Title

The Bidirectional and Hemispheric Reflectance of Apollo Lunar Soils: Laboratory and Diviner Measurements

Author

Smith, Emily Foote

Publication Date

2019

UNIVERSITY OF CALIFORNIA

Los Angeles

The Bidirectional and Hemispheric Reflectance of Apollo Lunar Soils:
Laboratory and Diviner Measurements

A dissertation submitted in partial satisfaction of the
requirements for the degree Doctor of Philosophy
in Geophysics and Space Physics

by

Emily Foote Smith

2019

ABSTRACT OF THE DISSERTATION

The Bidirectional and Hemispheric Reflectance of Apollo Lunar Soils: Laboratory and Diviner measurements

by

Emily Foote Smith
Doctor of Philosophy in Geophysics and Space Physics
University of California, Los Angeles 2019
Professor David A. Paige, Chair

We have created a comprehensive set of laboratory bidirectional measurements of lunar soil samples from Apollo missions 11, 12, 15, 16 and 17. The lunar soil samples successfully fit photometric models from the laboratory data to the solar spectrum averaged hemispheric reflectance as a function of the incidence angle. The Apollo 11 (vial 10084) and Apollo 16 (vials 61141 and 68810) soil samples are representative end member samples from the Moon's dark lunar maria and bright lunar highlands. We used our solar spectrum averaged albedos in a thermal model and compared our model-calculated normal bolometric infrared emission curves with those measured by the LRO Diviner Lunar Radiometer Experiment. We found excellent agreement at all of the Mare Apollo sites (Apollo 11, 12, 15 and 17) with Diviner at their landing sites. However, the sample from the Apollo 16 site, had an albedo measured in the laboratory that was 33% brighter than those required to fit the Diviner infrared data. We attribute this difference to increased compaction and decreased maturity of the laboratory sample relative to the natural lunar surface and to local variability in surface albedos at the Apollo 16 field area that are below the spatial resolution of Diviner. We address the idea of compaction as a possibility for the discrepancy of the Apollo 16 soil with additional measurements. We show that increasing the density and decreasing the porosity of the Apollo 11 and 16 samples increases the albedo of the samples. The albedo of the Apollo 16 highlands soil sample is nearly twice as sensitive to the effects of compaction as the mare Apollo 11 soil sample.

The dissertation of Emily Foote Smith is approved.

Michael K. Shepard

An Yin

David C. Jewitt

David A. Paige, Committee Chair

University of California, Los Angeles

2019

To my three amazing children: Alexandria, Eloise and Nathaniel -
follow your dreams with passion and conviction and you can accomplish
anything you set your mind to do.

I love you to the moon and back.

TABLE OF CONTENTS

Chapter 1

Chapter 2

Chapter 3

Chapter 4

References

LIST OF FIGURES

Chapter 1

Chapter 2

Chapter 3

Chapter 4

LIST OF TABLES

Chapter 1

Chapter 2

Chapter 3

Chapter 4

ACKNOWLEDGEMENTS

It's been a long road to finally writing this Acknowledgements page and it's fitting in doing so it completes my thesis. I recognize that my accomplishments in completing this work are the culmination of not only my efforts but the guidance and support from so many people in my life.

This thesis started in 2009 when I joined David Paige's group to study the Moon. I sincerely thank you for your help and guidance over the last decade. You’ve been a wonderful mentor and a dissertation advisor extraordinaire. I appreciate your giving me this opportunity, all the constructive criticism and endless patience. Failure was never an option!

I’d like to thank my incredible committee starting with Michael Shepard. You opened your lab to me, and you have always been so kind and supportive. I’d like to thank Dave Jewitt for providing great notes and making sure I understood the big picture behind the science. And to An Yin, the professor I’ve known the longest in the Department, your Structural Geology class and summer field trips had a huge impact on me. Your boundless energy and enthusiasm are contagious.

I am also indebted to Jeffrey Johnson for your guidance. Thank you for selecting me to serve on the LASER panels. I learned so much from them at an early point in my planetary career. And to Lauri Holbrook, you’ve always treated me with kindness and respect. You encouraged me to work hard and to never give up.

And a special thank you to Paul Davis. You are the reason I started the PhD program at UCLA. You believed in me and took me under your wing from the beginning.

I would like to thank CAPTEM, Carl Allen and Dick Morris for generously loaning the Apollo lunar soil samples to us for this study and for sharing their expertise. I’d also like to thank the Oxford team members: Neil Bowles, Tristram Warren and Rowan Curtis, for making the additional measurements we needed to complete this work. I’d like to thank the entire Diviner team and NASA Diviner LRO for funding this research.

To my UCLA friends: Farhad Bazargani (although we only spent one year in the PhD program together your on-going encouragement was so appreciated), Antonio Luis Dominguez Rameriz, Igor Stubailo, Martic Lukac (thank you for teaching me how to code and for making seismology fun. I will never forget the summer we spent installing seismometers in Peru) and Deborah Weiser for making workouts fun at UCLA.

To my mom Marjorie Diehl - my editor-in-chief and one of my biggest supporters. Thank you for never doubting my abilities or determination and for encouraging me to follow my heart. To my dad Robert Foote - you inspired my love of nature with our hiking and camping trips. I am a scientist in large part because you taught me the value of always questioning and exploring. To my sister Virginia Halverson - you are the best sister anyone could hope for and a true best friend. Thank you for always having my back and for keeping me honest and grounded in this life. I'm so grateful we have each other. To my brother Jon Foote - thank you for always challenging me and supporting me and for making our childhood trips to Virginia Lakes and Mammoth mountain so much fun.

To Grandma Jeanne Diehl (who inspires me to be adventurous) and all of my extended family - you are all the foundation of my life and I love you.

To Beth Smith the best mother-in-law, thank you for all of your love, support and encouragement. To Karen Foote thank you for joining our family and putting up with all of us! To Aunt Melinda and Uncle Sid thank you for your love, support and for knowing how to have a good time and laugh. To my sister-in-law, Rachel Smith, you were one of my earliest co-conspirators at UCLA. You have been a model for scientific success. And for introducing me to -

My husband Ethan Smith. Meeting you was the reason I stayed in LA and continued my work at UCLA. Thank you for your love, unequivocal support and our beautiful family. Words cannot express how truly grateful and happy I am to be with you. I'm so blessed we're on this life adventure together.

To anyone not named here - know that I love and appreciate all of you.

CURRICULUM VITAE

EDUCATION

Ph.D. Candidate, University of California, Los Angeles, Earth, Planetary and Space Sciences, Geophysics and Space Physics (advisor, David A. Paige)

M.Sc., 2012, University of California, Los Angeles, Earth, Planetary and Space Sciences, Geophysics and Space Physics (advisor, David A. Paige)

B.S., 2007, University of California, Los Angeles, Earth, Planetary and Space Sciences, Geology (with honors)

PEER REVIEWED PUBLICATIONS

Foote, E. J., Paige, D. A., Shepard, M. K., Johnson, J. R. and Biggar, S. (2019) The Bidirectional and Directional Hemispheric Reflectance of Apollo 11 and 16 Soils: Laboratory and Diviner Measurements, *Icarus*.

Paige, D.A., M. A. Siegler, J. A. Zhang, P. O. Hayne, **E. J. Foote,** K. A. Bennett, A. R. Vasavada, B. T. Greenhagen, Schofield, J. T., D. J. McCleese, M. C. Foote, E. M. De Jong, B. G. Bills, W. Hartford, B. C. Murray, C. C. Allen, K. J. Snook, L. A. Soderblom, S. Calcutt, F. W. Taylor, N. E. Bowles, J. L. Bandfield, R. C. Elphic, R. R. Ghent, T. D. Glotch, M. B. Wyatt, P. G. Lucey (2010b) “Diviner Lunar Radiometer Observations of Cold Traps in the Moon’s South Polar Region”, *Science,* 330, 479-482

Johnson, J. R, Shepard, M. K., Grundy, W. M., Paige, D. A, **Foote, E.** (2013), "Spectrogoniometry and modeling of martian and lunar analog samples”, *Icarus,* 223, 383-406.

AWARDS, HONORS AND SCHOLARSHIPS

2015	NASA Group Achievement Award, LRO Diviner Extended Mission, The LRO Extended Science Mission Team
2013	NASA Group Achievement Award, LRO Diviner Extended Mission, Diviner Lunar Radiometer Science Mission Team
2012	NLSI Student Poster Award
2011	NASA Group Achievement Award, LRO Diviner Extended Mission, The Lunar Reconnaissance Orbiter (LRO) Exploration
2011	NASA Group Achievement Award, LRO Mission Operations Team, for

	Exceptional accomplishments in operating the LRO spacecraft & instruments
2007	UCLA EPSS salutatorian award
2007	National Association of Geosciences Teachers Field-Course Scholarship
2006-2007	UCLA Undergraduate Research and Teaching Scholar program (URSTP) award for endowed by Wasserman
2004-2006	UCLA Scholarship, TAP Ingram Scholar
2004	Los Angeles Geographical Society Scholarship
2004	LAVC Patrons Transfer Alliance Program Honors Scholarship
2004	Lorraine Dettwyler Most Improved Earth Science Female Scholarship
2004	LAVC Patrons TAP Tom Yakavone Scholarship
2004	LA Patrons Moxie Scholarship

TEACHING EXPERIENCE

2010 (Winter)	EPSS 8 (Introduction to Seismology) Graduate Teaching Assistant, Earth Planetary and Space Science Department, University of California, Los Angeles
2006 (Fall)	EPSS 1 (Introduction to Geology) Undergraduate Teaching Assistant, Earth Planetary and Space Science Department, University of California, Los Angeles Provided supplementary material through group lectures and one on one tutoring sessions
2005 (Fall)	EPSS 3 (Astrobiology) grader, Earth Planetary and Space Science Department, University of California, Los Angeles Westwood, CA, Fall Graded short essays and assisted in writing the exams
2005 – 2006	Head Undergraduate Tutor for Earth Science and Anthropology Department Los Angeles Valley College, Earth Science and Anthropology Department. Run tutoring lab, scheduling, payroll, spreadsheet of attendance, proctor exams.
2004 – 2006	Undergraduate Tutor for geology, oceanography, geography (Physical and Cultural), meteorology, GIS, astronomy, anthropology, Los Angeles Valley College, Earth Science and Anthropology Department

CHAPTER 1

Introduction

1.0 Objectives

The primary goal of this thesis is to analyze and understand the solar reflectance of the Moon. Our approach is to determine the solar spectrum averaged albedos for six Apollo soil samples and use them to calculate the bolometric infrared emission curves, which are needed to compare to the Lunar Reconnaissance Orbiter (LRO) Diviner orbital bolometric temperatures taken at the six Apollo soil sample sites. The Diviner and Laboratory datasets provide complementary and independent insights into the photometric properties of the lunar surface. We have created the most extensive set of laboratory bidirectional measurements of lunar soil to date and have successfully fit photometric models to the data. We have successfully determined the bolometric reflectance for both Highlands and Mare soils, and used the results in lunar thermal models. Our studies verify the use of laboratory albedo measurements which can be used as key inputs to lunar thermal models, as well as to better define physical properties and compositions of planetary surfaces.

A secondary objective was to obtain a full Bidirectional Reflectance Distribution Function (BRDF) and find a photometric model that fits the Apollo 11 and 16 BUG datasets. The model enables the calculation BRDF's at any combination of photometric angles, and the determination of the hemispheric bolometric reflectance (see figure 1.1) We chose Hapke's 1993 BRDF model and a simplified empirical BRDF model, that we developed specifically for this study, to fit the Apollo BUG BRDF data, and use the results in a lunar thermal model and compare the results with infrared measurements by the LRO Diviner instrument.

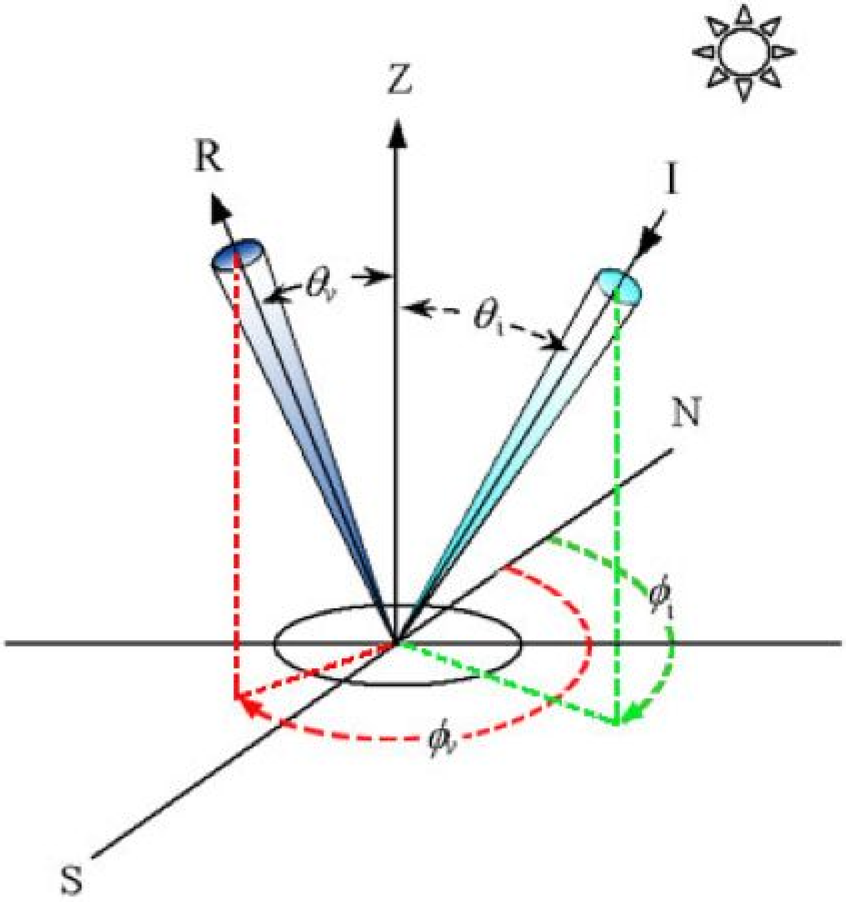

Figure 1.1: Illustration of the photometric angles used in this study: *i* is the solar incidence angle, *r* is the reflectance off the surface.

1.1 Background

The formation and evolution of the lunar regolith is a complex process. The nature and history of the regolith is determined by two completely random mechanisms at various locations. One mechanism is destructive—the excavation of existing regolith by impact craters. The other mechanism is constructive—the build up of layers of new material (either from bedrock or older regolith) that is excavated from either near (small) or distant (large) impact craters. Additionally, high-energy particles produce distinctive nuclear reactions to depths of several meters. At the surface, dust particles form microcraters and solar-wind atomic particles are trapped in the outer layers of regolith grains. (Lunar Sourcebook, 1991) The effects of solar and cosmic particles that strike the lunar surface are subsequently superimposed on these mechanical processes.

The chemical composition of the lunar soil varies considerably, however, the physical properties such as grain size (average 40 to 110 microns), density, compaction and compressibility are fairly similar for both the highlands and mare regions. For example, the seismic velocities of the uppermost layer of the moon, the lunar regolith which has a thickness of approximately 4 meters, has uniform seismic velocities for both highlands and mare averaging 100 m/s (Heffels et al, 2017).

A physical parameter that relates to the density of the uppermost few centimeters of the lunar surface is the H parameter. The H-Parameter is the characteristic depth scale in centimeters over which the density of the lunar regolith transitions from a density of 1100 kg m^{-3} at the surface to 1800 kg m^{-3} at depth (Hayne et al., 2017). The H-Parameter provides a means of gradually varying the thermal conductivity of the uppermost regolith layers, which is needed to determine/calculate the bolometric brightness temperatures of the lunar surface.

1.2 Lunar Soil

We focus on the lunar soil, which is defined as the finer-grained upper few centimeters of the lunar regolith. Neil Armstrong clearly described the lunar soil when he stepped down onto the moon: “I’m at the foot of the ladder… the surface appears to be very, very fine-grained, as you get close to it, it's almost like a powder… It does adhere in fine layers like powdered charcoal to the sole and sides of my boots. I only go in a small fraction of an inch. Maybe an eighth of an inch, but I can see the footprints of my boots and the treads in the fine sandy particles" (NASA archives). Figure1. 2 shows the footprint of Armstrong's boot into the surface.

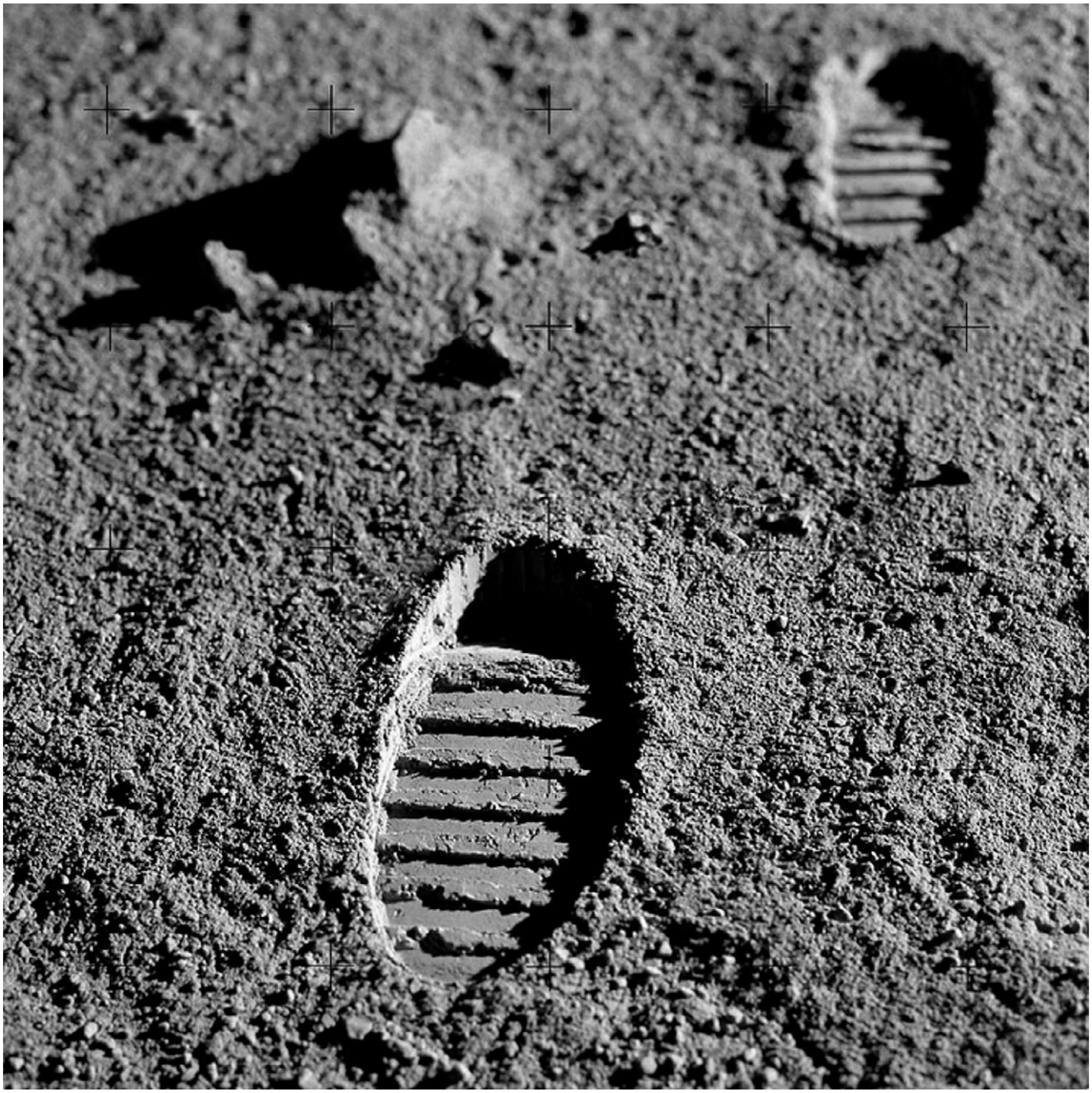

Figure 1.2: Close-up view of Apollo 11 astronaut Neil Armstrong's footprints in the lunar soil. Notice the fine grained and fluffy texture and the compressibility of the upper few centimeters of the regolith. (Courtesy of NASA)

The lunar soils range in composition from basaltic to anorthositic and show considerable variation. The five basic types of soil particles are crystalline rock fragments, mineral fragments, breccias, agglutinates and glasses. The soils are somewhat cohesive, dark grey to light grey, very-fine-grained, loose, clastic material derived primarily from the mechanical disintegration of basaltic and anorthositic rocks. This variation in soils is demonstrated by comparing the Apollo 11 rocks, which were a mixture of basalts and breccias, with the Apollo 12 rocks, which were almost all basalts, with only two breccias in the returned samples. This difference is directly related to the age and mineralogy of the samples. The Apollo 11 samples were formed some 500 million years after the samples obtained from Apollo 12 were formed. In addition, these samples support the belief that the mare volcanism did not occur as a single, Moon-wide melting event. The subsequent Apollo 15, 16 and Apollo 17 missions provided the opportunity to obtain samples from deeper in the lunar crust than was previously possible and in part due to inaccessible locations. This variety allowed us to examine samples of highland (Apollo 16) material that were older than the Imbrium impact and investigate the possibility of young, explosive volcanism in this region (Lunar Sourcebook, 1991).

The Apollo missions/astronauts were successful in retrieving numerous samples which allows the continuation of detailed examination of the materials from various locations. As an example, the Apollo 11 astronauts collected approximately 20 kilograms of lunar regolith during their two and a half hour exploration of the surface. Many more extensive samples of the lunar surface and subsurface material were excavated and brought to Earth for analysis in subsequent Apollo missions.

The capability to collect samples many kilometers from the lander was made possible with the Apollo Lunar Roving Vehicle (LRV). Figure 1.3 shows a close up picture of the lunar rover that the astronauts used to gather samples that were far from the lunar module. Figures 1.4 and 1.5 show astronaut and scientist Harrison Schmidt actively collecting lunar soil from the surface of the moon and roaming around the Apollo site.

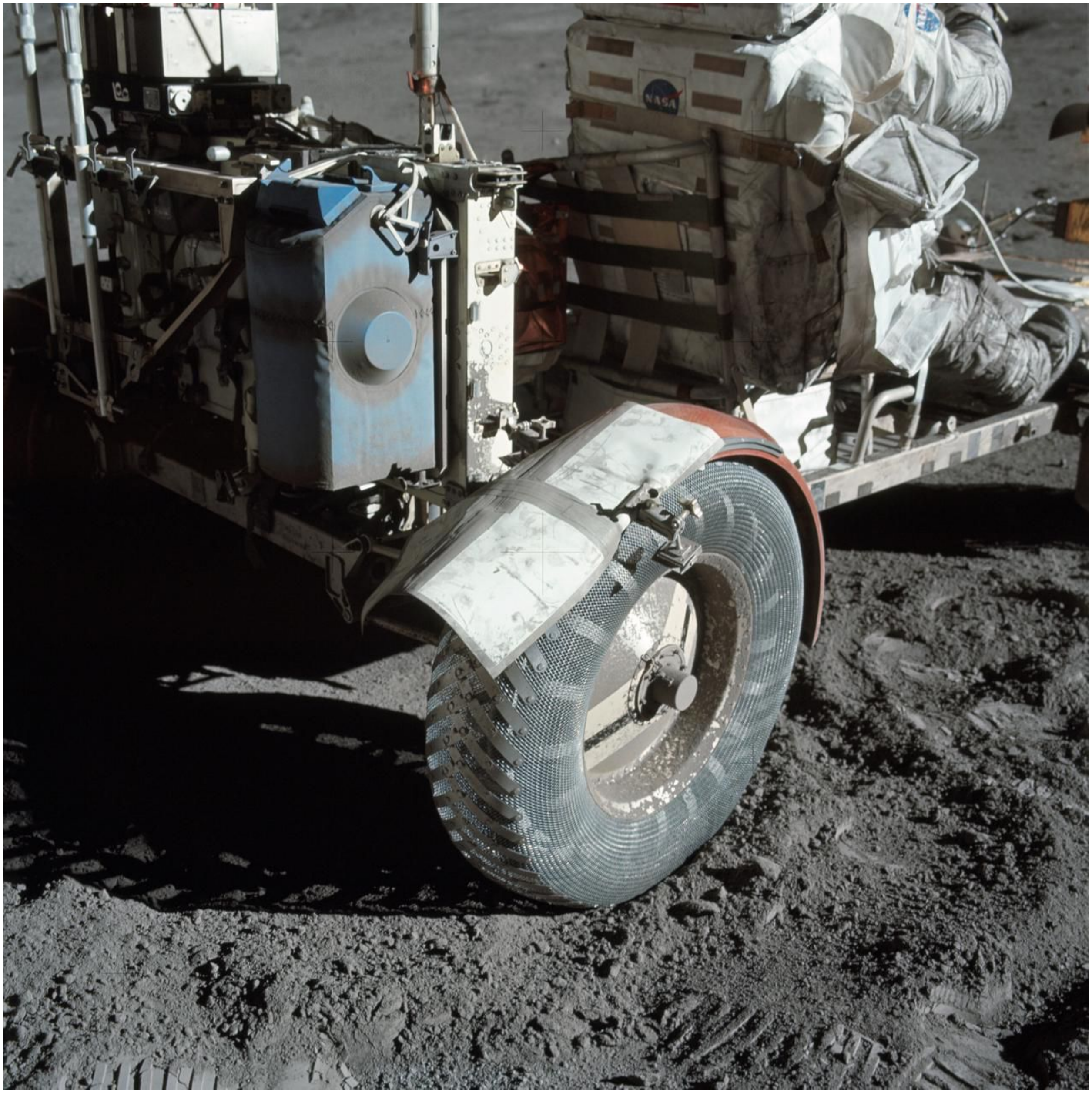

Figure 1.3 : NASA archive photograph of the lunar roving vehicle (LRV) at the Taurus-Littrow landing site from the Apollo 17 mission.

Figure 1.4: NASA archive image of Apollo 17 scientist-astronaut Harrison Schmitt, scooping up lunar soil material from the surface.

Figure 1.5: NASA archive picture of Apollo 17 scientist-astronaut Harrison Schmitt at the Taurus-Littrow landing site (Station 5). He appears to be heading towards a selected area to study and collect more lunar soil samples.

1.3 Apollo Samples

The Moon is the only planetary objects from which we have a large quantities of soil and rock samples, which are extremely valuable for photometric studies. Birkebak, Cremers and Dawson (Birkebak et al., 1970) used Apollo 11 soil samples to determine unidirectional reflectance measurements. In the post-Apollo era, McCord, et al, compared near-infrared reflectance measurements taken from Apollo samples to telescopic observations and showed that they are in good general agreement (McCord et al., 1981). Hapke et al (1998) made photopolarimetric measurements using JPL's goniometer on eight Apollo soil samples to investigate the opposition effect. In 1997, the research by Blewett, Lucey, Hawke, Ling and Robinson (1997) demonstrated a significant (factor of two) difference between laboratory measurements of lunar samples, and those derived from measurements by the Clementine Orbiter. They theorized that the packing or roughness of the samples may have been responsible for this discrepancy. However, the calibration of the two devices could well be significantly different, leading to different comparative results. Later research by Ohtake et al., appears to bear this out as they discovered significant disagreement between orbital Moon reflectance measurements across different missions and instruments. (Ohtake et al., 2010 and 2013).

The Curation and Analysis Team for Extraterrestrial Materials (CAPTEM) provided us with six representative lunar soil samples from five Apollo missions where the mean grain size ranged from 40μm to about 100μm. These are: 1) a typical low albedo mare sample (10084, Apollo 11); 2) a low titanium basaltic mare sample with impact breccias (12001, Apollo 12); 3) an Apollo 15 mare sample (15071); 4) a high albedo lunar highlands soil (68810 & 61141, Apollo 16) and 5) an Apollo 17 mare soil sample (70181). Figure 1.6 shows close up images of the lunar samples in this study with a picture of the moon where the Apollo landing sites/ samples were collected. Table 1.1 contains the coordinates of the Apollo landing/sample sites.

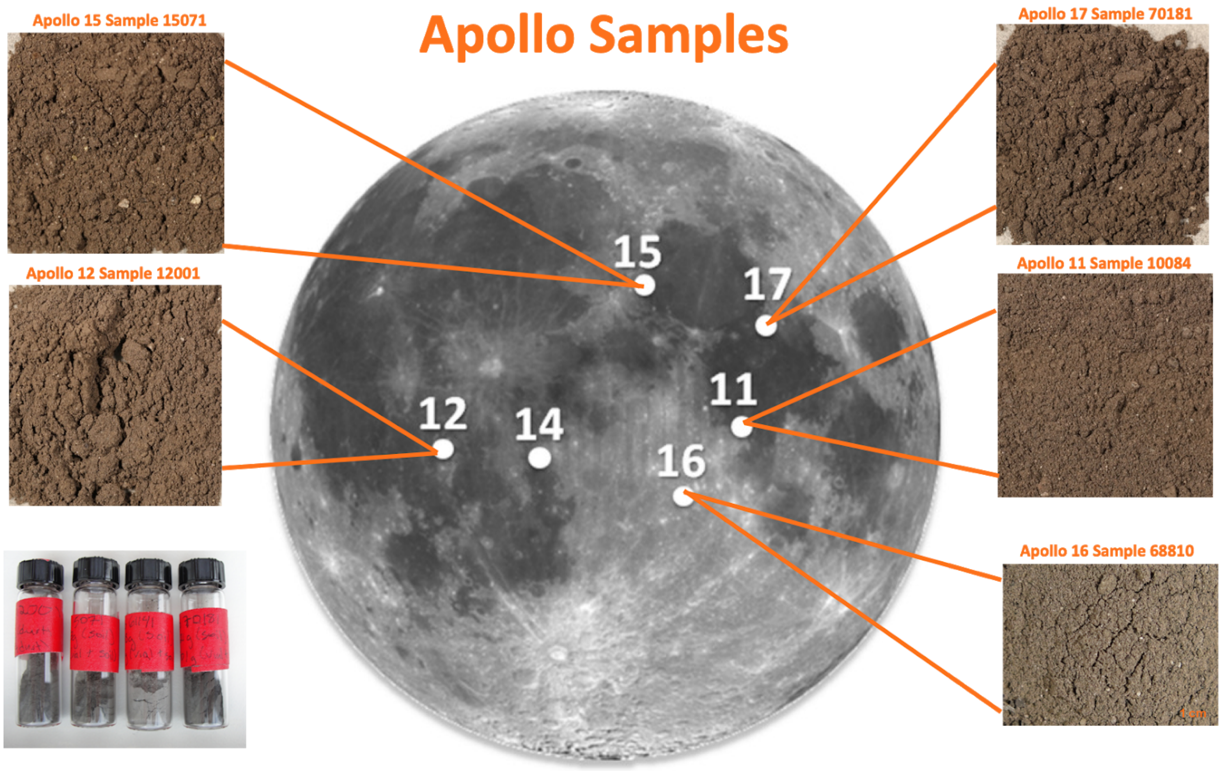

Figure 1.6: Map of the near side of the moon with close up images of our Apollo samples. Note: the picture of the vials on the bottom left are shown to depict the contrast between the various pristine lunar soil samples used in this study (ap 12001, 15071, 61141and 70181) under the same illumination. The width of each image is 1cm.

Table 1.1: The Lunar coordinates of our Apollo soil samples.

Apollo Sample	**Longitude**	**Latitude**
Apollo 10084	23.47242165	0.673705459
Apollo 12001	-23.421697617	-3.012505293
Apollo 15071	3.597932339	26.03899956
Apollo 68810	15.48301029	-8.974000931
Apollo 70181	30.79599953	20.15399933

1.4 Photometry

Historically, lunar photometry has been used as a tool to determine various lunar soil properties via telescopic and spacecraft data or laboratory bidirectional measurements derived from samples. Bidirectional reflectance is a function of the incidence (illumination source) and emission (detector position) angles and their position relative to each other which is referred to as the phase angle (Shepard, 2017). Figure 1.7 shows an example of photometric angles. One of the earliest and most cited pre-Apollo papers concerning bidirectional reflectance measurements is Minnaert's 1941 paper in which he tests and applies Helmholtz's principle of reciprocity to telescopic photometric measurements of the Moon (Minnaert, 1941). Later, Thomas Gold first hypothesized that the surface of the Moon's surface consisted of fine dust like particles based on its photometric properties (Gold, 1955). Subsequently, Bruce Hapke developed a goniometer to make bidirectional reflectance measurements of several hundred different materials. He was the first to compare laboratory reflectance measurements to the telescopic reflectance of the lunar surface. (Hapke and Van Horn, 1963). The lunar soil is so fine grained that the cohesive strength of the particles are stronger than the force of gravity. The dust clumps in a way that creates peculiar structures which have been referred to as "fairy castles". Early in his career, Hapke determined that the highly back scattering effect from the lunar surface, the brightness at zero phase angles was due to these "fairy castle" structures embedded in the lunar surface. Prior to the Apollo missions, he developed a semi-empirical photometric model to fit the bidirectional reflectance of fine grained particles such as those on the Moon. His model has evolved over time due to the availability of new lunar orbital and laboratory photometry datasets. (Hapke, 1981; 1993; 1998; 2008).

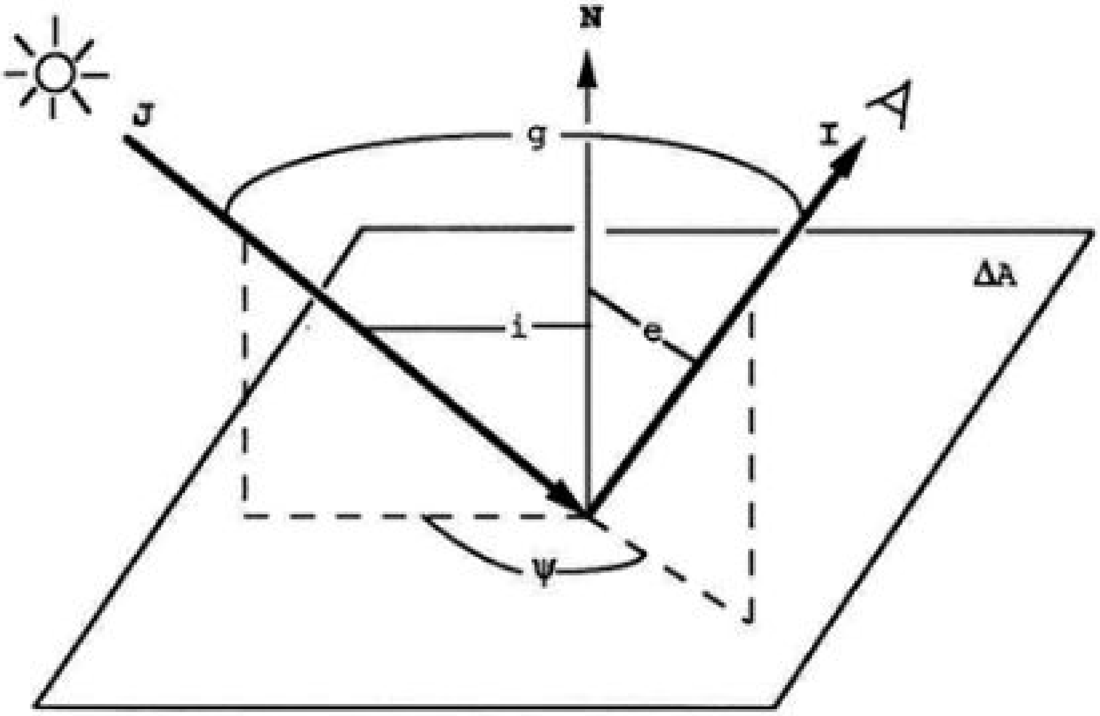

Figure 1.7: Illustration from Hapke (1993) showing the photometric angles used in this study: *i* is the solar incidence angle, *e* is the emission angle, *g* is the phase angle and ψ is the solar azimuth angle.

1.5 Scope of Thesis

In the subsequent chapters we take a deeper look at the solar spectrum averaged hemispheric albedos and the bolometric temperatures of the Moon. Chapter two has been reformatted from the revised and resubmitted paper to *Icarus* entitled "The Bidirectional and Directional Hemispheric Reflectance of Apollo 11 and 16 Soils: Laboratory and Diviner Measurements" with coauthors David Paige at UCLA, Michael Shepard at Bloomsburg University, Jeffrey Johnson at APL and Stuart Biggar at University of Arizona. It focuses on determining the bolometric hemispheric reflectance of a representative lunar mare sample from the Apollo 11 mission and a representative highlands sample from the Apollo 16 mission. We compare the bolometric albedo to Diviner's Solar and Thermal infrared datasets. In Chapter Three we focus on the maria regions of the Lunar surface. We analyze Apollo soil samples from the Apollo 12, 15 and 17 missions. Chapter Four examines how changing the compaction i.e the porosity of a soil impacts the albedo of the surface. We study the effect of packing density on the two types of lunar soil - a typical low albedo soil sample from the lunar mare (Apollo 11) and a medium-low albedo soil sample from the Highlands (Apollo 16).

CHAPTER 2

The Bidirectional and Directional Hemispheric Reflectance of Apollo 11 and 16 Soils: Laboratory and Diviner Measurements

This chapter has been reformatted from the following revised paper:

Foote, E. J., Paige, D. A., Shepard, M. K., Johnson, J. R. and Biggar, S. (2019) *The Bidirectional and Directional Hemispheric Reflectance of Apollo 11 and 16 Soils: Laboratory and Diviner Measurements*. ICARUS

2.0 Introduction

The bolometric hemispheric reflectance is the total reflected energy from a surface for a given solar incidence angle (Hapke, 1993). Determining the bolometric hemispheric reflectance of the Lunar surface is important because of the key role it plays in the surface energy balance. It determines the radiative equilibrium temperature of the surface (Hapke, 1993), and it is thus a key input for lunar thermal models. The bolometric hemispheric reflectance cannot be fully measured from orbit, but it can be measured in the laboratory by integrating spectrophotometers or by goniometers. The first measurements of the hemispheric reflectance of lunar samples were made by Birkeback and Cremers (1970) who used an integrating spectrophotometer to measure the directional spectral and total reflectance of newly acquired soil samples from Apollo 11. Their results have been incorporated into subsequent thermal models of the lunar surface (Keihm 1984; Vasavada et al., 1999, 2012, Hayne et al., 2017). This study presents the results of a new set of laboratory bi-directional reflectance measurements of two Apollo regolith samples which are interpreted in terms of the bolometric hemispheric reflectance.

One of the main motivations for this work is to obtain full Bidirectional Reflectance Distribution Functions (BRDF's) for representative lunar maria and highlands samples. The BRDF allows calculation of reflectance at any combination of photometric angles as well as the integrated hemispheric reflectance. In this study, we measured the full bidirectional reflectance distribution functions of two lunar soil samples from the Apollo 11 and 16 missions. We then fit two BRDF models, one theoretical and one empirical, to the laboratory data and computed the bolometric hemispheric reflectance. We next used our derived bolometric hemispheric reflectances in conjunction with a one-dimensional thermal model to calculate the bolometric infrared emission at the Apollo 11 and Apollo 16 landing sites, and compared these results with diurnal bolometric thermal emission measurements made by the Lunar Reconnaissance Orbiter Diviner Lunar Radiometer Experiment, DIVINER (Paige et al., 2010a).

2.1 Materials and Methods

2.1.1 Samples The Curation and Analysis Team for Extraterrestrial Materials (CAPTEM) at NASA provided two representative lunar soil samples: a typical low albedo mare sample (10084, Apollo 11), and a high albedo lunar highlands soil (68810 & 61141, Apollo 16) (Figure 1). Descriptions of each of our samples can be found in Table 1, which includes petrography, grain size, maturity and major elements. For our purposes, maturity is defined as the degree of surface exposure to micrometeorites and solar wind which particular soil has experienced. The specific information was derived from the Lunar Soil Handbook (Handbook of Lunar Soils, 1993) Table

1 also shows our measurements of the bulk density of our two lunar soil samples, which was accomplished by measuring the weights of the samples in a 2.5 ml volume.

For this study, CAPTEM generously loaned us 28.578 grams of the Apollo 11 lunar soil sample 10084, 52.000 grams of the Apollo 16 lunar soil sample 68810 and 20 grams of the Apollo 16 lunar soil sample 61141. The Apollo 11 sample is a basaltic regolith that has a substantial non-mare component. The composition is 66% crystalline mare basalt, 20% feldspathic particles from the highlands, 8% KREEP-bearing, impact-melt breccias, 5% orange volcanic glass and 1% meteoritic material (Korotev and Gillis, 2001). Unfortunately, the Apollo 16 samples have not yet been characterized in detail. However, other Apollo 16 soil samples (e.g. 68820) that have been characterized are primarily composed of impact breccias and anorthositic rocks (Handbook of Lunar Soils, 1993). Figure 1 is a close up image of our two lunar soil samples.

The samples used in our study are not pristine. We cannot say for certain they weren't contaminated from terrestrial exposure. Previous research looked at the effects of hydration and found the absorption feature of water near 3 microns in pristine lunar soil samples (Izawa, 2014). Millikan and Mustard (2005) also made spectral reflectance measurements on fine particle samples and studied how the absorption of water changes the reflectance. Spectral variations near 3 microns will not have an impact on our analyses because the magnitude of the solar flux is very small in this spectral region. Also, Birkebak and Cremers (1970) measured the directional reflectance of Apollo Lunar soil, sample 10084, in a vacuum and at standard atmospheric pressure which yielded no spectral absorption features from 0.5 microns to 2.0 microns.

Table 2.1: Descriptions of Apollo samples used in this study from The Handbook of Lunar Soils (Handbook of Lunar Soils, 1983) We measured the bulk density of Highland sample (68810) and Mare sample (10084) in our lab (see text). Note: average grain size

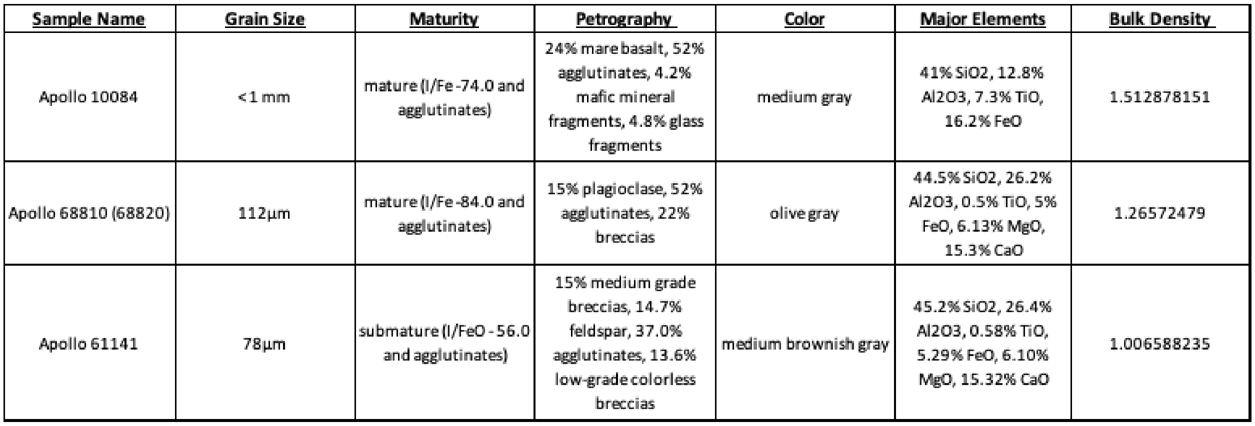

Sample Name	Grain Size	Maturity	Petrography	Color	Major Elements	Bulk Density
Apollo 10084	<1 mm	mature (I/Fe -74.0 and agglutinates)	24% mare basalt, 52% agglutinates, 4.2% mafic mineral fragments, 4.8% glass fragments	medium gray	41% SiO2, 12.8% Al2O3, 7.3% TiO, 16.2% FeO	1.512878151
Apollo 68810 (68820)	112µm	mature (I/Fe -84.0 and agglutinates)	15% plagioclase, 52% agglutinates, 22% breccias	olive gray	44.5% SiO2, 26.2% Al2O3, 0.5% TiO, 5% FeO, 6.13% MgO, 15.3% CaO	1.26572479
Apollo 61141	78µm	submature (I/FeO - 56.0 and agglutinates)	15% medium grade breccias, 14.7% feldspar, 37.0% agglutinates, 13.6% low-grade colorless breccias	medium brownish gray	45.2% SiO2, 26.4% Al2O3, 0.58% TiO, 5.29% FeO, 6.10% MgO, 15.32% CaO	1.006588235

Notes: Descriptions for Apollo 68810 were substituted with the adjacent Apollo 68820 sample information, because Apollo 68810 has not been characterized. It was given to us as a test sample. Dick Morris (JSC) made the maturity measurement of our Apollo 68810 sample.

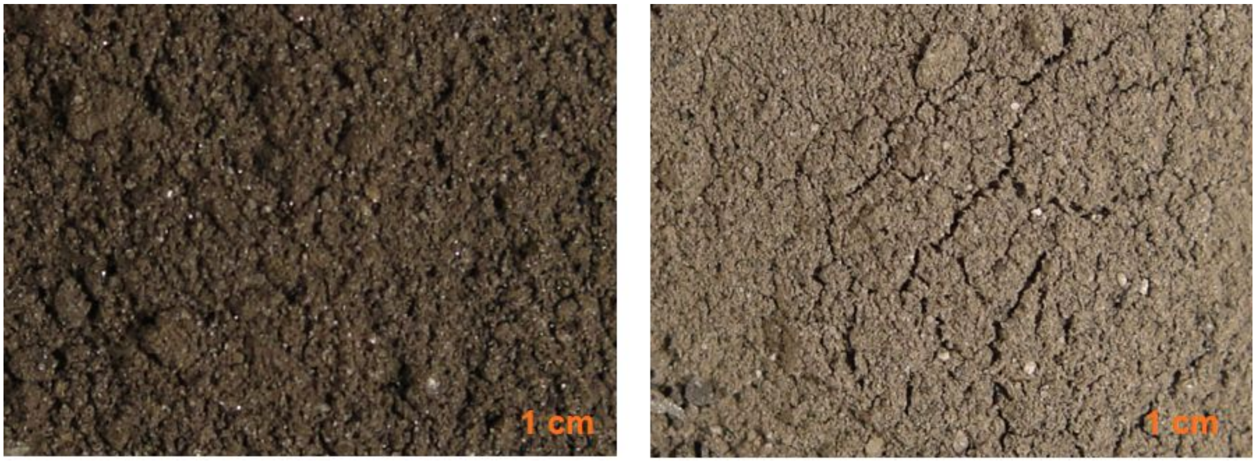

Figure 2.1: Close up images of the Apollo 11 and 16 lunar soil samples. The width of each closeup sample image is 1 cm.

2.1.2 BUG Apparatus We used the Bloomsburg University Goniometer (BUG) (Shepard et al., 2002) to make the Bidirectional Reflectance Distribution Function (BRDF) measurements on the Apollo samples. The BUG instrument consists of a filtered, chopped and collimated light source and a solid-state detector. The source and detector move along three independent axes. The source is a 100 W quartz halogen bulb and is attached to an arm that moves 0-65º degrees in incidence (i) and 0-180º degrees in azimuth, 60 cm away from the sample. The detector is attached to an arm that moves 0-80º in emission (e) angle, 80 cm away from the sample. Figure 2.2 shows the BUG experimental setup which was optimized for obtaining reflectance measurements at high incidence and emission angles. We prepared the sample by carefully pouring it into a small dish and leveling the surface with a straight edge. Figure 2.2 also shows the prepared sample on the goniometer in between measurements.

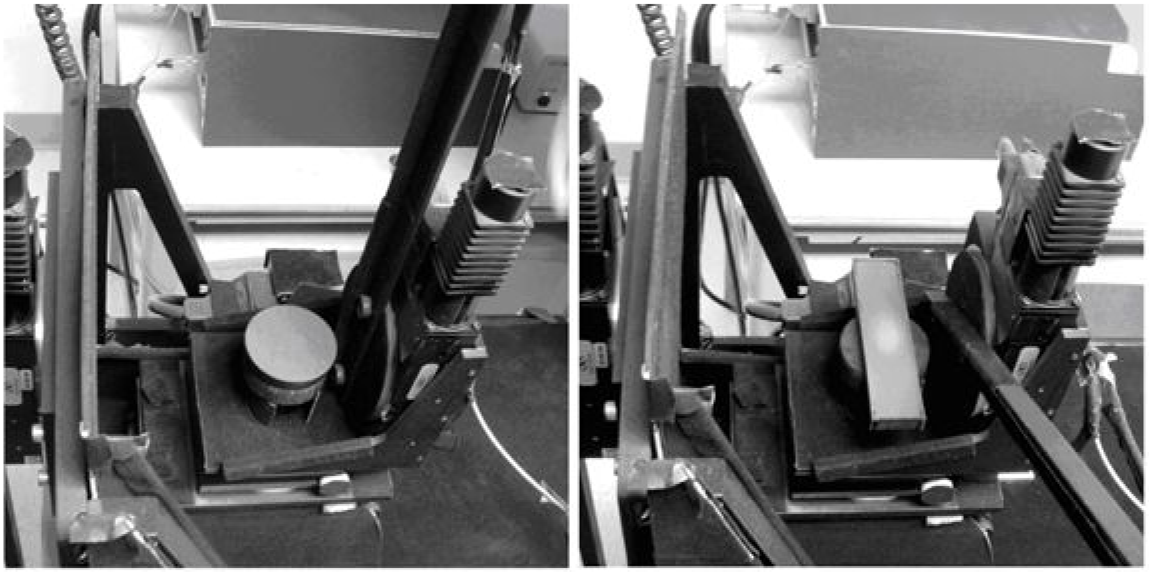

Figure 2.2: The BUG experimental setup for measuring Bidirectional Reflectance Distribution Functions (BRDF). (left) The standard BUG setup uses a sample cup with a diameter of 6 cm and a depth of 0.5 cm. (right) The nonstandard BUG setup for measurements along and perpendicular to the principal plane axis using a 12 cm x 2.5 cm x 0.5 cm dish, which enabled acquisition of data at high incidence angles (*i* >60°).

2.1.3 Data Acquisition, Calibration and Verification The BUG instrument is calibrated before and after each run. This calibration procedure included measuring the raw intensity in voltage of a Spectralon reference target, certified to NIST standards, at an incidence angle, i=0º and emission angle, e=5º (Shepard and Helfenstein, 2007, 2011).

We collected two different types of BUG reflectance datasets. The standard set of BUG BRDF measurements includes a set of incidence angles ($0º < i < 60º$), emission angles ($0º < e < 80º$), and phase angles ($3º < g < 140º$), which provided us with 680 measurements per wavelength (Shepard and Helfenstein 2007, 2011, and Johnson et al., 2013) (see Figure 2.3). We also obtained separate BUG datasets at high-incident angles. These measurements were acquired along and perpendicular to the principal plane axis and include incidence angles $0º < i < 75º$ and phase angles $3º < g < 155º$, which gave us an additional 89 points per wavelength (for a grand total of 769 angle combinations). We used 4 narrow-band spectral filters to obtain the following data sets: 450, 550, 750, and 950 nm (Johnson et al, 2009).

The BUG measures the radiance factor r_f, which is the ratio between the measured intensity to that of a normally illuminated perfectly reflecting diffuse (Lambert) surface. Since r_f varies with illumination geometry, the bidirectional reflectance is most easily visualized in terms of the Lambert albedo, which is the ratio to the measured reflectance relative to that of a Lambert surface measured under the same illumination condition (Hapke, 1993; Shepard, 2017). For this work, we define Lambert albedo as:

$$A_L = r_f/\mu_0 \qquad (1)$$

Where μ_0 is the cosine of the incidence angle.

Apollo 11, i=15° and i=60°

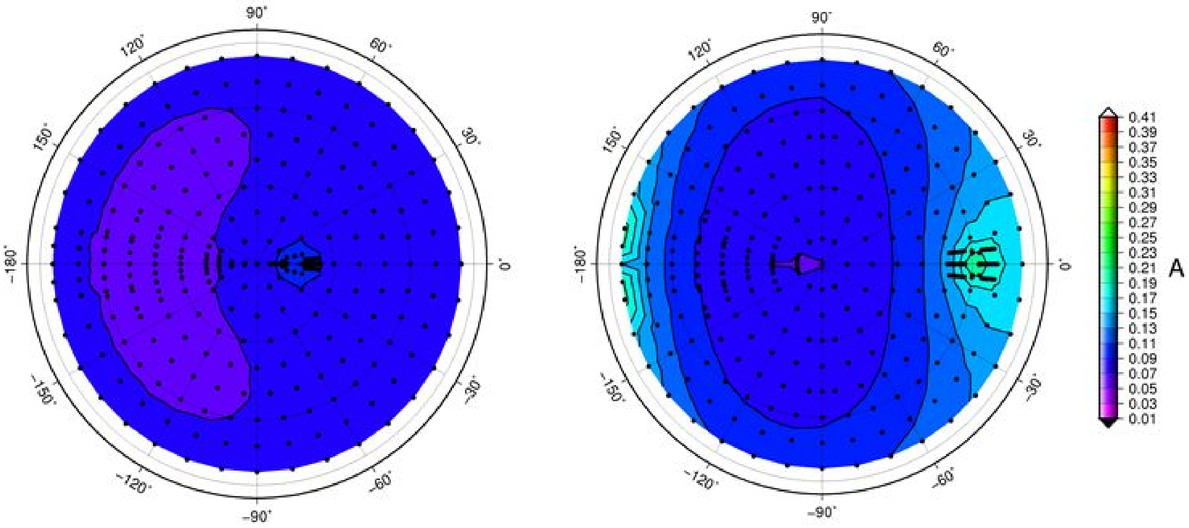

Apollo 16, i=15° and i=60°

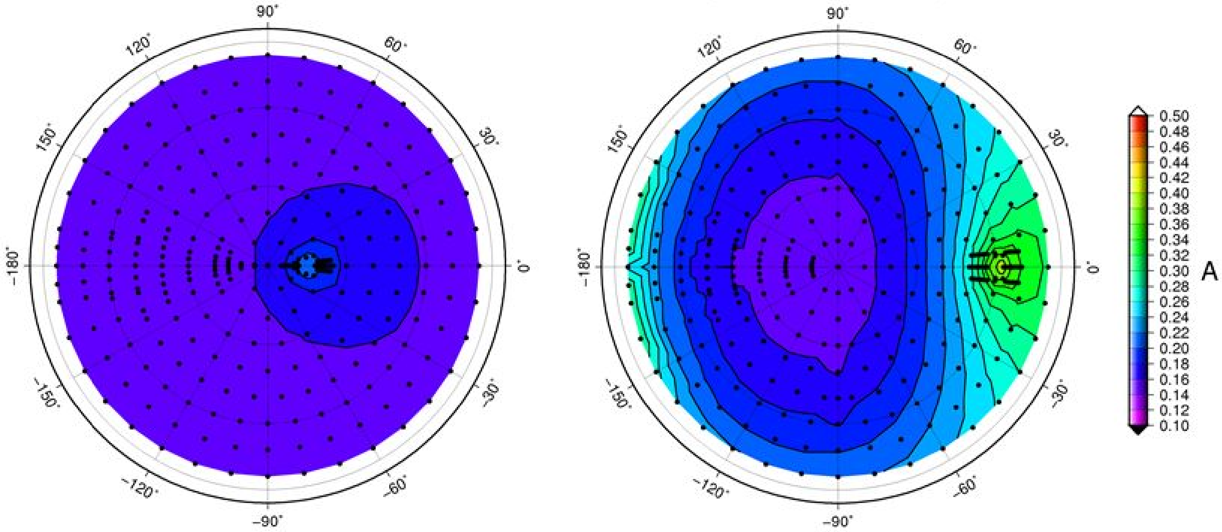

Figure 2.3: Polar contour plots of measured Lambert Albedo (A) where e is radial coordinate and ψ is the azimuthal coordinate (see figure 8.1 in Hapke, 1993 for graphical depiction of the angle). Dots denote BUG angle sets. Shown are measurements for i= 15° and i= 60° for both Apollo 11 (top 2) and Apollo 16 (bottom 2). The illumination source is along the positive X axis. The radial coordinate is emission angle (to 90°) and the azimuthal coordinate is azimuth angle, where 0° azimuth defines the plane of incidence. The principal plane is oriented along the x axis.

We verified our BUG BRDF measurements in three ways. First, we checked reciprocity for measurements of a white Spectralon target for several sets of angles (Figure 2.4). We examined the ratio of Lambert albedos of 47 reciprocal pairs as a function of azimuth angle, phase angle, emission angle and incidence angle. As illustrated in the plot, the BUG measurements obey the Helmholtz reciprocity principle also known as Principle of Reciprocity (Minnaert, 1941 and Shepard, 2017) to a high degree, as the average Lambert albedo ratio is 1.0092345. Also noticeable, is how the majority (approximately 67%) of the values fall along the 1.00 line.

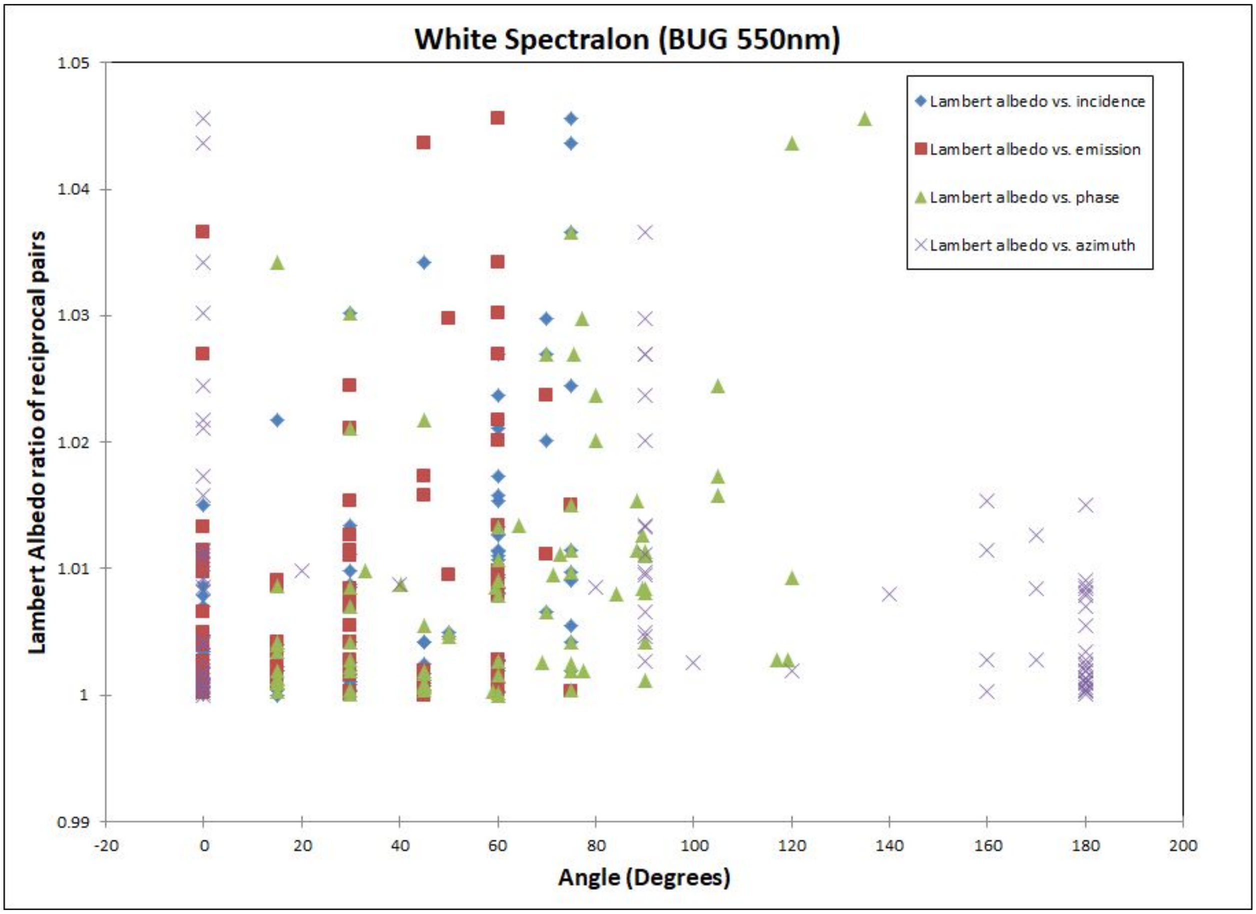

Figure 2.4: Reciprocity check of the spectralon measurements made on BUG. The majority of the points fall along 1.00. The average value of the 47 reciprocal pairs is 1.0092345.

For our second verification, we did a cross calibration check between the BUG goniometer at 550 nm and the Blacklab goniometer at the University of Arizona Optical Sciences Lab at 554 nm (Biggar et al., 1988; 2003). The Blacklab goniometer was used previously to measure the bidirectional reflectance of the Diviner flight solar calibration target (Paige et al., 2010a). The Blacklab measurements of the two spectralon targets were calibrated relative to a prepared Algoflon targets whose bidirectional reflectance for normal illumination, and whose integrated hemispheric reflectance was directly traceable to NIST standards. Comparing Blacklab to BUG revealed that the calibration procedures previously employed by BUG resulted in absolute reflectances that were systematically lower than Blacklab by a factor of 0.955. Figure 2.5 shows corrected BUG vs Blacklab Spectralon reflectances from Shepard and Helfenstein (2011). To make our BUG lunar sample measurements consistent with Blacklab, we applied a correction factor of 1.047 to all our BUG data.

For our third verification, we measured the same Apollo 11 lunar soil sample with Blacklab at 455, 554, 699 and 949 nm and with BUG at 450, 550, and 950 nm for a restricted set of 25 photometric angles ($60^\circ < i < 75^\circ$), ($60^\circ < e < 80^\circ$), and ($51^\circ < g < 94^\circ$) and found that the ratios of Blacklab to corrected BUG reflectances were 1.0028 at 455/450 nm, 1.0066 at 554/550 nm, 0.963 at 699/750 nm, and 1.046 at 949/950 nm.

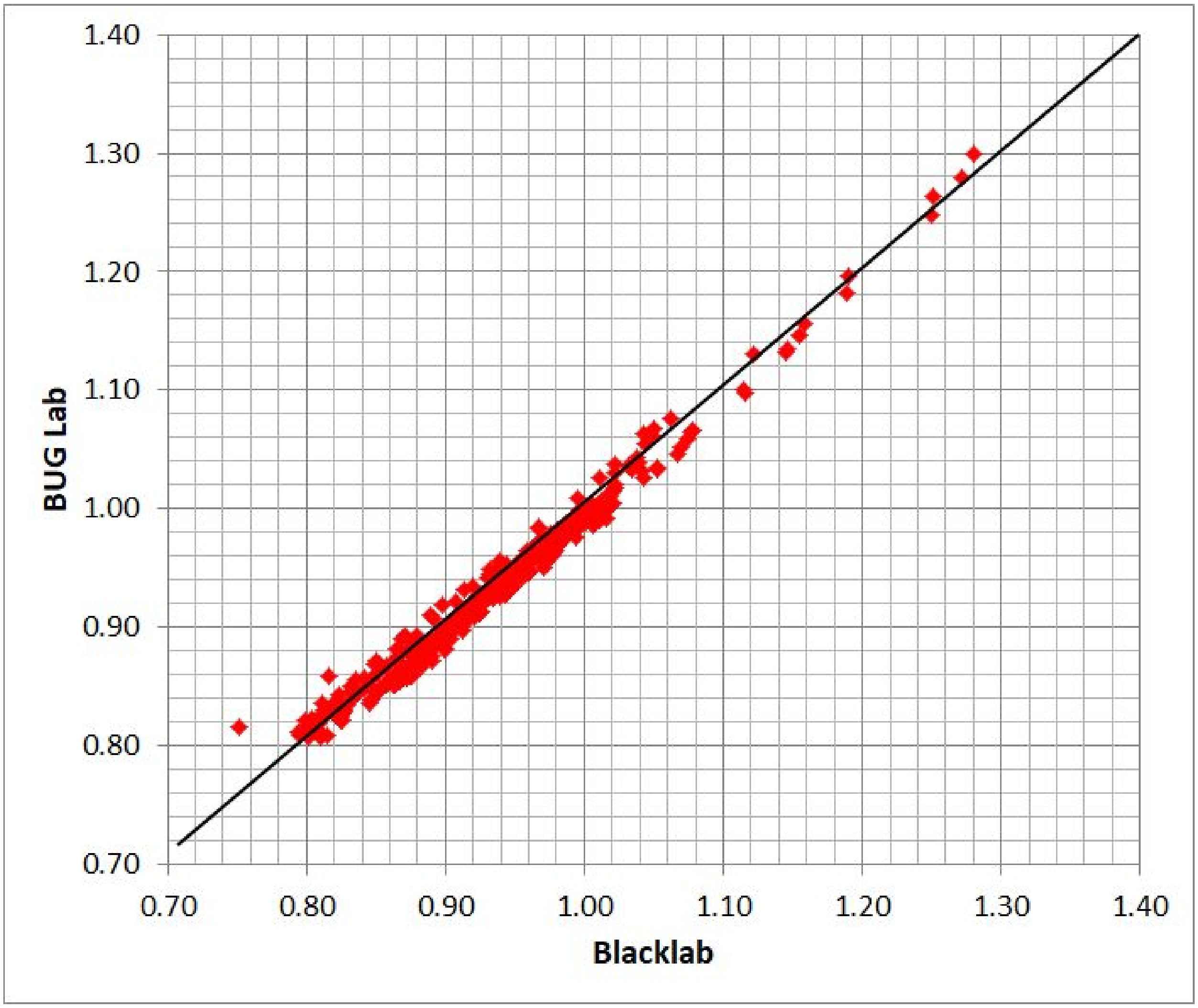

Figure 2.5: Comparison of Lambert Albedo spectralon measurements made on BUG and Blacklab from Shepard and Helfenstein (2011).

2.2 BUG Dataset

The BUG reflectance data are presented in terms of the Lambert Albedo. A Lambert surface has a constant Lambert albedo at all illumination and viewing geometries, and therefore represents the simplest surface BRDF model. Another useful surface BRDF model is the Lommel-Seeliger (L-S) model, which can be derived from radiative transfer theory under the assumption of an infinitely deep medium consisting of isotropically single scattering particles (i.e. no multiple scattering). The L-S albedo is related to the Lambert albedo through the following relation:

$$A_{L-S} = (\mu_0 + \mu)\, A_L \qquad (2)$$

Where $\mu = \cos e$ *(Shepard, 2017).*

Figures 2.3 and 2.6-2.9 show representative plots of the measured BUG Lambert albedos for the Apollo 11 and 16 samples. The results are presented in 3 different ways: contour plots using all the data; only data along the principal plane; and, only data perpendicular to the principal plane. The lunar BRDF's exhibit strong peaks in reflectance at low phase angles, which is a manifestation of the well-known lunar opposition effect (Hapke, 1993; Shepard, 2017). Figure 2.10 shows L-S albedos for the BUG Apollo 11 results in the principal plane. The general consistency of the L-S albedo peaks at g=0 suggests that the single scattering phase functions for soil particles are the dominant factor in determining the BRDF for the Apollo 11 soil sample. This is expected behavior for dark materials consisting of particles with low single scattering albedo, which reduces the effects of multiple scattering. (Hapke, 1993; Goguen,et al, 2010)

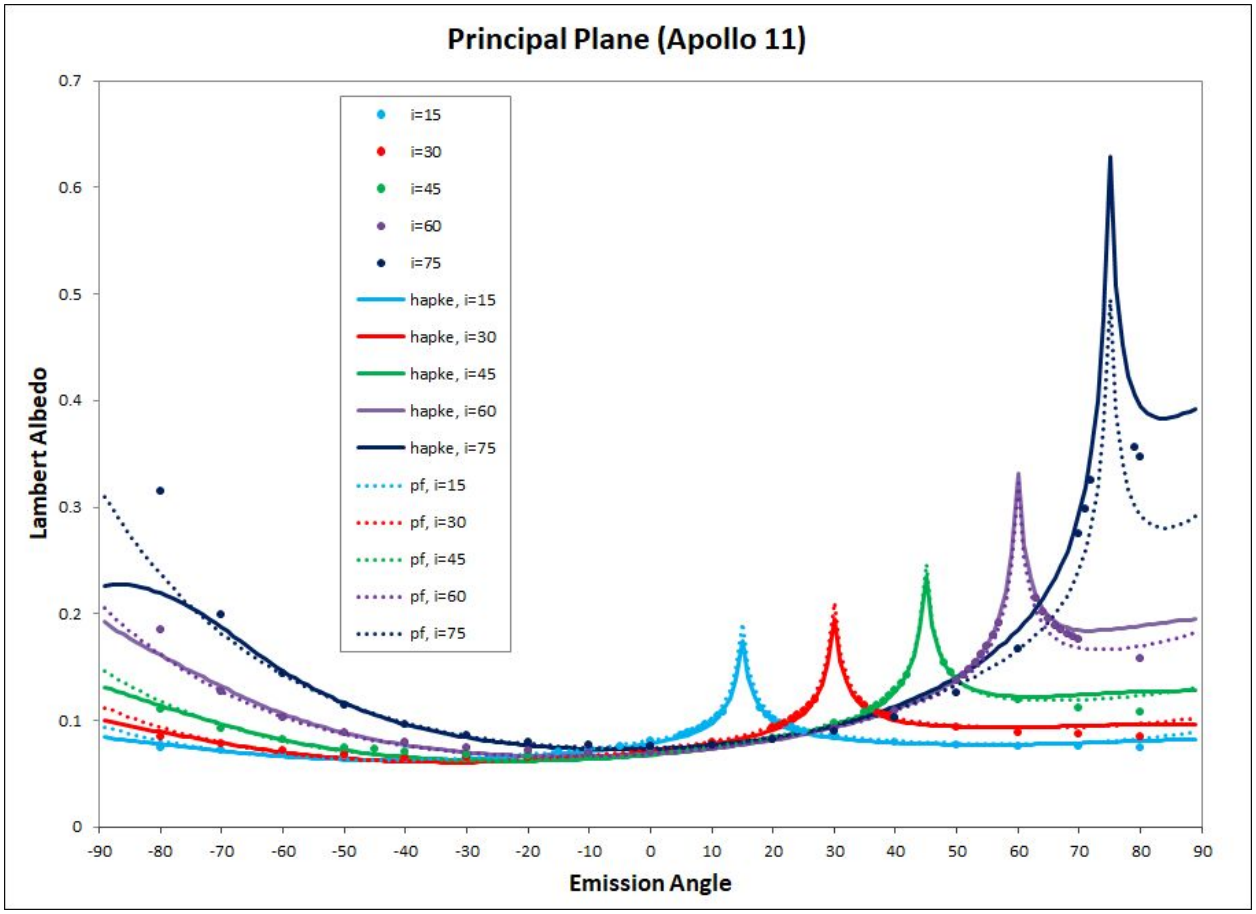

Figure 2.6: Lambert Albedo plots along the principal plane of the Apollo 11 BUG data (dots), Hapke (solid lines) and Simplified (dashed lines) functions using the best fit parameter values shown in Table 2 for the 750 nm wavelength datasets. Each color represents a different fixed incidence angle. Both functions fit the BUG data very well at low incidence angles and fit fairly well at the higher incidence angles.

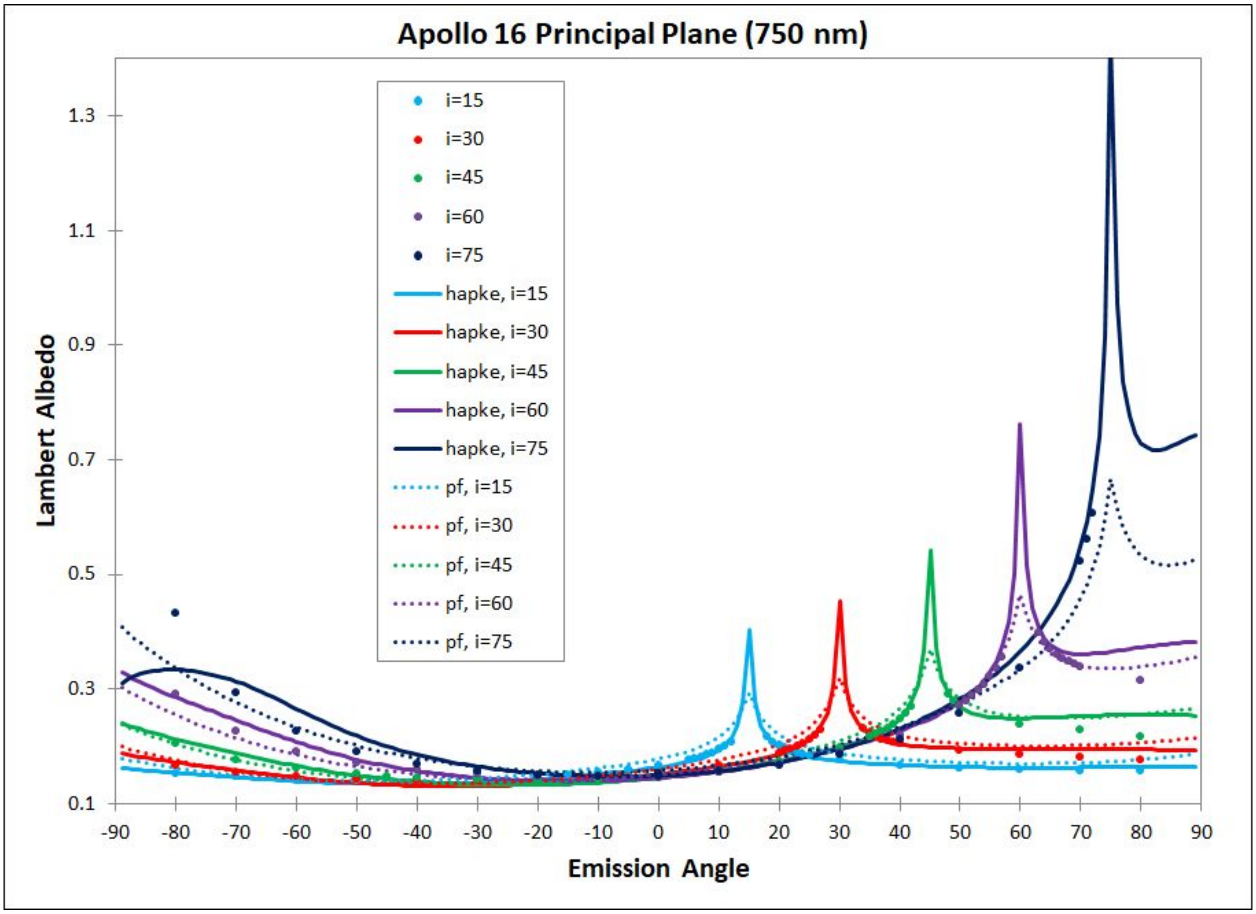

Figure 2.7: Lambert Albedo plots along the principal plane of the Apollo 68810 BUG data (dots lines), Hapke (solid lines) and Simplified (dashed lines) functions using the best fit parameter values shown in Table 2 for the 750 nm wavelength datasets. Each color represents a different fixed incidence angle. Both functions fit the BUG data very well at low incidence angles and fit fairly well at the higher incidence angles.

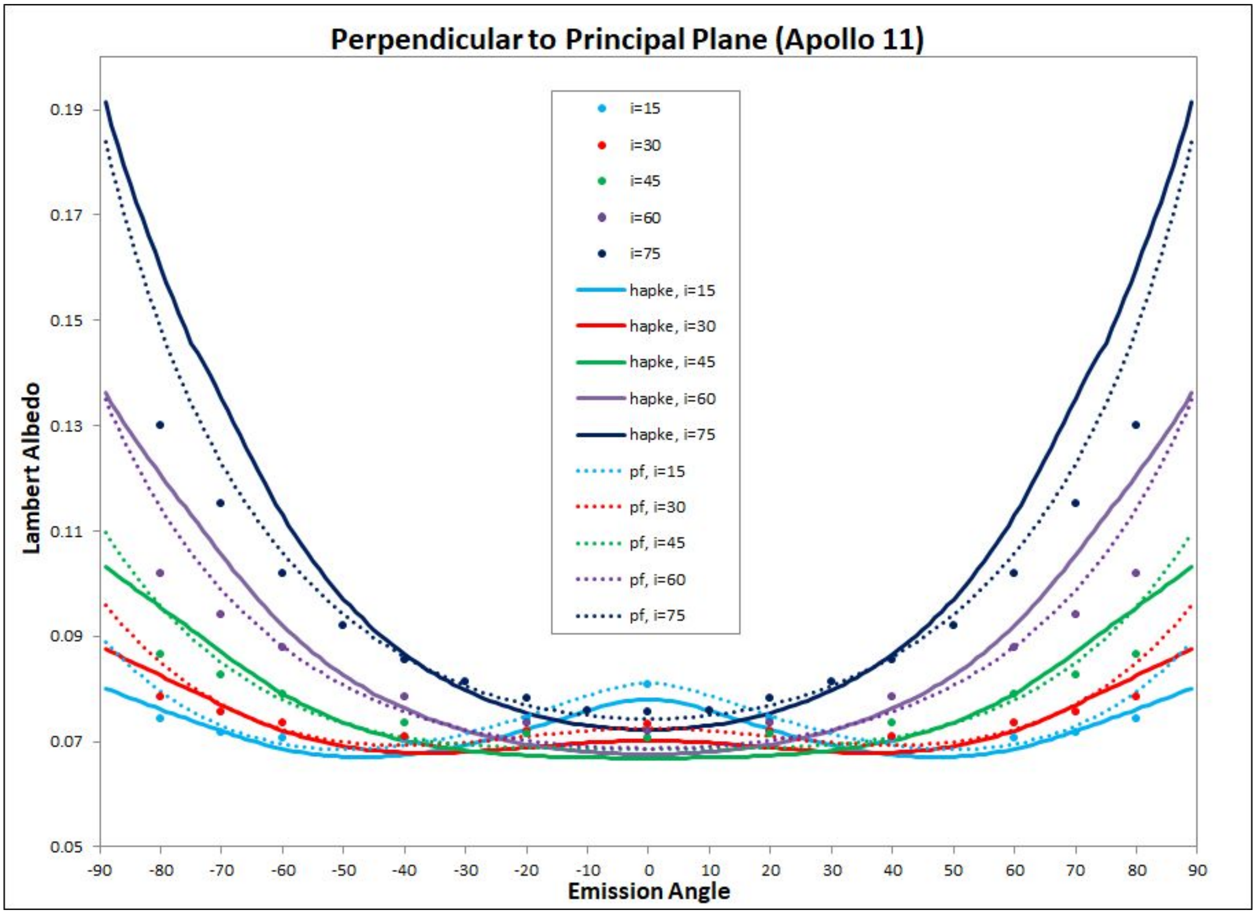

Figure 2.8: Perpendicular to Principal plane plots of the Apollo 11 BUG data (dots lines), Hapke (solid lines) and Simplified (dashed lines) functions using the best fit parameter values shown in Table 2 for the 750 nm wavelength datasets. Each color represents a different fixed incidence angle. Both functions fit the BUG data very well at low incidence angles, but overestimate at higher incidence angles, $i > 30°$.

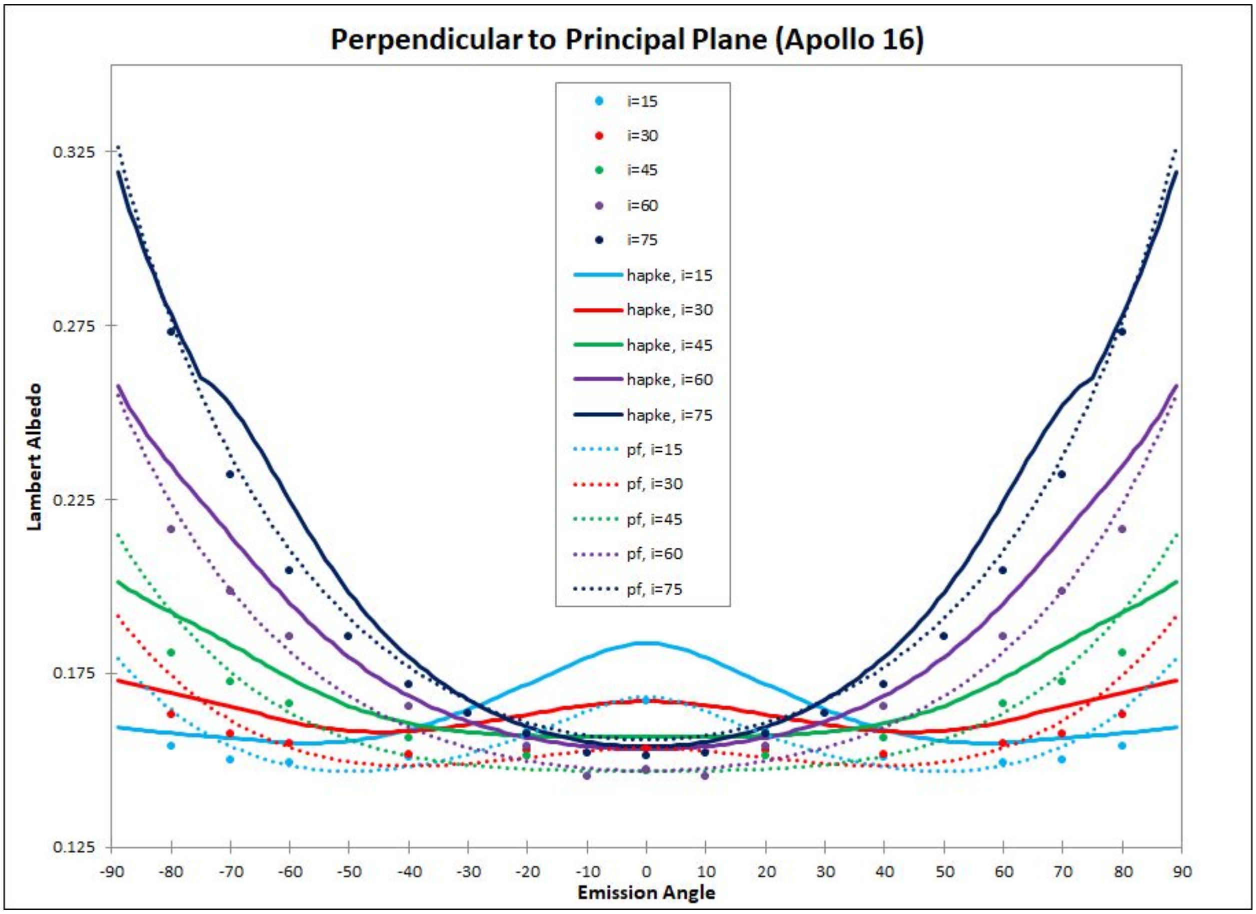

Figure 2.9: Perpendicular to Principal plane plots of the Apollo 16 BUG data (dots lines), Hapke (solid lines) and Simplified (dashed lines) functions using the best fit parameter values shown in Table 2 for the 750 nm wavelength datasets. Each color represents a different fixed incidence angle. Both functions fit the BUG data very well at low incidence angles and fit fairly well at the higher incidence angles.

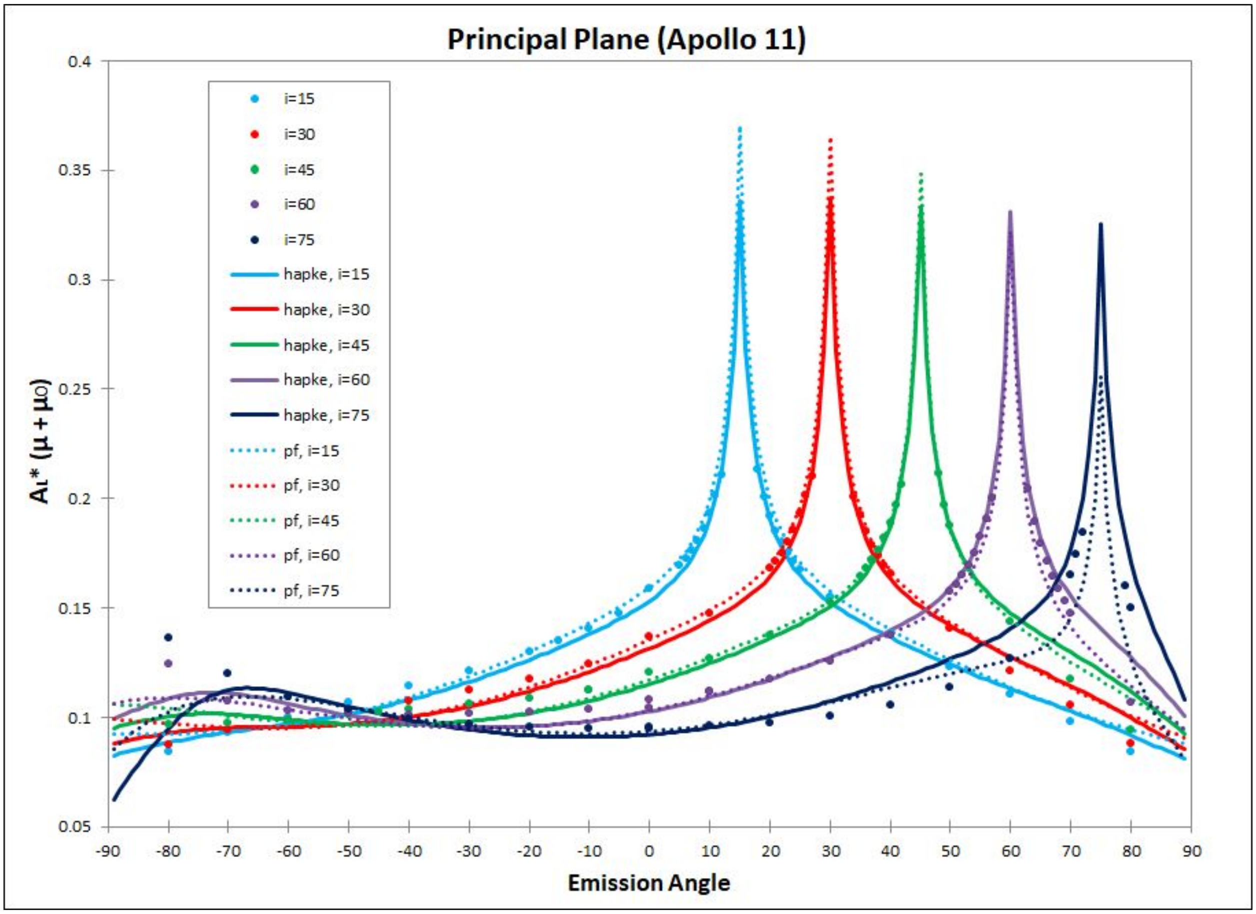

Figure 2.10: Lommel Seeliger-corrected albedo plots along the principal plane. The BUG data are represented as dots, the Hapke functions are shown as solid lines and the Simplified functions are displayed as dashed lines. Both functions were calculated using the best fit parameter values shown in table 2 for the 750 nm wavelength datasets. Each color represents a different fixed incidence angle. Both functions fit the BUG data very well at low incidence angles and do fairly well at higher incidence angles.

2.3 BRDF Models and Results

One of the main motivations for this work is to obtain a full BRDF and find a photometric model that fits the Apollo 11 and 16 BUG datasets. The model fits enable the calculation of BRDF's at any combination of photometric angles, and to determine the hemispheric bolometric reflectance. We chose two models to fit the BUG BRDF data - Hapke's

1993 BRDF model and a simplified empirical BRDF model that we developed specifically for this study.

2.3.1 Hapke Model We used Hapke's equation (12.55) (Hapke, 1993) for the bidirectional-reflectance distribution function (BRDF) of a rough surface. Hapke's models are based on a combination of radiative transfer modeling and empirical parameterizations. This version of Hapke's model was chosen because of its widespread use in the field, and because it was the least complex version that includes enough free parameters to obtain accurate fits. Hapke's 1993 BRDF equation (Equation 12.55) can be expressed in terms of the Lambert Albedo:

$$A_L = \frac{w}{4\mu_0} \frac{\mu_{0e}}{\mu_{0e} + \mu_e} \left\{ \left[(1 + B(g)p(g) + H(\mu_{0e})H(\mu_e) - 1) \right] S(i, e, g) \right\} \quad (3)$$

where w is the single scattering albedo, μ_{0e} and μ_e are the computed effective cosines of the incidence and emission angles accounting for surface roughness, $B(g)$ is a backscattering function for the opposition effect, $p(g)$ is the single scattering phase function, H are the Chandrasekhar (1960) "H" functions that account for multiple scattering, for which we employed Hapke's simplified equation 8.50, and $S(i,e,g)$ is a shadowing/visibility function, equation 12.50 (Hapke, 1993).

Following Johnson et al. (Johnson et al, 2006), we use:

$$B(g) = B_0/(1 + \frac{tan(g/2)}{h}) \quad (4)$$

and

$$p(g) = \frac{c(1-b^2)}{(1-2b\,cos(g) + b^2)^{3/2}} + \frac{(1-c)(1-b^2)}{(1+2b\,cos(g) + b^2)^{3/2}} \tag{5}$$

Where B_0 is the amplitude of the shadow hiding opposition surge and h is the angular width of the shadow hiding opposition surge. *p(g)* is approximated as the 2-term Henyey-Greenstein function. Where *c* represents the backward scattering fraction and *b* is the asymmetry parameter.

2.3.2 Simplified Empirical Model We have developed a simplified empirical function that yields BRDF behavior that is similar to Hapke's, but is significantly less computationally intensive. The Simplified Empirical BRDF Model is:

$$A_L = \frac{2X}{(\mu_0 + \mu + Y)} \frac{1}{\mu_0} (1 + B(g))p(g) \tag{6}$$

where μ_0 is the cosine of the actual incidence angle and μ is the cosine of the actual emission angle, and *X* and *Y* are empirical constants. *X* is a multiplicative factor that determines the overall reflectance, and *Y* prevents the function from blowing up at high phase angles when μ_0 and μ are small. *B(g)* is the same as Equation 4 above. Like the Hapke models, the simplified empirical model satisfies the Helmholtz reciprocity principle in that exchanging μ_0 for μ results in an equation is mathematically equivalent (Minnaert, 1941), but it ignores multiple scattering and shadow hiding Hapke terms in his original equation.

2.3.3 BRDF Results We successfully fit the BUG data with the two BRDF models described above using a fitting procedure in which we selected a range of parameter values and time step for each parameter and tried every combination until the sum of squares was minimized. As shown in Table 2.2, we obtained best fit reduced chi-squared χ^2_v values between 0.2 and 0.3, which indicates that the data are well fit by both models. The χ^2_v values for the Apollo 16 data are systematically lower than those for Apollo 11, due to the fact that we likely overestimated the uncertainty in the BUG data for the brighter Apollo 16 sample. We assumed that each of the BUG measurements had the same uncertainty value and the absolute systematic error was 4% (**σ**=0.04) , based on Johnson et al., 2013. Although, according to Sheppard and Helfenstein, 2007 the uncertainties in the high emission BUG data (i=60º, e=80º) tend to be 5-10% larger.

Recognizing that derived parameters from Hapke's model are non unique (Shepard and Helfenstein, 2007), we employed it because of its wide use in the field, and because it has enough free parameters to obtain accurate fits. The average single scattering albedos (*w*) for the Mare Apollo 10084 sample is 0.32 and for the highlands Apollo 68810 and 61141 samples are 0.54 and 0.58, respectively. All of the values for our Hapke fits are shown in Table 2.2. Johnson et al. (2013) used a similar Hapke model to fit the same BUG measurements and computed Hapke values that are similar to ours. Both Apollo samples and Hapke fits to the BUG data show decreasing c values (greater forward scattering) and increased b values with wavelength. (Johnson et al, 2013).

Table 2.2: Best fit parameters for the Apollo 11 (top) and Apollo 16 (bottom) 450, 550, 750 and 950 nm BUG Data using the Hapke BRDF and a simplified BRDF.

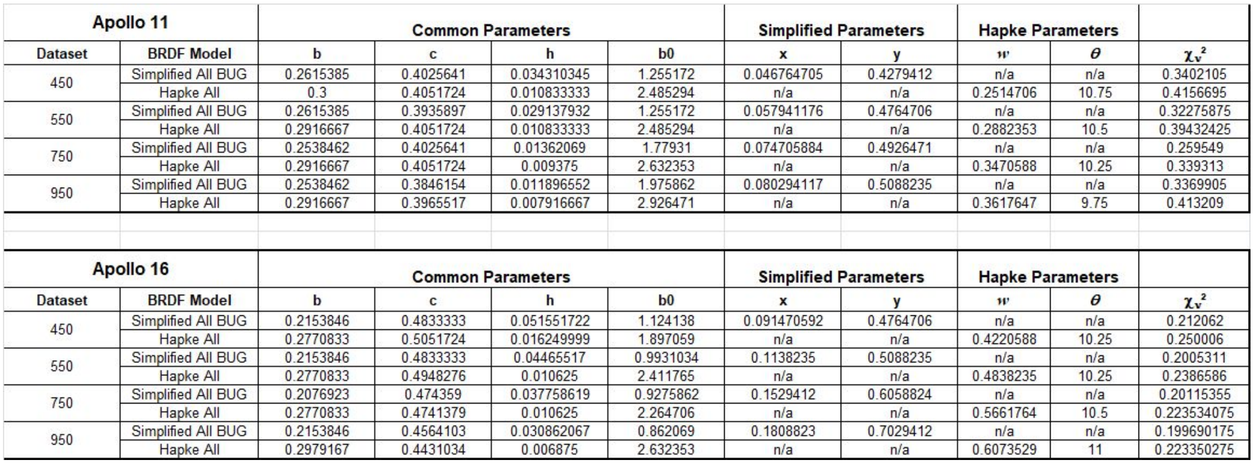

Apollo 11		Common Parameters				Simplified Parameters		Hapke Parameters		
Dataset	BRDF Model	b	c	h	b0	x	y	w	θ	χ_v^2
450	Simplified All BUG	0.2615385	0.4025641	0.034310345	1.255172	0.046764705	0.4279412	n/a	n/a	0.3402105
	Hapke All	0.3	0.4051724	0.010833333	2.485294	n/a	n/a	0.2514706	10.75	0.4156695
550	Simplified All BUG	0.2615385	0.3935897	0.029137932	1.255172	0.057941176	0.4764706	n/a	n/a	0.32275875
	Hapke All	0.2916667	0.4051724	0.010833333	2.485294	n/a	n/a	0.2882353	10.5	0.39432425
750	Simplified All BUG	0.2538462	0.4025641	0.01362069	1.77931	0.074705884	0.4926471	n/a	n/a	0.259549
	Hapke All	0.2916667	0.4051724	0.009375	2.632353	n/a	n/a	0.3470588	10.25	0.339313
950	Simplified All BUG	0.2538462	0.3846154	0.011896552	1.975862	0.080294117	0.5088235	n/a	n/a	0.3369905
	Hapke All	0.2916667	0.3965517	0.007916667	2.926471	n/a	n/a	0.3617647	9.75	0.413209

Apollo 16		Common Parameters				Simplified Parameters		Hapke Parameters		
Dataset	BRDF Model	b	c	h	b0	x	y	w	θ	χ_v^2
450	Simplified All BUG	0.2153846	0.4833333	0.051551722	1.124138	0.091470592	0.4764706	n/a	n/a	0.212062
	Hapke All	0.2770833	0.5051724	0.016249999	1.897059	n/a	n/a	0.4220588	10.25	0.250006
550	Simplified All BUG	0.2153846	0.4833333	0.04465517	0.9931034	0.1138235	0.5088235	n/a	n/a	0.2005311
	Hapke All	0.2770833	0.4948276	0.010625	2.411765	n/a	n/a	0.4838235	10.25	0.2386586
750	Simplified All BUG	0.2076923	0.474359	0.037758619	0.9275862	0.1529412	0.6058824	n/a	n/a	0.20115355
	Hapke All	0.2770833	0.4741379	0.010625	2.264706	n/a	n/a	0.5661764	10.5	0.223534075
950	Simplified All BUG	0.2153846	0.4564103	0.030862067	0.862069	0.1808823	0.7029412	n/a	n/a	0.199690175
	Hapke All	0.2979167	0.4431034	0.006875	2.632353	n/a	n/a	0.6073529	11	0.223350275

Examples of BRDF model Lambert albedos are shown in Figures 2.11 and 2.12. The principal plane results are shown in Figures 2.6, 2.7 and 2.10 and the off principal plane results are shown in figures 2.8 and 2.9. The results show that both approaches can satisfactorily fit the BUG data. This is not completely unexpected, given the similarities between the functions and their input parameters, and the fact that the BRDF for dark lunar soil is likely to be dominated by the single scattering phase functions of the individual soil particles. However, both BRDF models tend to somewhat underestimate the BUG data when incidence and emission angles are both high, which is due to the fact that most of the fitted data were acquired at lower incidence angles.

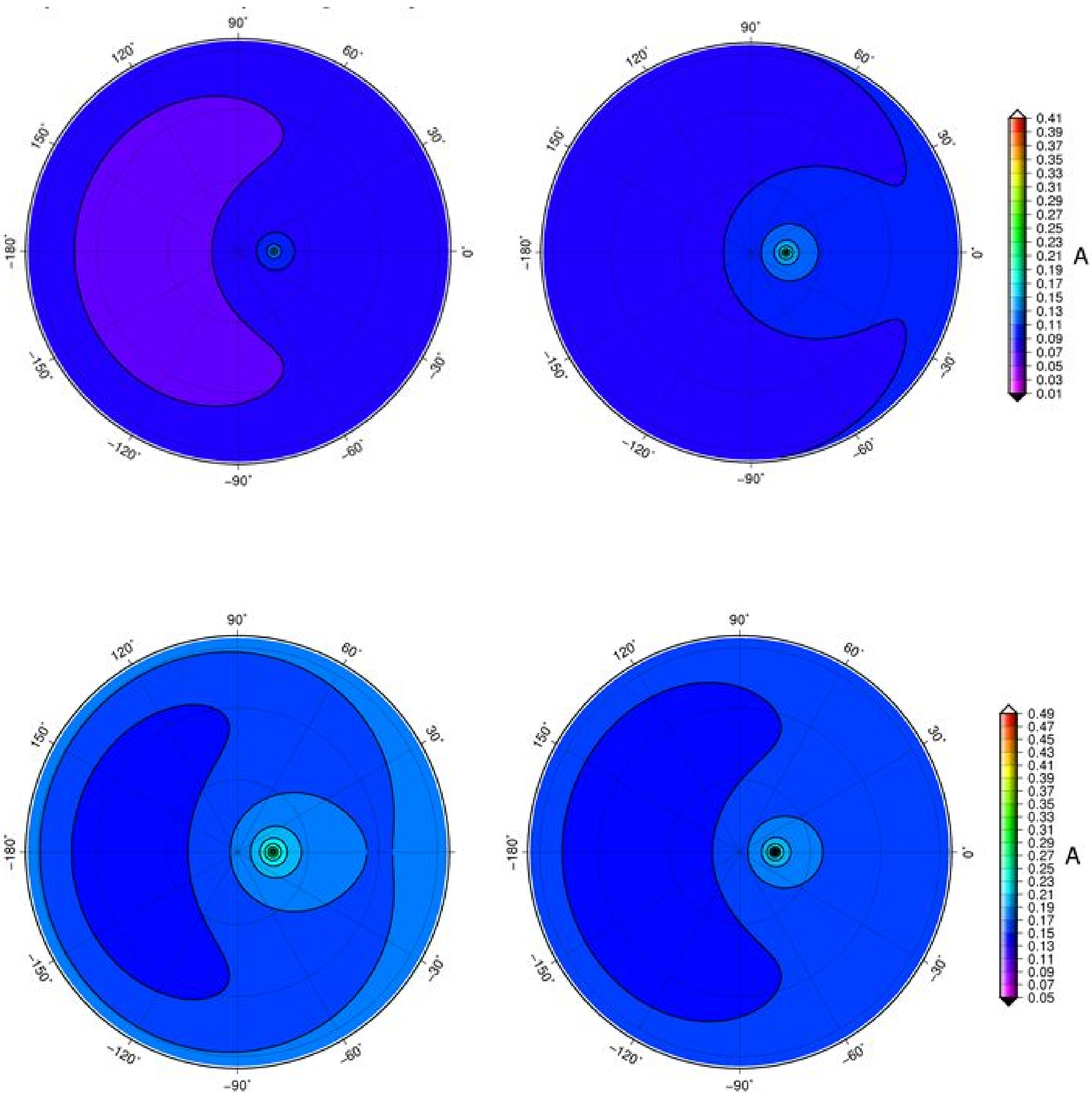

Figure 2.11: Polar contour plots of modeled Lambert Albedo (A) at i=15, of the Hapke (left plots) and Simplified (right plots) functions using the best fit parameter values shown in Table 2 for the 750 nm wavelength datasets. Emission is the radial coordinate and ψ is the azimuthal coordinate. The scales used here are the same as shown above for the BUG data. The top two plots were made by fitting models to the Apollo 11 data and the bottom two plots represent the Apollo 16 data.

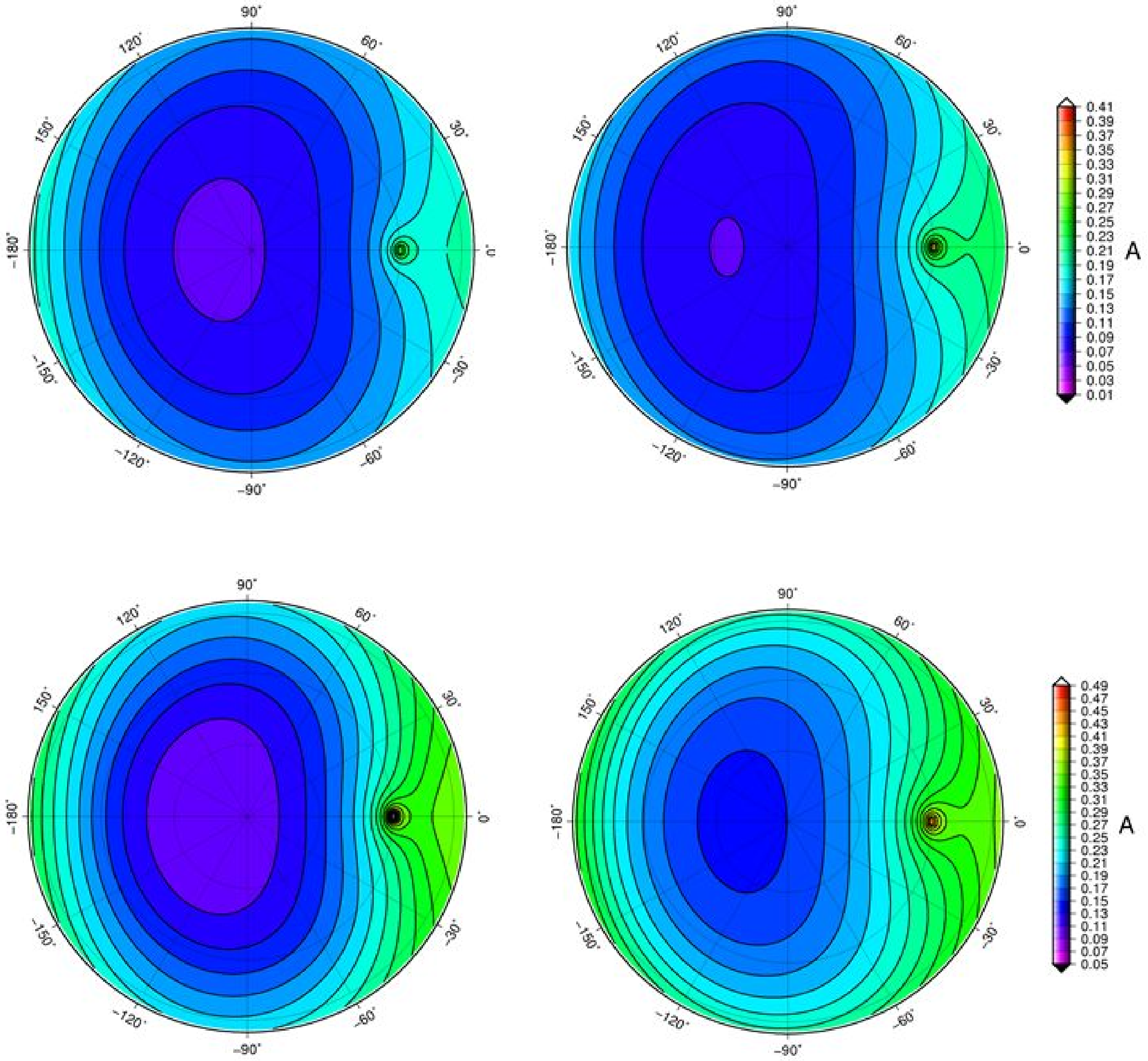

Figure 2.12: BRDF polar contour plots, at i=60, of Apollo 11 (top plots) and Apollo 16 (bottom plots) of the Hapke and Simplified functions using the best fit parameter values shown in Table 2 for the 750 nm wavelength datasets. The colors represent Lambert albedo, e is the radial coordinate and ψ is the azimuthal coordinate.

2.4 Solar Spectrum Averaged Hemispheric Albedo Results

The heat balance of the lunar surface is controlled by the solar spectrum averaged hemispheric albedo, which is sometimes referred to as the bolometric albedo, or the directional hemispheric reflectance. We determine the directional hemispheric albedo, A_h, as a function of incidence angle at each measured BUG wavelength, using Hapke's equation 10.10:

$$A_h(i) = \pi \int_{2\pi} A_L(i, e, g) \mu d\Omega_e \tag{7}$$

where $d\Omega_e = sin\ e\ ded\psi$ and Ψ is the azimuth angle. To calculate solar spectrum average directional hemispheric albedoes, we calculated appropriate spectral boundaries and solar spectrum weighting factors for each BUG filter and linearly extrapolated the directional hemispheric albedos for wavelengths shorter than 450nm and for wavelengths longer than 950nm based on published measurements of lunar soil spectral reflectance in these wavelength ranges (Ohtake et al, 2013; Izawa et al., 2014). Solar spectrum integration parameters shown in Table 2.3 are based on the ASTM E490-00a (ASTM International, 2014) solar spectrum data. The best fit Hapke values that we used to calculate the bolometric reflectance curves are shown in Table 2.4.

Table 2.3: Solar spectrum integration parameters employed for the calculation of A_h. Stars indicate wavelength ranges for linearly extrapolated directional hemispheric albedos.

Filter (nm)	Minimum Value (nm)	Maximum Value (nm)	Weighting Factor
200*	0	250	0.00152768008
300*	250	350	0.0379378349
450	350	500	0.174775004
550	500	650	0.196715966
750	650	850	0.186839342
950	850	1100	0.144279152
1250*	1100	1400	0.101405241
1600*	1400	1800	0.0735787377
2000*	1800	2250	0.037638206
2500*	2250	1000000	0.0453027375

Table 2.4. Derived Hapke solar-spectrum averaged parameters

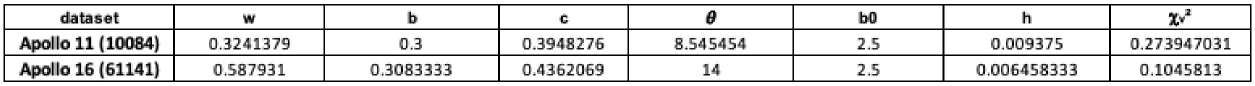

dataset	w	b	c	θ	b0	h	χ_v^2
Apollo 11 (10084)	0.3241379	0.3	0.3948276	8.545454	2.5	0.009375	0.273947031
Apollo 16 (61141)	0.587931	0.3083333	0.4362069	14	2.5	0.006458333	0.1045813

Figure 2.13 shows the solar spectrum averaged hemispheric albedos for the Apollo 11 and 16 BUG measurements as a function of incidence angle. We fit 2nd-order quadratic functions to the standard mare soil sample (Apollo sample 10084) and to the standard highlands sample (Apollo sample 61141) for $A_L(i)$ where i is in degrees. The second order polynomial fit for the mare Apollo sample 10084 is:

$$A_h(i) = 9.4032 * 10^{-6} i^2 - 1.8345 * 10^{-4} i + 0.068061 \quad (8)$$

The second order polynomial fit for the lightest highlands Apollo sample (Apollo 16) is:

$$A_h(i) = 1.3299 * 10^{-5} i^2 - 1.0248 * 10^{-4} i + 0.14382 \qquad (9)$$

Also included on the same plot are Keihm's (1984) model and Vasavada's (1999 and 2012) models for the same quantity. The functional dependence of albedo on solar incidence angle previously published by Keihm and Vasavada (Keihm, 1984) and (Vasavada, 1999 & 2012) is:

$$A_h(i) = A_0 + a(i/45)^3 + b(i/90)^8 \qquad (10)$$

The parameter values that Keihm used are constrained for the entire lunar surface as $A_0=0.12$, $a = 0.03$, $b = 0.14$. Vasavada (2012) splits the lunar surface into two bolometric hemispherical reflectance functions; mare: $A_0=0.07$, $a=0.045$, $b=0.14$ and highlands: $A_0 = 0.16$, $a = 0.045$, $b=0.14$.

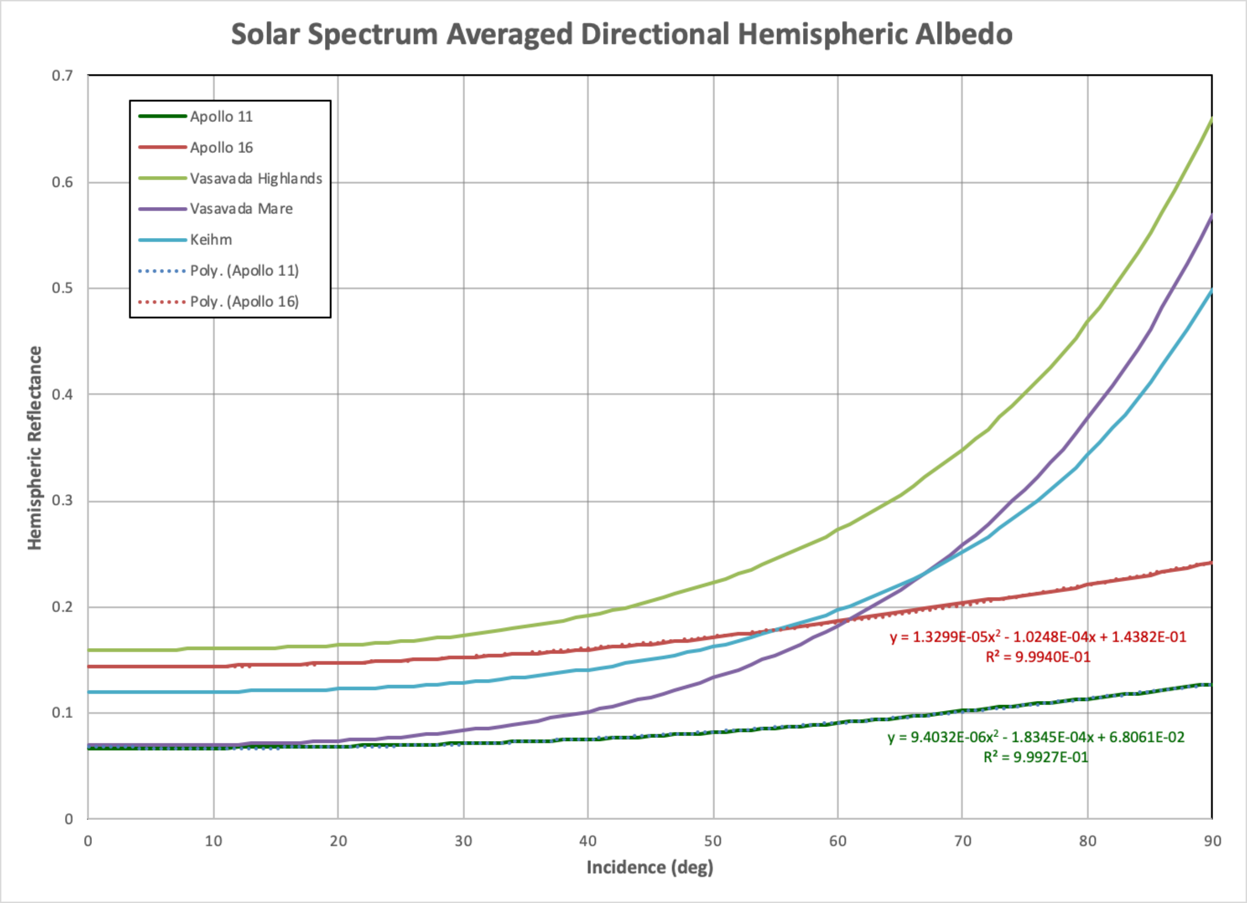

Figure 2.13 Solar spectrum averaged hemispheric albedos (A_h) as a function of solar incidence angle. Shown are our best-fits based on our BUG measurements of Apollo samples, as well as the parameterizations used by Keihm (1994), and Vasavada (1999, 2012). Also shown are our best fit quadratic functions for $A_h(i)$ for our Apollo 11 and Apollo 16 samples.

As shown in figure 2.13, the hemispheric reflectance functions derived from our laboratory measurements of the Apollo soil samples display relatively flat curves with increasing incidence angles, while the functions employed by Keihm and Vasavada dramatically increase beyond 50 degree incidence angle. For example, the absolute difference between their models and our measurements of both Apollo samples at 60 degrees is 0.1. Keihm's ($A_0=0.12$) and Vasavada's ($A_0=0.07$ for the mare regions and $A_0=0.16$ for highlands) models have higher initial albedo values than what we measured at normal illumination conditions ($A_0=0.0644$ for the mare

Apollo 11 samples and $A_0=0.14$ for highlands Apollo 16 sample). The impacts of these differences on thermal model results are described in later sections.

2.5 Diviner Bolometric Brightness Temperature Measurements

We determined normal bolometric brightness temperatures from the Apollo 11 and Apollo 16 sample sites using data acquired by Diviner. The bolometric brightness temperature provides a means of characterizing wavelength-integrated thermal emission measurements in terms of an equivalent blackbody emitter (Paige et al. 2010b). Since lunar surface temperatures are close to being in radiative equilibrium during the daytime, measured bolometric brightness temperatures may provide a useful check on models for the hemispheric albedo.

Precise locations for the Apollo sampling stations have been determined by the LRO LROC team (http://www.lroc.asu.edu/), and we found the coordinates of our sampling sites using the online Quickmap tool in conjunction with Apollo-era maps provided in the Handbook of Lunar Soils (1993). Our coordinates for the Apollo 11 sample are (0.67370546°N, 23.4724216°E) and for our Apollo 16 sample are (-9.0687°N, 15.4755°E). We retrieved all Diviner data obtained between July 2009 and August, 2016 in Channels 3-9 with $0° < e < 5°$ within 30 km latitude/longitude boxes centered at these locations and binned them at a resolution of 0.25 hours in local time. The chosen sizes of the latitude/longitude boxes was the result of a tradeoff between the desire for high spatial resolution and the desire for high local time resolution and coverage. We then computed bolometric brightness temperatures as described by Paige et al., (2010b). We also computed a small correction to the daytime bolometric brightness temperatures (obtained between 6 and 18 hours local time) to account for the ~7% annual variation in the solar flux due to the eccentricity of the Earth's orbit around the Sun by multiplying the bolometric thermal emission by the square of of the Sun-Earth distance in AU. The seasonal effects due to the small (1.54°) obliquity of the Moon are negligible at these latitudes so no correction was applied for this. The relationship between the corrected bolometric brightness temperatures, T_{BolC} and the measured T_{bol} values is:

$$\sigma T^4{}_{BolC} = \sigma T^4{}_{Bol} R^2{}_{\oplus} \tag{11}$$

Where $R_{\oplus}$ is the Sun-Earth distance in AU. The resulting T_{BolC} values for Apollo 11 and Apollo 16 $R_{\oplus}<1$ (close) and $R_{\oplus}>1$ (far) are shown in Figures 2.14 and 2.15.

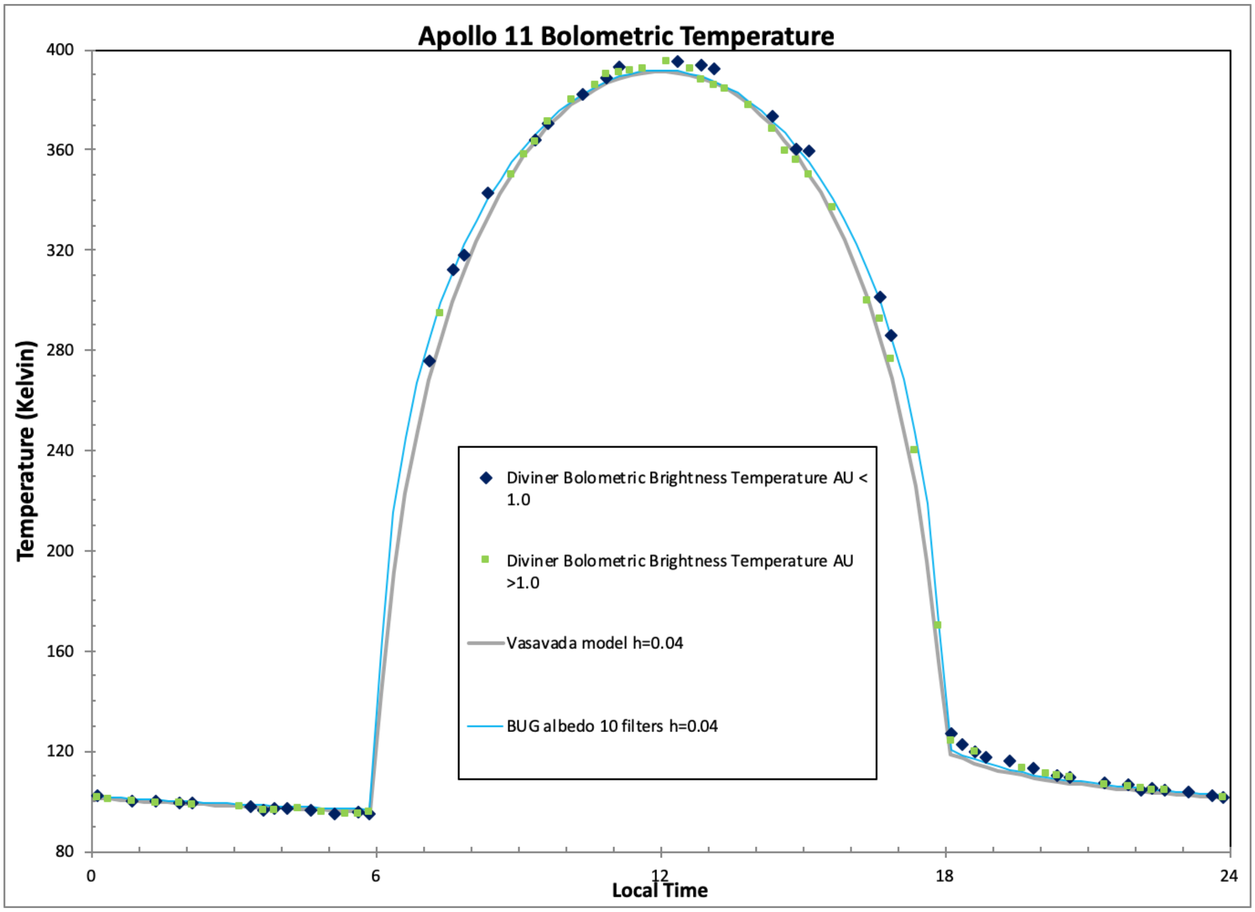

Figure 2.14. Diviner measurements of normal bolometric brightness temperatures for Apollo 11 along with the results of thermal model calculations assuming our BUG albedo model functions from figure 13 for $A_h(i)$ those used by Vasavada et al., (2012) for equatorial lunar maria.

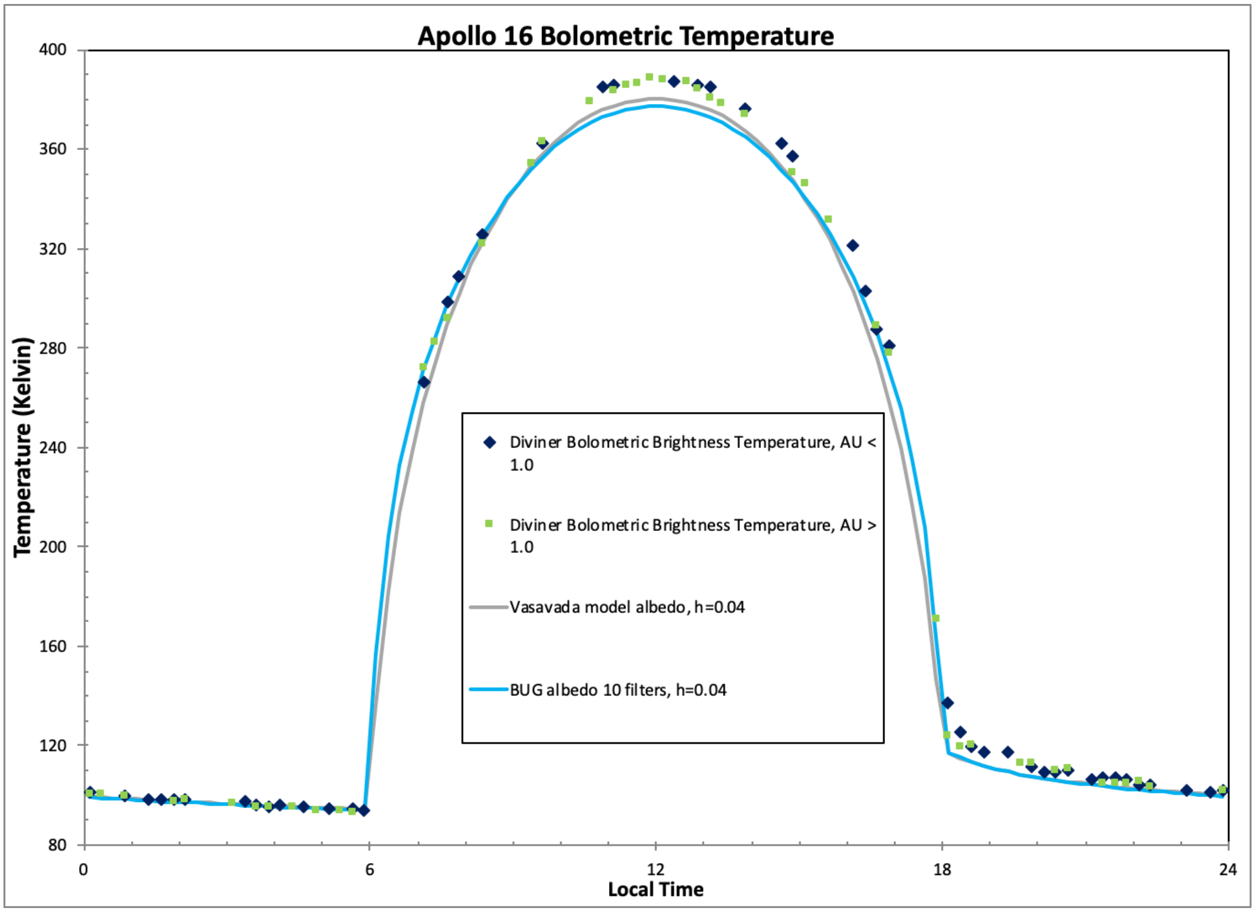

Figure 2.15. Diviner measurements of normal bolometric brightness temperatures for Apollo 16 along with the results of thermal model calculations assuming our Simplified model functions from figure 13 for $A_h(i)$ and those used by Vasavada et al., (2012) for equatorial lunar highlands.

2.6 Thermal Model Results

We employed a thermal model that is equivalent to the model described by Hayne et al. (2017) to calculate bolometric brightness temperatures to compare with the Diviner data. The model surface heat balance equation can be written as:

$$K\frac{\partial T}{\partial z} + (1 - A_h(i))S = \varepsilon\sigma T^4 \qquad (12)$$

where K is the thermal conductivity, $\frac{\partial T}{\partial z}$ is the vertical temperature gradient at the surface, S is the incident solar flux, ε is the hemispherically integrated bolometric surface infrared emissivity, σ is the Stefan Boltzmann Constant, and T is the surface temperature. Following the work of Bandfield et al. (2015), we calculate surface temperatures using a hemispherically integrated bolometric emissivity of $\varepsilon = 0.951$. To calculate bolometric brightness temperatures for normal viewing geometry to compare with the Diviner measurements described in the previous section, we use an emissivity at e=0° of 0.99 as recommended by Bandfield et al., (2015).

Because we use prescribed values for $A_h(i)$ based on our simplified fits to our laboratory reflectance measurements (Equations 8 and 9), the only remaining free parameter in the model is the H-parameter, which is the characteristic depth scale in centimeters over which the density of the lunar regolith transitions from a density of 1100 kg m^{-3} at the surface to 1800 kg m^{-3} at depth (Hayne et al., 2017). The H-parameter provides a means of gradually varying the thermal conductivity of the uppermost regolith layers. During the day, the lunar surface is close to being in radiative equilibrium, and the H-parameter does not strongly influence calculated surface temperatures. However, during the night when insolation is zero, the H-Parameter strongly influences surface temperatures, with higher H-parameter values resulting in lower nighttime surface temperature (Hayne et, al, 2017). Our fitting procedure involved varying the H-parameter to fit the Diviner nighttime bolometric brightness temperatures, but no effort was made to fit the Diviner daytime data.

Plots of our model-calculated normal bolometric brightness temperatures of the Apollo 11 and 16 sites using our simplified albedo parameterization are shown in Figures 2.14 and 2.15. Also shown for comparison are normal bolometric brightness temperatures calculated using the

Vasavada et al papers (1999, 2012) maria and highlands albedo parameterizations. We found that using an H-Parameter of 0.04m provided a best fit to the nighttime data in all cases. The average difference between our model-calculated normal bolometric brightness temperatures and the Diviner data for the Apollo 11 lunar soil is +0.11K. The average difference for Apollo 16 lunar soil is -2.56K. The average differences in the Diviner data and Vasavada's calculated temperatures for the Apollo sites are, -4.65K for the Apollo 11 lunar soil and -8.67K for the Apollo 16 lunar soil. The Vasavada albedos do not fit the data as well, but they were derived from a large sampling of equatorial maria and highland regions and are not optimized to provide an exact fit at the Apollo 11 and 16 sampling sites. Furthermore, Vasavada et al (2012) fit Diviner Channel 7 brightness temperatures whereas we fit Diviner Bolometric brightness temperatures. Bandfield et al (2015) showed that lunar surface roughness results in significantly elevated brightness temperatures at shorter wavelengths in the morning and afternoon. This causes Diviner bolometric temperatures to be higher than Channel 7 brightness temperatures in the morning and afternoon and thus explains why we require lower albedos than Vasavada et al (2012) to accurately fit them.

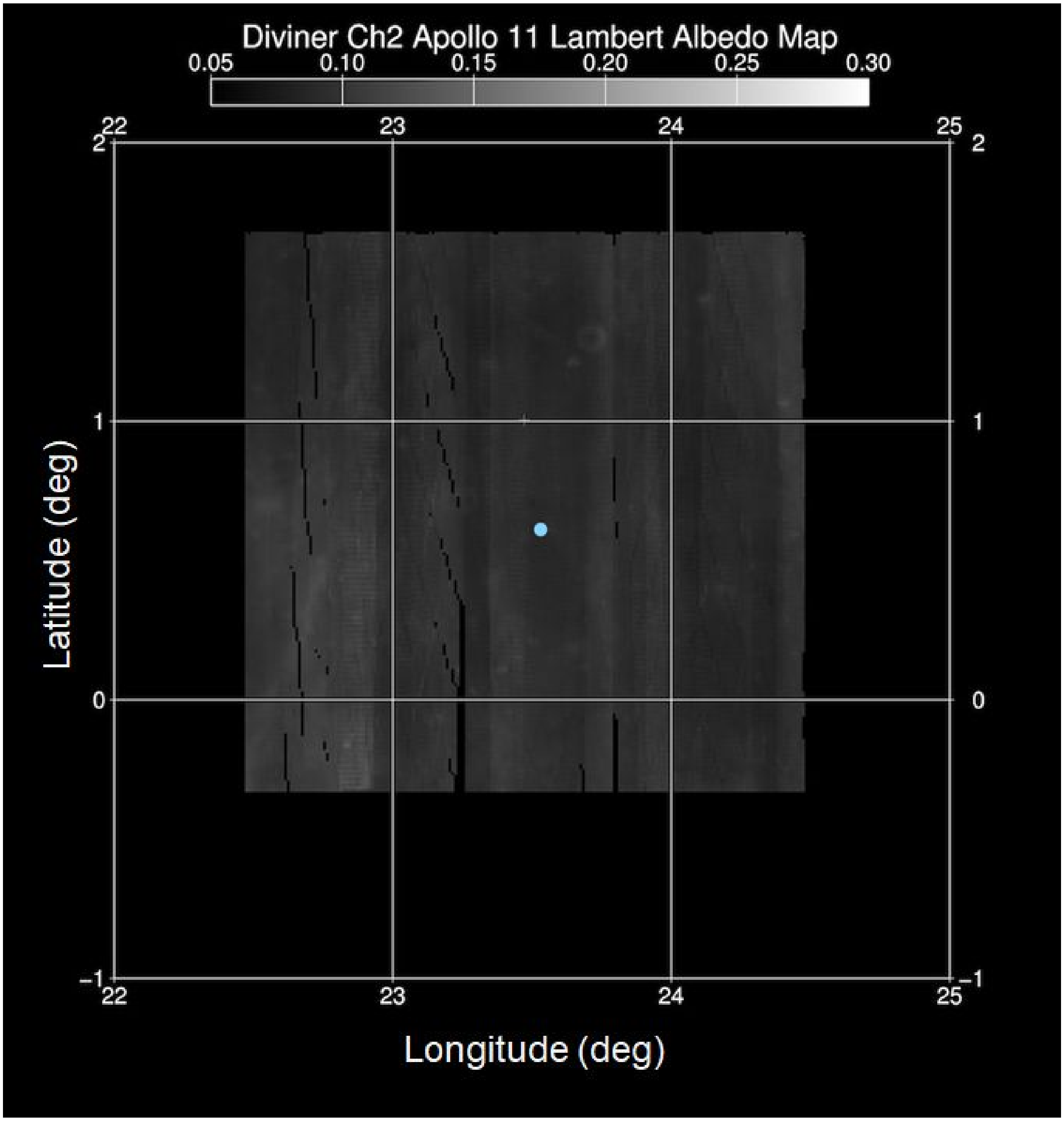

Figure 2.16 Diviner Lambert Albedo Map of the Apollo 11 sample site area. The maps include Diviner Channel 2 data acquired from July 2009 - January 2017 for 0<*i*<25° and 0<*e*<10°. The blue dot indicates the sample location for lunar soil sample 10084. The landing site and surrounding areas appear to have homogenous reflectance properties.

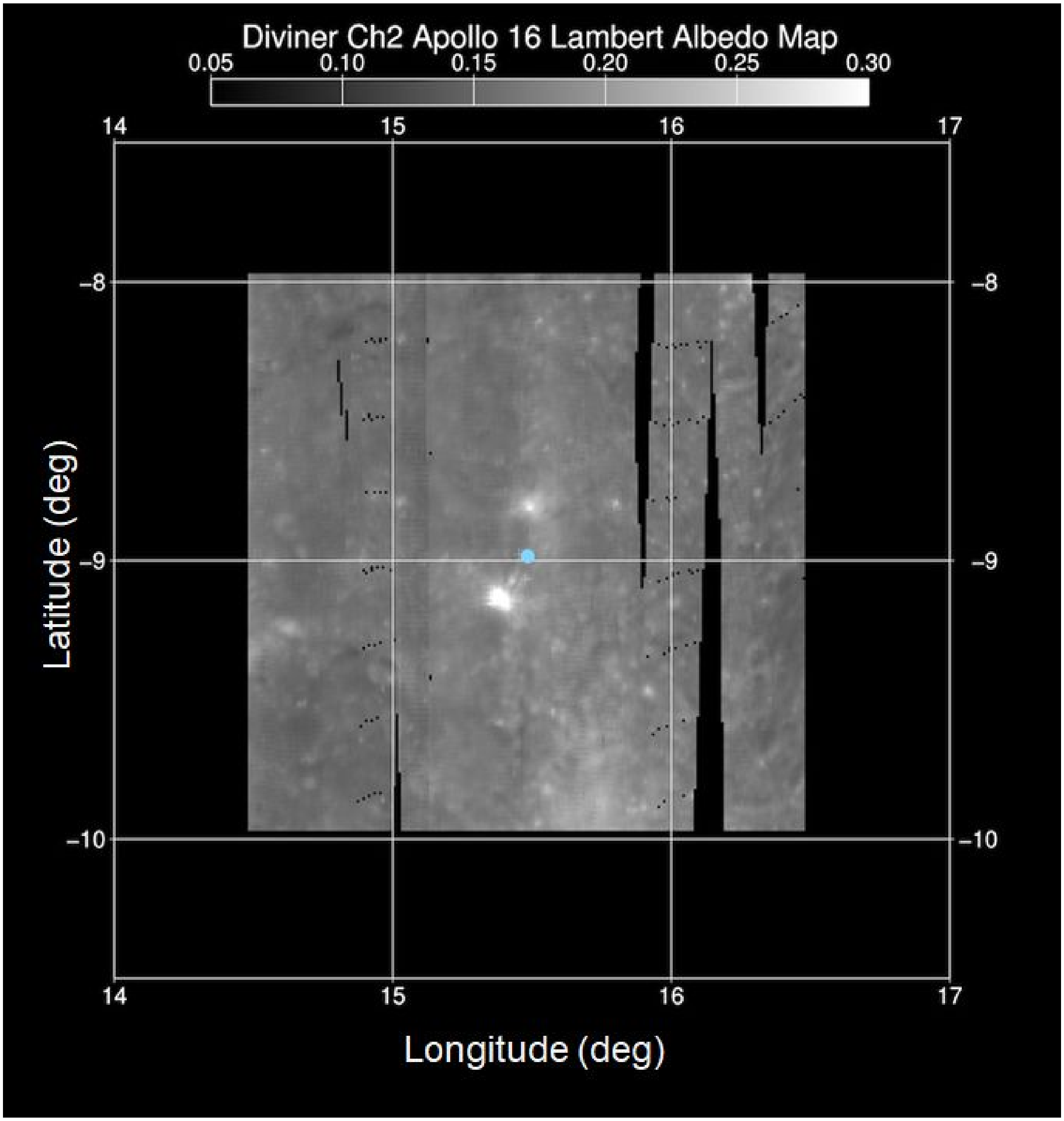

Figure 2.17. Diviner Lambert Albedo Map of the Apollo 16 sample site area. The maps include Diviner Channel 2 data acquired from July 2009 - January 2017 for 0<*i*<25° and 0<*e*<10°. The blue dot indicates the sample location for lunar soil sample 61141 and 68810. The Apollo 16 field site, which contained a number of fresh bright ray craters, was considerably more diverse than Apollo 11.

2.7 Discussion

In total, the measurements and models we present here paint a self-consistent end-to-end picture of the solar-spectrum averaged reflectance properties of the Apollo 11 soil. Our well-calibrated bidirectional reflectance measurements of the Apollo 11 soil samples yielded solar-spectrum averaged hemispheric reflectances that produced thermal model-derived daytime bolometric brightness temperatures that are in good agreement with those measured by the well-calibrated Diviner instrument. This suggests that differences in the compaction states or the surface textures of our laboratory samples versus those on the natural lunar surface were not a significant factor for the case of Apollo 11. Our analysis of our goniometer BRDF measurements for Apollo 11 soil only yield a modest increase in A_h at higher incidence angles, whereas previous models have used parameterizations that imply that A_h increases very rapidly at higher incidence angles (Figure 2.13). Examination of the original Birkeback et al. (1970) Apollo 11 soil integrating sphere measurements shows only a 40% increase in albedo between i=20° and i=60°. Our goniometer results for the same sample imply 35% increase between i=20° and i=60°, which is generally consistent. However, the Vasavada et al., (1999 and 2012) albedo parameterizations, which are based on the original model of Keihm (1984), imply a 240% increase in A_h between i=20° and i=60°. Furthermore, the Birkeback et al. (1970) measurements only go as high as i=60°, so the Keihm (1984) albedo parameterization at higher incidence angles is an extrapolation.

The measurements and models we present here for Apollo 16 are not as self-consistent as those for Apollo 11. As shown in Figure 2.14, our thermal model-calculated bolometric brightness temperatures at mid-day are distinctly lower than measured by Diviner, which implies that the Apollo 16 sample had a higher hemispheric albedo than the natural lunar surface. The solar incidence angle at the Apollo 16 site is 9.0687 degrees at noon. Using Equation 9, our fits to our laboratory soil reflectance measurements yield $A_h(9.0687°)=0.1389$. To fit the Diviner measured T_{BolC} value of 387.5K at noon using our thermal model would requires $A_h(9.0687°)=0.093$, which is approximately 33% lower than our laboratory albedo measurements would imply. Hillier et al. (1999) noted a similar discrepancy between Clementine UV/Vis Camera reflectance data and laboratory measurements of the reflectance of lunar samples. We believe that this difference could be due to some combination of two factors that have been identified in previous studies.

Ohtake et al, (2010, 2013) present comparisons between laboratory measurements of Apollo 16 sample 62231 and SELENE Multiband Imager and Spectral Profiler (MI) measurements at the sample site, which show that the MI reflectances are 24% to 33% lower than the laboratory measurements at 750 nm. Ohtake et al. (2010) ascribe 60% of this difference to potential differences in soil composition and maturity states, and 40% to potential differences in porosity and density. Also shown by Hapke (2008) and Shepard and Helfenstein (2011), increasing the filling factor (decreasing the porosity) of low to medium albedo powders increases their albedos. It is likely that the sample handling and preparation histories of our samples resulted in decreased porosities, and thus increased reflectivities. The Hapke (2008) results show that the brightening effects of decreasing porosity are greatest for medium albedo powders, which could help explain the differences in our fits between the brighter Apollo 16 soils vs the darker Apollo 11 soils. Also, given that the Apollo 16 soil samples were acquired to depths of 2-5 cm, the maturity levels of the samples are likely lower than those of the uppermost lunar surface. We also note that the Apollo 16 field site, which included several bright recent impact craters and associated ejecta, was considerably more diverse than Apollo 11. Figures 2.16 and 2.17 show Diviner Channel 1 Lambert Albedo maps of the 60 km lat/long boxes centered on the Apollo 11 and Apollo 16 sampling sites. The mean and standard deviations of the measured Lambert Albedos for the Apollo 11 box were 0.094±0.079, and 0.1670±0.15 for the Apollo 16 box. For comparison, the measured Diviner Lambert albedos for 300 meter latitude/longitude boxes centered on the Apollo 11 and Apollo 16 sample sites were 0.091 and 0.193 respectively. Although the Diviner footprint is not small enough to resolve the exact location of the Apollo 16 sample, available observations suggest that the general region sampled was 15.5% brighter than the broader field area as a whole.

2.8 Summary and Conclusions

The principal conclusions of this study are as follows:

1. We obtained a complete set of calibrated BRDF measurements of 6 lunar samples acquired at two Apollo landing sites at 450, 550, 750 and 950 at incidence angles ranging from 0 to 75°.
2. We then successfully fit the BRDF measurements to the Hapke (1993) BRDF model as well as a simplified BRDF model that we developed for this study.
3. We used the BRDF models to calculate the solar-spectrum averaged hemispheric reflectance as a function of solar incidence angle, which differ from those used in previous studies.

4. We tested the accuracy of our derived solar spectrum hemispheric reflectances by using them in a lunar thermal model to calculate normal bolometric infrared diurnal emission curves at the Apollo 11 and Apollo 16 sites.
5. We compared our model-calculated normal bolometric infrared emission curves with those measured by the LRO Diviner instrument and found excellent agreement at Apollo 11, but at Apollo 16, we found that the albedos we measured in the laboratory were higher than those required to fit the Diviner infrared data
6. We ascribe the difference at Apollo 16 to increased compaction and decreased maturity of the laboratory sample relative to the natural lunar surface, and to local variability in surface albedos at the Apollo 16 field area that are below the spatial resolution of Diviner.

2.9 Acknowledgements

We would like to thank CAPTEM, Carl Allen and Dick Morris for generously loaning the Apollo lunar soil samples to us for this study and for their expertise on lunar soil samples. We'd also like to thank NASA Diviner LRO for funding this research. We'd also like to thank Tristram Warren and an anonymous reviewer for their detailed and insightful comments.

CHAPTER 3

The BRDF of Apollo Lunar Mare Soil Samples

3.0 Introduction

As presented in Chapter 2 on the bolometric hemispheric reflectance of soils from the Apollo 11 and 16 missions, a key input for lunar thermal models is the determination of the radiative equilibrium temperature of the lunar surface. A thorough understanding of the bolometric albedo determines the radiative equilibrium temperature of the lunar surface. As was illuminated in chapter two, we found excellent agreement between the Apollo 11 orbital and laboratory datasets, however we found a discrepancy in the Apollo 16 measurements. A primary focus of this chapter is to further investigate more lunar mare samples to see if we can get the same results as we got in chapter two for the Apollo 11 mare soil sample.

Although we cannot fully measure the bolometric hemispheric reflectance from orbit, as demonstrated by Birkeback and Cremers (1970) in their measurements of soil samples brought back by Apollo 11, we are capable of accurately measuring this reflectance in the laboratory when integrating spectrophotometers are utilized. Their work has been a cornerstone of subsequent studies of thermal models. A primary goal for the subject study is to develop a more complete understanding of Bidirectional Reflectance Distribution Functions (BRDF's) for specific samples of lunar maria. This study sets forth the results of a different set of bi-directional reflectance measurements of mare regolith samples from three Apollo missions:

Apollo 12, 15 and 17. These Mare basalts were emplaced as fluids that flowed easily across the Moon's surface. (Lunar Source Book) Basalts are dark-colored rocks solidified from molten lava.

We used BRDF models, both theoretical and empirical, to compare to the laboratory data and calculated the bolometric hemispheric reflectance. We subsequently used this data in conjunction with a one-dimensional thermal model to determine the bolometric infrared emission at the respective Apollo landing sites, and compared diurnal bolometric thermal emission measurements made by DIVINER (Paige et al., 2010a) with our results.

3.1 Samples

The Curation and Analysis Team for Extraterrestrial Materials (CAPTEM) at NASA provided three lunar mare basalt soil samples: a low albedo mare sample (12001, Apollo 12), a moderately low albedo mare sample (15071, Apollo 15) and a very low albedo mare sample (70181, Apollo 17). These mare basalts were emplaced as fluids that flowed easily across the Moon's surface and solidified into dark colored rocks called Basalts. The first lunar samples that were understood through earth's magmatic processes came from the Apollo 12 mission. (Rhodes et al, 1977) In total, the Apollo 12 crew returned over 32 kg of lunar samples. These samples enabled scientists to determine that the Copernicus crater impact occurred some 810 million years ago; four different types of local basalts were sampled with ages much younger than those from Apollo 11, and a small sample of highlands rock previewed the complexity of the lunar highlands to be sampled on later Apollo missions. Figure 3.1 shows an astronaut collecting samples from the lunar surface during the Apollo 12 mission. Figure 3.2 shows an LROC image of the Apollo 12 landing site. All in all the Apollo 12 mission was an incredible success, and it paved the way for the science missions yet to come. The Apollo 15 mission was the first to use a lunar rover vehicle and hence was able to cover more of the lunar surface surrounding the lunar module than had previous missions. Figure 3.3 shows the tracks of the rover on the surface of the moon during the Apollo 15 mission. The astronauts covered significantly more ground during the latter missions (Apollo 16 and 17) due to the addition of the lunar rover vehicle. The tracks left on the surface 50 years ago are still noticeable as you can see in the pictures taken from the Lunar Reconnaissance Camera on the LRO spacecraft. Figures 3.2 through 3.4 are LROC images of the Apollo 12, 15 and 17 sites.

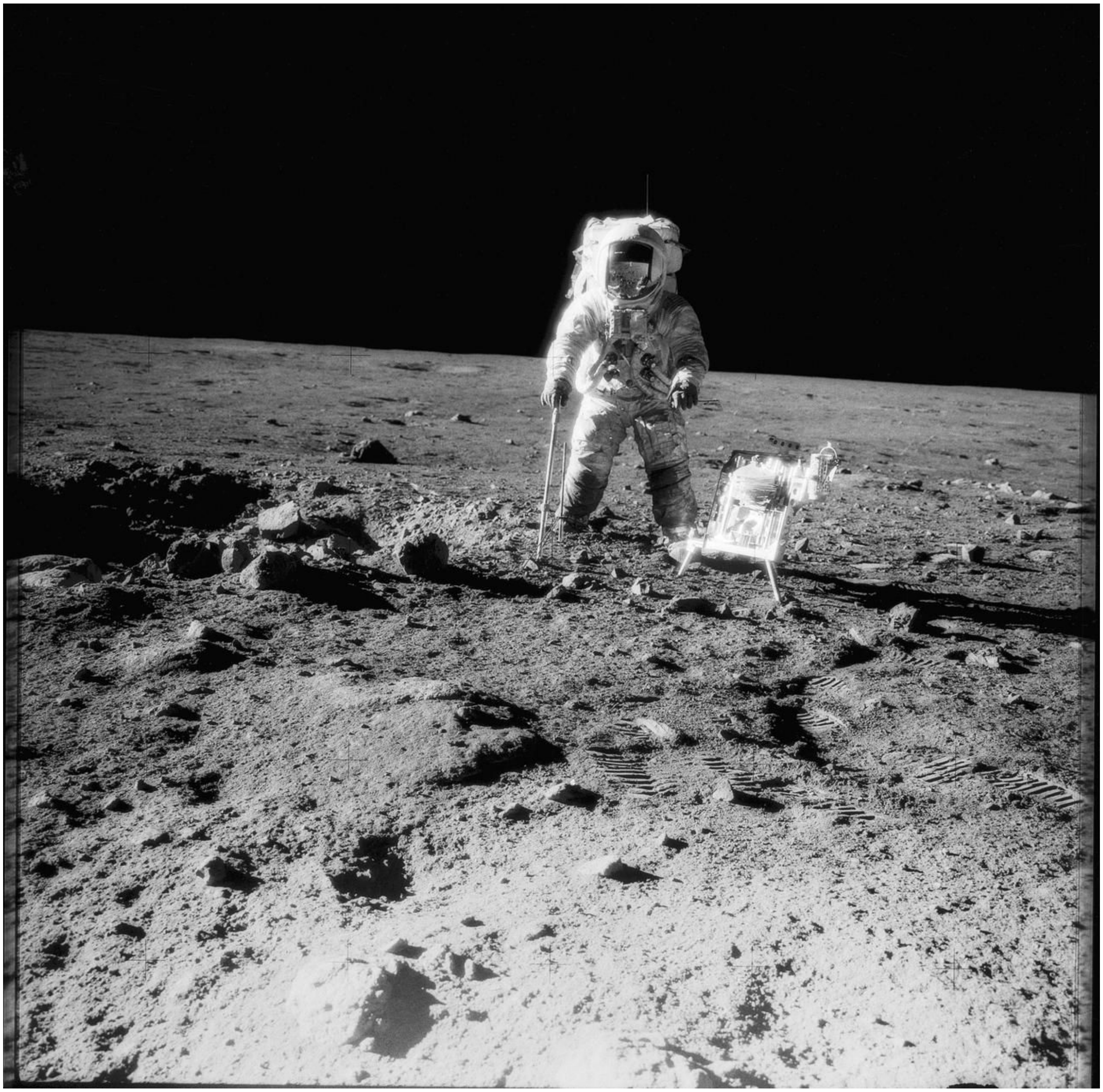

Figure 3.1: (NASA archive image) Apollo 12 astronaut is pictured here collecting samples with the Apollo Lunar Hand Tools (ALHT) kit. Also worth noting are the footprints made by the Apollo 12 astronauts Charles Conrad Jr. and Alan L. Bean on the fine grained fluffy lunar surface.

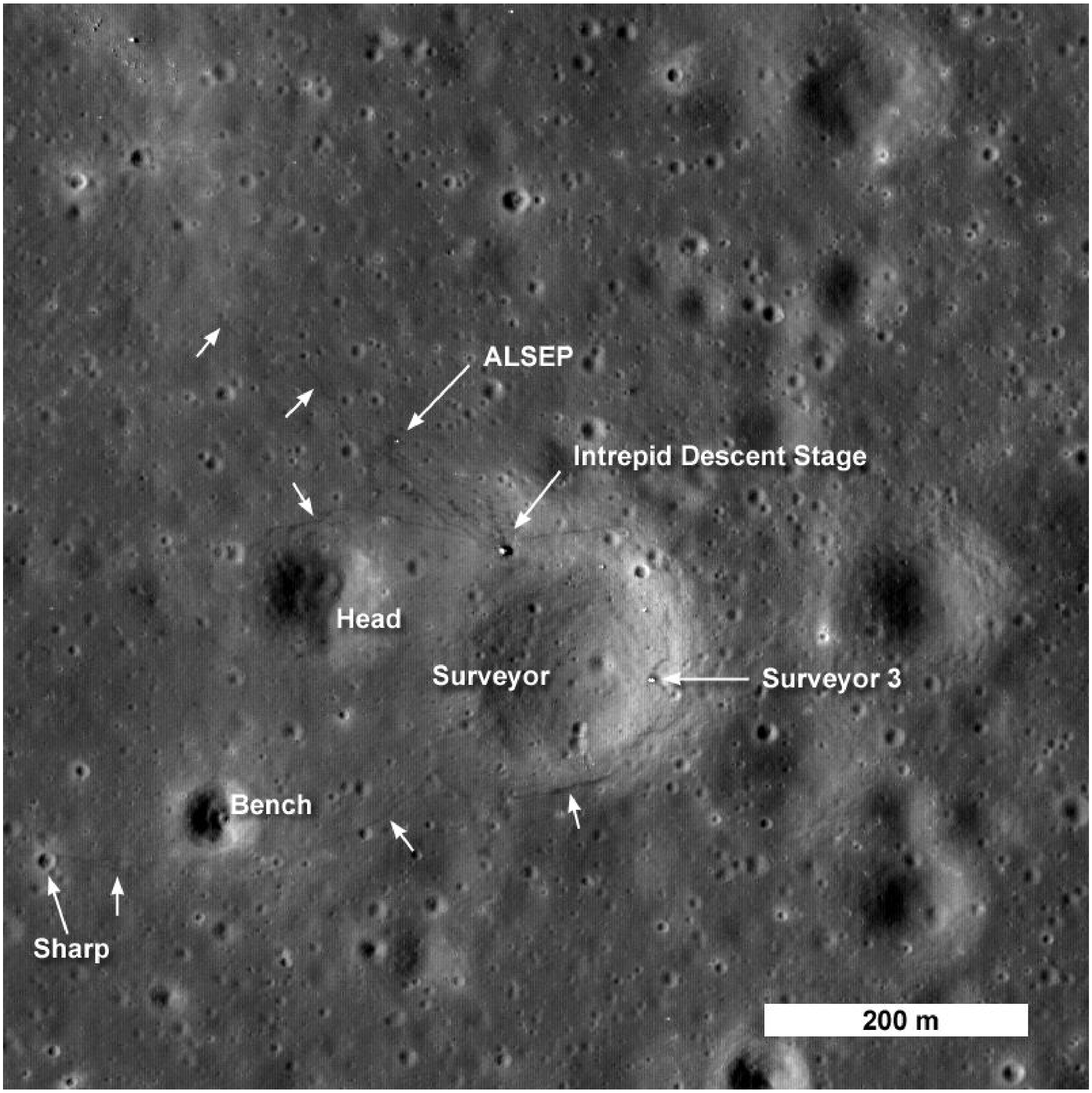

Figure 3.2: This is an LROC image of the Apollo 12 landing site. Also shown is the Lunar Module descent stage, the Experiment package (ALSEP) and Surveyor 3 spacecraft. The labeled arrows indicate the location of each object and the unmarked arrows show the tracks made by the Apollo astronauts. The scale is shown on the bottom right.

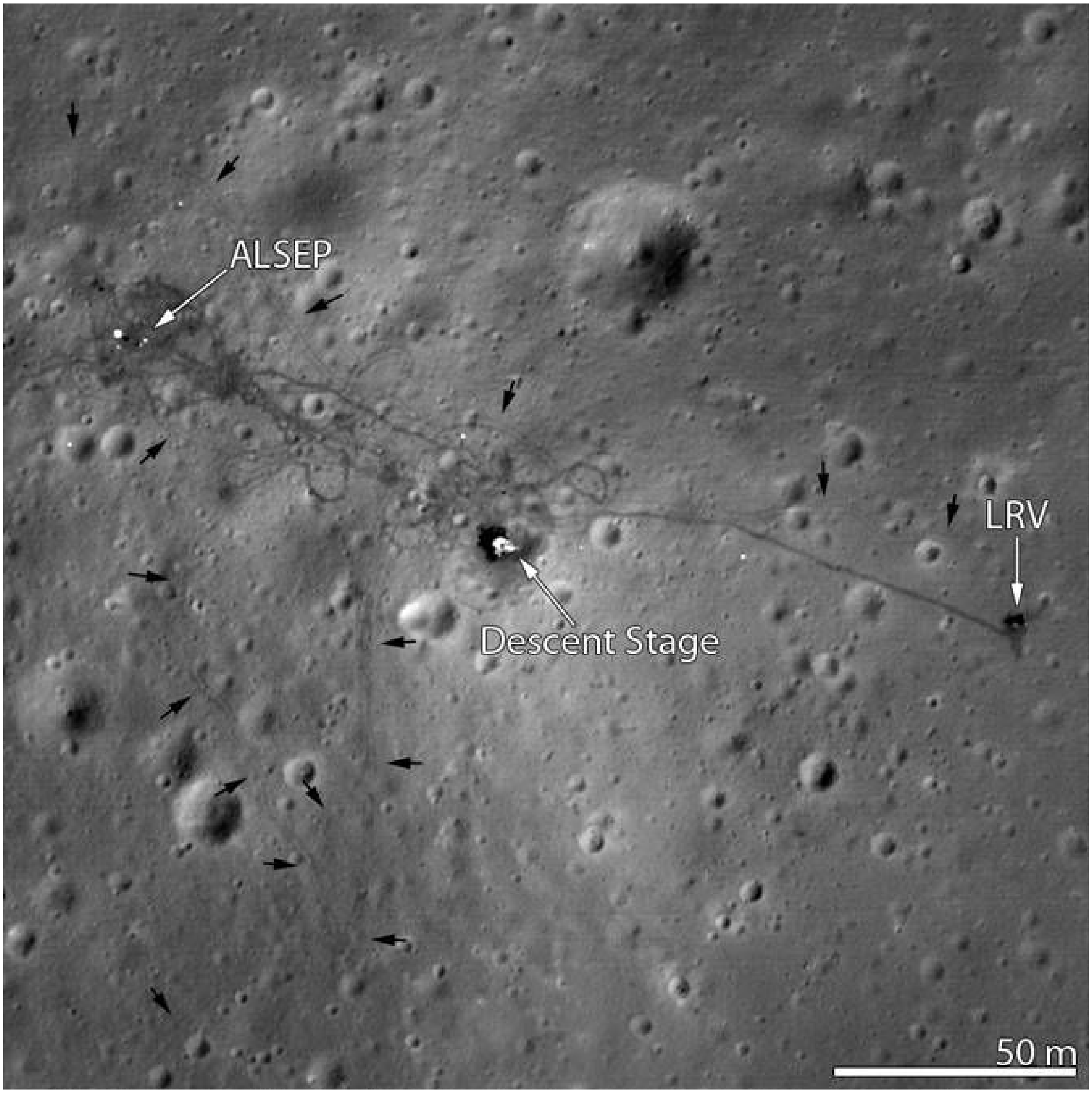

Figure 3.3: LROC image of the Apollo 15 landing site. The tracks in the picture are from the lunar module vehicle roaming the surface. Apollo 15 was the first mission to use the Lunar Roving Vehicle. The labeled arrows indicate the other anthropogenic features from the Apollo 15 mission. The scale bar is on the bottom right of the image.

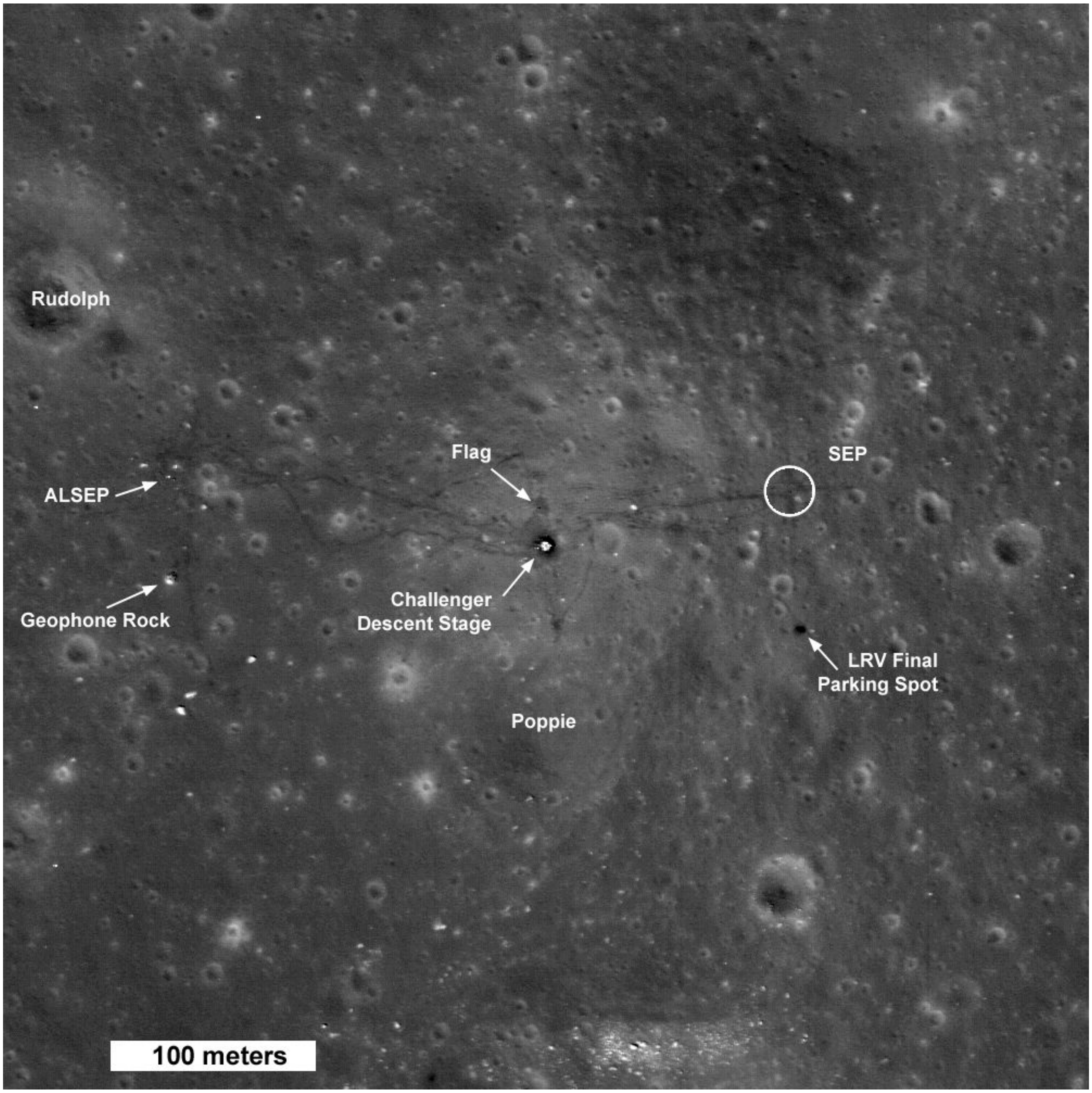

Figure 3.4: LROC image of the entire Apollo 17 site. The scale bar is on the bottom left of the image.

For this study, CAPTEM generously loaned us 20 grams of the Apollo 12 lunar soil sample 12001, 20 grams of the Apollo 15 lunar soil sample 15071 and 20 grams of the Apollo 17 lunar soil sample 70181. The Apollo 12 sample is a submature medium gray with brownish hue soil that was collected near the Lunar Module during the astronauts traverse between the Surveyor and Crescent Craters. The Apollo sample 15071 is part of a radial surface sample, collected 25 meters east of the crater rim of Elbow Crater. It is a submature sample with 39.5% monomineralic components that include 23.7% pyroxene, 9.3% plagioclase and 4.2% olivine. The Apollo sample 70181 is a submature surface sample (it was collected 0 to 5 cm depth) that was located near the Apollo Lunar Surface Experiments Package (ALSEP), 3 m from deep drill core. It has 56% Agglutinates with 14% basaltic components and 4.6% low-grade-brown breccias. (Handbook of Lunar Soils, 1993) Figure 3.5 shows three close up images of each of our lunar mare soil samples used in this study. Detailed descriptions of each of our samples can be found in Table 1, which includes petrography, grain size, maturity and major elements. For our purposes, maturity is defined as the degree of surface exposure to micrometeorites and solar wind which particular soil has experienced. The specific information was derived from the Lunar Soil Handbook (Handbook of Lunar Soils, 1993) Table 3.1 also shows our measurements of the bulk density of our two lunar soil samples, which was accomplished by measuring the weights of the samples in a 2.5 ml volume, just like we did for the Apollo 11 and 16 soil samples discussed in chapter 2.

Table 3.1: Descriptions of Apollo samples used in this study from The Handbook of Lunar Soils (Handbook of Lunar Soils, 1983) The bulk density of each sample was measured in our laboratory at UCLA. Note: average grain size

Sample Name	Grain Size	Maturity	Petrography	Color	Major Elements	Bulk Density
Apollo 12001	60μm	submature (I/FeO -56.0 and agglutinates)	12.9% mare basalt, 40.1% agglutinates, 18.3% mafic mineral fragments, 5% devitrified glass	medium gray with brownish hue	46% SiO2, 2.8% TiO2, 12.5% Al2O3, 17.2% FeO, 10.4% MgO, 10.9% CaO	1.32
Apollo 15071	100μm	submature (I/FeO -52.0 and agglutinates)	9.3% Plagioclase, 23.7% Pyroxene, 34.6% agglutinates, 10.9% Crystaline lithics, 6.1% glass, 8.9% breccias	light gray	46.95% SiO2, 12.7% Al2O3, 1.6% TiO, 16.29% FeO, 10.75% MgO, 10.49% CaO	1.262
Apollo 70181	58μm	submature (I/FeO -47.0 and agglutinates)	4.3% plagioclase, 10.3% clinopyroxene, 56% agglutinates, 7.2% breccias, 4.4% glass	dark olive gray	40. 87% SiO2, 12.3% Al2O3, 8.11% TiO, 16.37% FeO, 9.82% MgO, 11.05% CaO	1.273

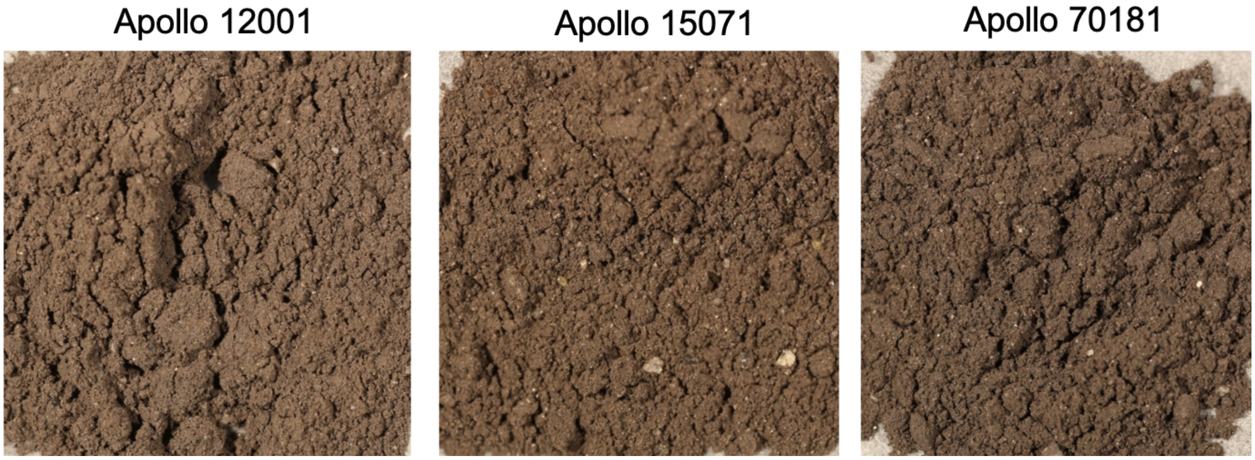

Figure 3.5: Close up images of Apollo 12, 15 and 17 soil samples. The width of each closeup sample image is 1cm.

3.2 BUG set up and Dataset

We used Bloomsburg University Goniometer (BUG) to make the BRDF measurements on this suite of Apollo lunar mare samples. We used the same configuration of angles as we did for the Apollo 11 and 16 samples discussed in chapter 2. As we stated previously, BUG measures the radiance factor r_f, which is the ratio between the measured intensity to that of a normally illuminated perfectly reflecting diffuse (Lambert) surface. Since r_f varies with illumination geometry, the bidirectional reflectance is most easily visualized in terms of the Lambert albedo, which is the ratio of the measured reflectance relative to that of a Lambert surface measured under the same illumination condition (Hapke, 1993; Shepard, 2017). For this work, we define Lambert albedo as:

$$A_L = r_f/\mu_0 \tag{1}$$

Where μ_0 is the cosine of the incidence angle. A Lambert surface has a constant Lambert albedo at all illumination and viewing geometries, and therefore represents the simplest surface BRDF model.

We present the BUG reflectance data in terms of the Lambert Albedo. Figure 3.6 shows representative plots of the measured BUG Lambert albedos for the Apollo 12, 15 and 17 samples at two different incidence angles, i=15° and i=60°. The results are presented in polar contour plots using all the data;

Apollo 12, *i*=15° and *i*=60°

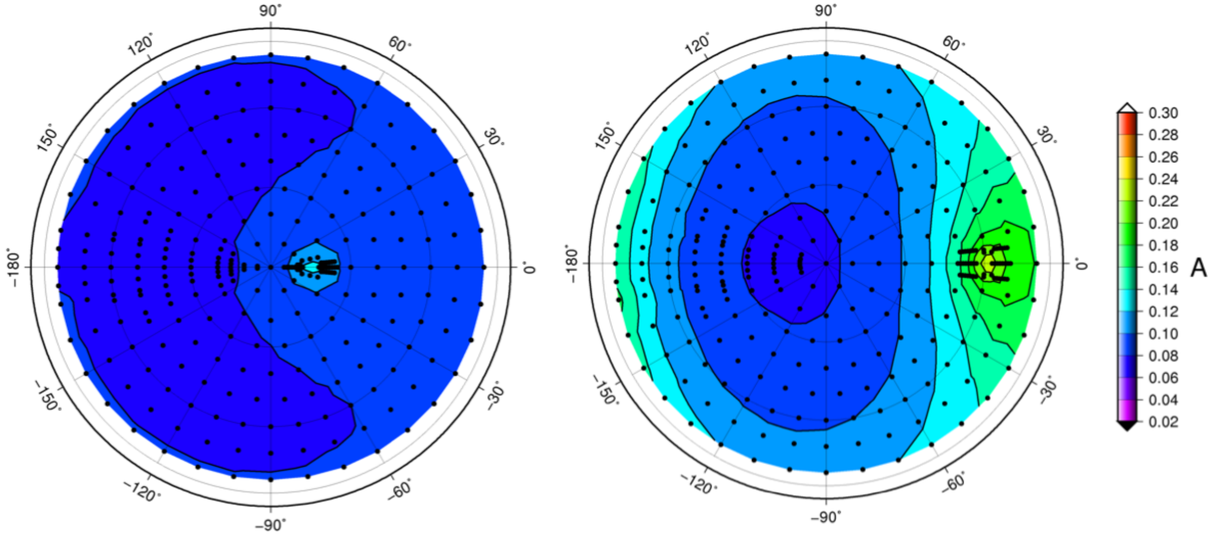

Apollo 15, *i*=15° and *i*=60°

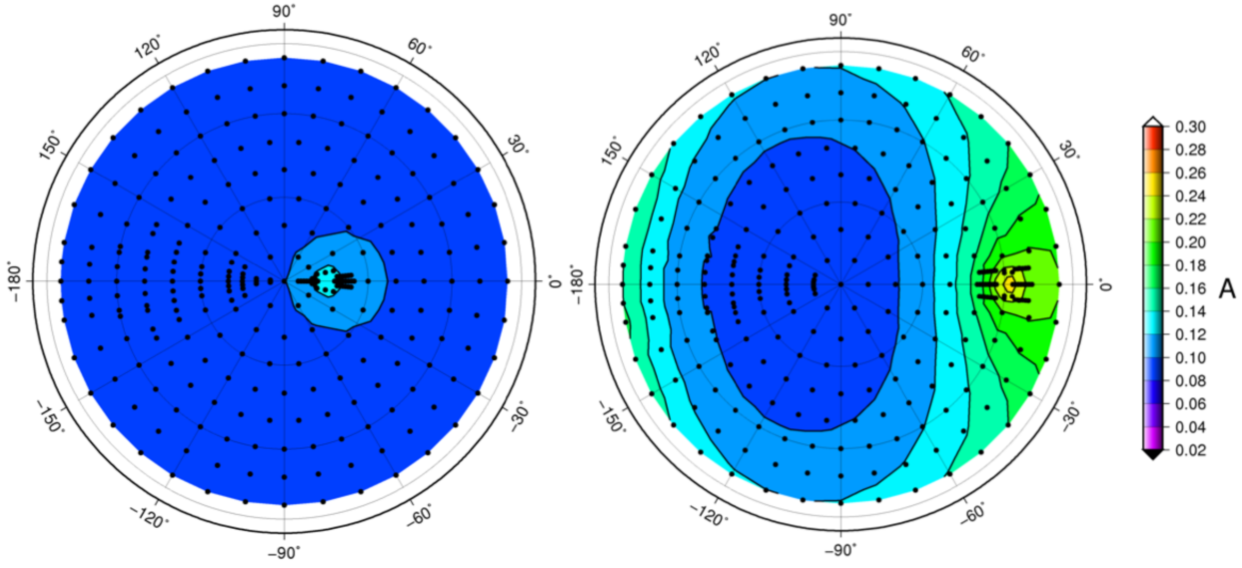

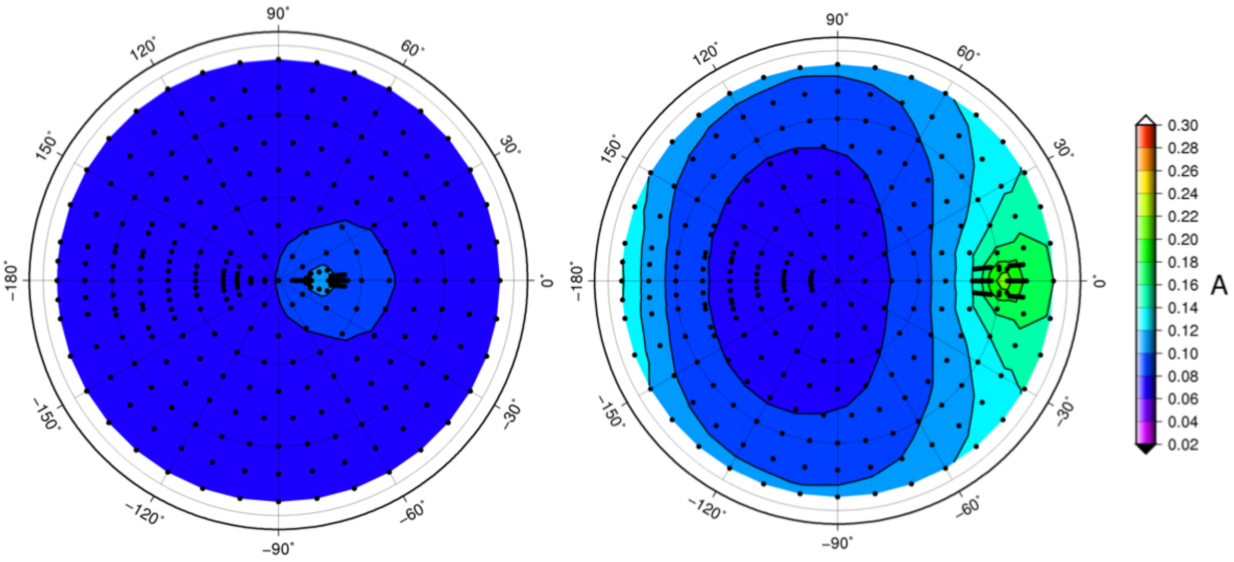
Apollo 17, *i*=15° and *i*=60°

Figure 3.6 Polar contour plots of measured Lambert Albedo where e is the radial coordinate and ψ is the azimuthal coordinate. Dots denote BUG angle sets. Shown are measurements for *i*=15°and *i*=60° for Apollo 12 (top 2 plots), Apollo 15 (middle 2 plots) and Apollo 17 (bottom 2 plots). The illumination source is along the positive X axis. The radial coordinate is emission angle (to 90°) and the azimuthal coordinate is azimuth angle, where 0° azimuth defines the plane of incidence. The principal plane is oriented along the x axis. Note: the BUG measurements were made on one side and are reflected about the principal plane in these graphs.

3.3 BRDF Models and Results

One of the main motivations for this work is to obtain a full BRDF and find a photometric model that fits the Lunar Mare for our Apollo 12, 15 and 17 BUG datasets. The model fits enable the calculation of BRDF's at any combination of photometric angles, and to determine the hemispheric bolometric reflectance. We chose to fit the BUG BRDF data to Hapke's 1993 BRDF model.

As previously discussed in chapter 2, we used Hapke's equation (12.55) (Hapke, 1993) for the bidirectional-reflectance distribution function (BRDF) of a rough surface. Hapke's models are based on a combination of radiative transfer modeling and empirical parameterizations. This version of Hapke's model was chosen because of its widespread use in the field, and because it was the least complex version that includes enough free parameters to obtain accurate fits. Hapke's 1993 BRDF equation (Equation 12.55) can be expressed in terms of the Lambert Albedo:

$$A_L = \frac{w}{4\mu_0}\frac{\mu_{0e}}{\mu_{0e}+\mu_e}\left\{\left[(1+B(g)p(g)+H(\mu_{0e})H(\mu_e)-1)\right]S(i,e,g)\right\} \qquad (2)$$

where w is the single scattering albedo, μ_{0e} and μ_e are the computed effective cosines of the incidence and emission angles accounting for surface roughness, *B(g)* is a backscattering function for the opposition effect, *p(g)* is the single scattering phase function, *H* are the Chandrasekhar (1960) "H" functions that account for multiple scattering, for which we employed Hapke's simplified equation 8.50, and *S(i,e,g)* is a shadowing/visibility function, equation 12.50 (Hapke, 1993).

Following Johnson et al. (Johnson et al, 2006), we use:

$$B(g) = B_0/(1+\frac{tan(g/2)}{h}) \qquad (3)$$

and

$$p(g) = \frac{c(1-b^2)}{(1-2b\,cos(g)+b^2)^{3/2}} + \frac{(1-c)(1-b^2)}{(1+2b\,cos(g)+b^2)^{3/2}} \qquad (4)$$

Where B_0 is the amplitude of the shadow hiding opposition surge and h is the angular width of the shadow hiding opposition surge. *p(g)* is approximated as the 2-term Henyey-Greenstein function. Where *c* represents the backward scattering fraction and *b* is the asymmetry parameter.

<u>*BRDF Results*</u> We successfully fit the BUG data with Hapke's BRDF model described above

using a fitting procedure in which we selected a range of parameter values and time step for each parameter and tried every combination until the sum of squares was minimized. As shown in Table 3.2, we obtained best fit reduced chi-squared χ^2_v values between 0.03 and 0.19 for the Apollo 12 sample and χ^2_v values between 0.03 and 0.05 for the Apollo 15 and 17 soil samples. This indicates that the data are well fit by Hapke's model. The Apollo 17 data have the lowest overall χ^2_v values and the Apollo 12 BUG data have the highest χ^2_v values. We assumed that each of the BUG measurements had the same uncertainty value and the absolute systematic error was 4% (**σ**=0.04) , based on Johnson et al., 2013. Although, according to Shepard and Helfenstein, 2007 the uncertainties in the high emission BUG data ($i=60^\circ$, $e=80^\circ$) tend to be 5-10% larger. Recognizing that Hapke's model is non unique, we utilized it because of its wide acceptance and use in the field, and because it is the least complex model with enough free parameters to obtain accurate fits to the data. The most robust parameter is the single scattering value. The average single scattering albedo (*w*) for the Mare sample Apollo 12001 is 0.305, is approximately 0.351 for sample 15071 and is 0.309 for sample 70181. All of the values for our Hapke fits are shown in table 3.09.

Table 3.2: Best fit Hapke parameters for the Apollo 12, 15 and 17 soil samples for each of the BUG filters.

Apollo Sample 12001

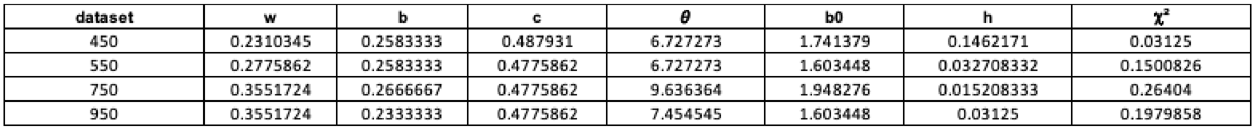

dataset	w	b	c	θ	b0	h	χ^2
450	0.2310345	0.2583333	0.487931	6.727273	1.741379	0.1462171	0.03125
550	0.2775862	0.2583333	0.4775862	6.727273	1.603448	0.032708332	0.1500826
750	0.3551724	0.2666667	0.4775862	9.636364	1.948276	0.015208333	0.26404
950	0.3551724	0.2333333	0.4775862	7.454545	1.603448	0.03125	0.1979858

Apollo Sample 15071

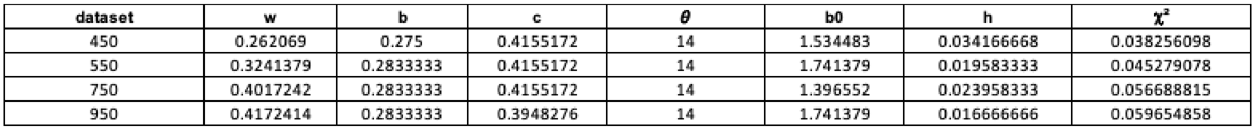

dataset	w	b	c	θ	b0	h	χ^2
450	0.262069	0.275	0.4155172	14	1.534483	0.034166668	0.038256098
550	0.3241379	0.2833333	0.4155172	14	1.741379	0.019583333	0.045279078
750	0.4017242	0.2833333	0.4155172	14	1.396552	0.023958333	0.056688815
950	0.4172414	0.2833333	0.3948276	14	1.741379	0.016666666	0.059654858

Apollo Sample 70181

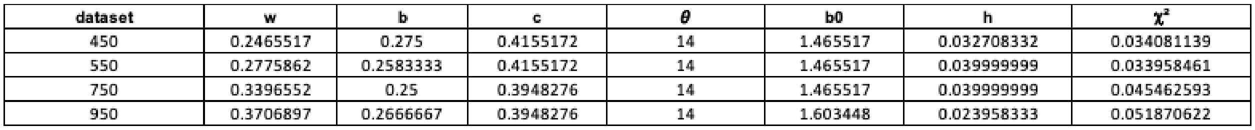

dataset	w	b	c	θ	b0	h	χ^2
450	0.2465517	0.275	0.4155172	14	1.465517	0.032708332	0.034081139
550	0.2775862	0.2583333	0.4155172	14	1.465517	0.039999999	0.033958461
750	0.3396552	0.25	0.3948276	14	1.465517	0.039999999	0.045462593
950	0.3706897	0.2666667	0.3948276	14	1.603448	0.023958333	0.051870622

Examples of BRDF model Lambert albedos are shown in Figure 3.7. The model results are presented in polar contour plots similar to the plots above of the BUG data. The results show that the Hapke model satisfactorily fits the BUG data.

Apollo 12 *i*=15° and *i*=60°

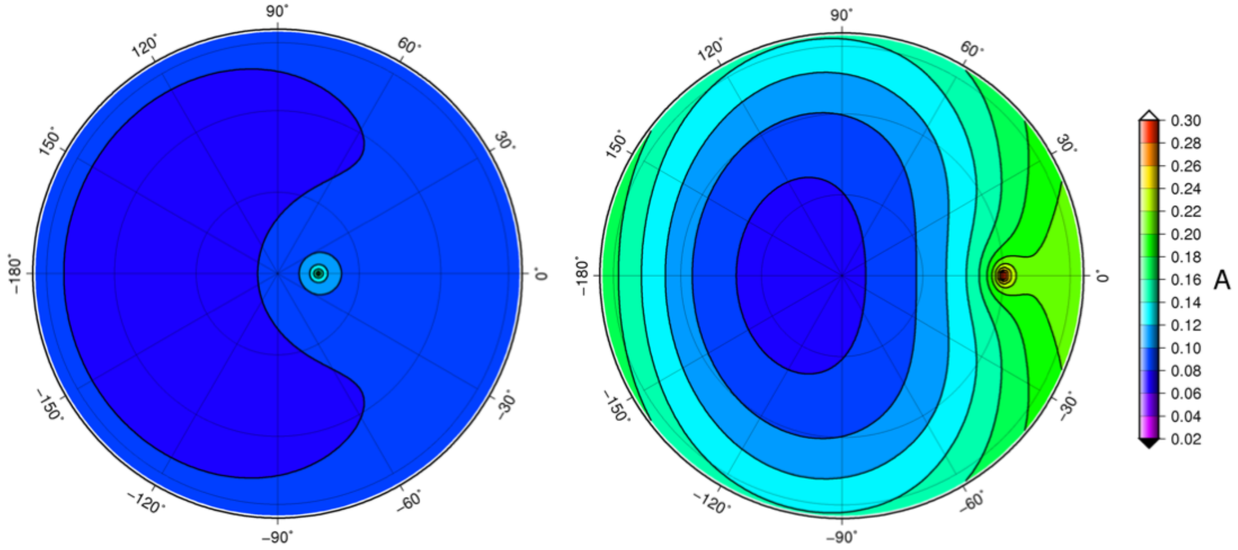

Apollo 17 *i*=15° and *i*=60°

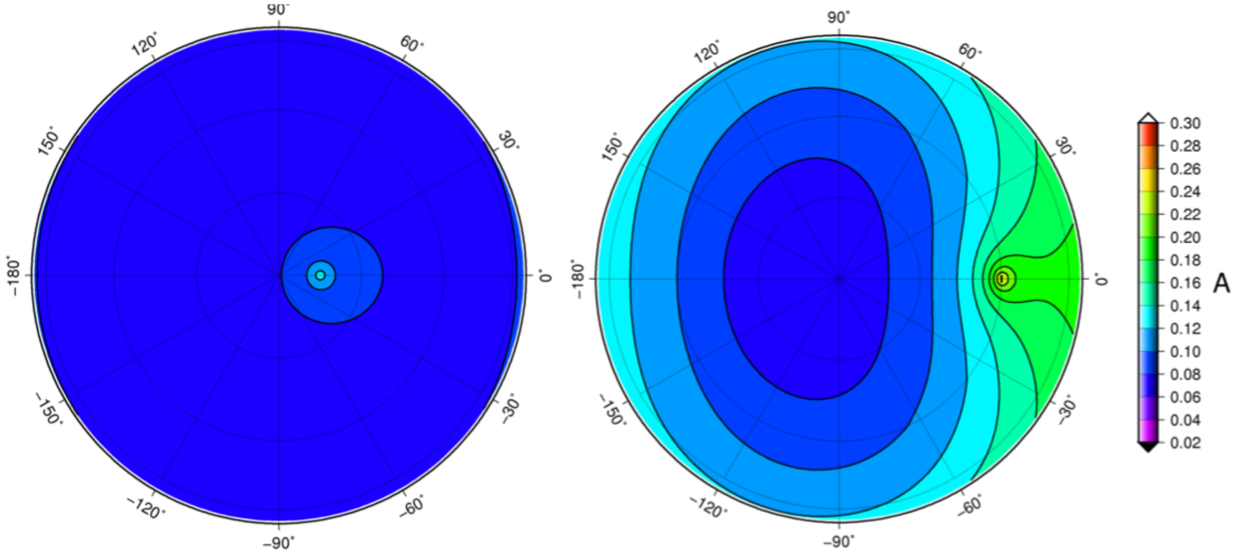

Figure 3.7. BRDF polar contour plots of the Hapke functions using the best fit parameter values shown in table 2 for *i*=15° and *i*=60° for the 750nm wavelength datasets. The colors represent Lambert albedo. The scales used here are the same as shown above for the BUG data. The top two plots were made by fitting models to the for Apollo 12 data and the bottom two plots represent models fit the Apollo 17 data.

3.4 Solar Spectrum Averaged Hemispheric Albedo Results

The heat balance of the lunar surface is controlled by the solar spectrum averaged hemispheric albedo, which is sometimes referred to as the bolometric albedo, or the directional hemispheric reflectance. We determine the directional hemispheric albedo, A_h, as a function of incidence angle, using Hapke's equation 10.10:

$$A_h(i) = \pi \int_{2\pi} A_L(i, e, g) \mu d\Omega_e \qquad (5)$$

where $d\Omega_e = \sin e \, ded\psi$ and Ψ is the azimuth angle. Since BUG acquires data at discrete wavelengths, we calculated appropriate spectral boundaries and weighting factors for each BUG filter to compute the solar spectrum averaged albedo based on the ASTM E490-00a (ASTM International, 2014) solar spectrum data as shown in Table 3.3. We used extra weighting factors in chapter 2, however this didn't improve our results so we decided to use the 4 filters that we used to acquire the BRDF with BUG. The best fit Hapke values that we used to calculate the bolometric reflectance curves are shown in Table 6.

Table 3.3: Solar spectrum integration parameters employed for the calculation of A_h.

BUG Filter (nm)	Minimum Value (nm)	Maximum Value (nm)	Weighting Factor
450	0	500	0.213743418
550	500	650	0.196260065
750	650	850	0.186406329
950	850	1,000,000	0.403590202

Table 3.4:

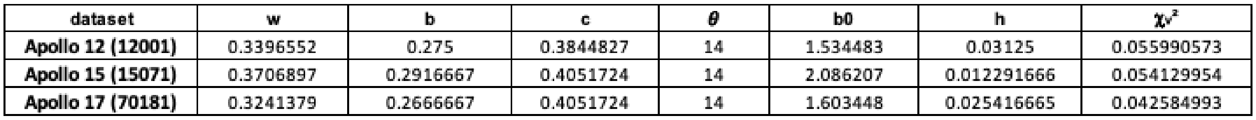

dataset	w	b	c	θ	b0	h	χ_v^2
Apollo 12 (12001)	0.3396552	0.275	0.3844827	14	1.534483	0.03125	0.055990573
Apollo 15 (15071)	0.3706897	0.2916667	0.4051724	14	2.086207	0.012291666	0.054129954
Apollo 17 (70181)	0.3241379	0.2666667	0.4051724	14	1.603448	0.025416665	0.042584993

Figure 3.8 shows the solar spectrum averaged hemispheric albedos for the Apollo 12, 15 and 17 BUG measurements as a function of incidence angle. We fit 2nd-order quadratic functions to each of the mare soil samples (Apollo sample 12001, 15071 and 70181) for $A_L(i)$ where i is in degrees. The second order polynomial fit for the mare Apollo sample 12001 is:

$$A_h(i) = 5.8804 * 10^{-6} i^2 + 3.5991 * 10^{-6} i + 0.069306 \qquad (6)$$

The second order polynomial fit for the Apollo 15 mare sample is:

$$A_h(i) = 6.3026 * 10^{-6} i^2 + 1.9943 * 10^{-6} i + 0.076127 \qquad (7)$$

The second order polynomial fit for the darkest mare Apollo sample (Apollo 17) is:

$$A_h(i) = 5.00 * 10^{-6} i^2 + 6.00 * 10^{-6} i + 0.0656 \qquad (8)$$

Also included on the same plot are Keihm's (1984) model and Vasavada's (1999 and 2012) models for the same quantity. The functional dependence of albedo on solar incidence angle previously published by Keihm and Vasavada (Keihm, 1984) and (Vasavada, 1999 & 2012) is:

$$A_h(i) = A_0 + a(i/45)^3 + b(i/90)^8 \qquad (9)$$

The parameter values that Keihm used are constrained for the entire lunar surface as $A_0=0.12$, $a = 0.03$, $b = 0.14$. Vasavada (2012) splits the lunar surface into two bolometric hemispherical reflectance functions; mare: $A_0=0.07$, $a=0.045$, $b=0.14$ and highlands: $A_0 = 0.16$, $a =0.045$, $b=0.14$.

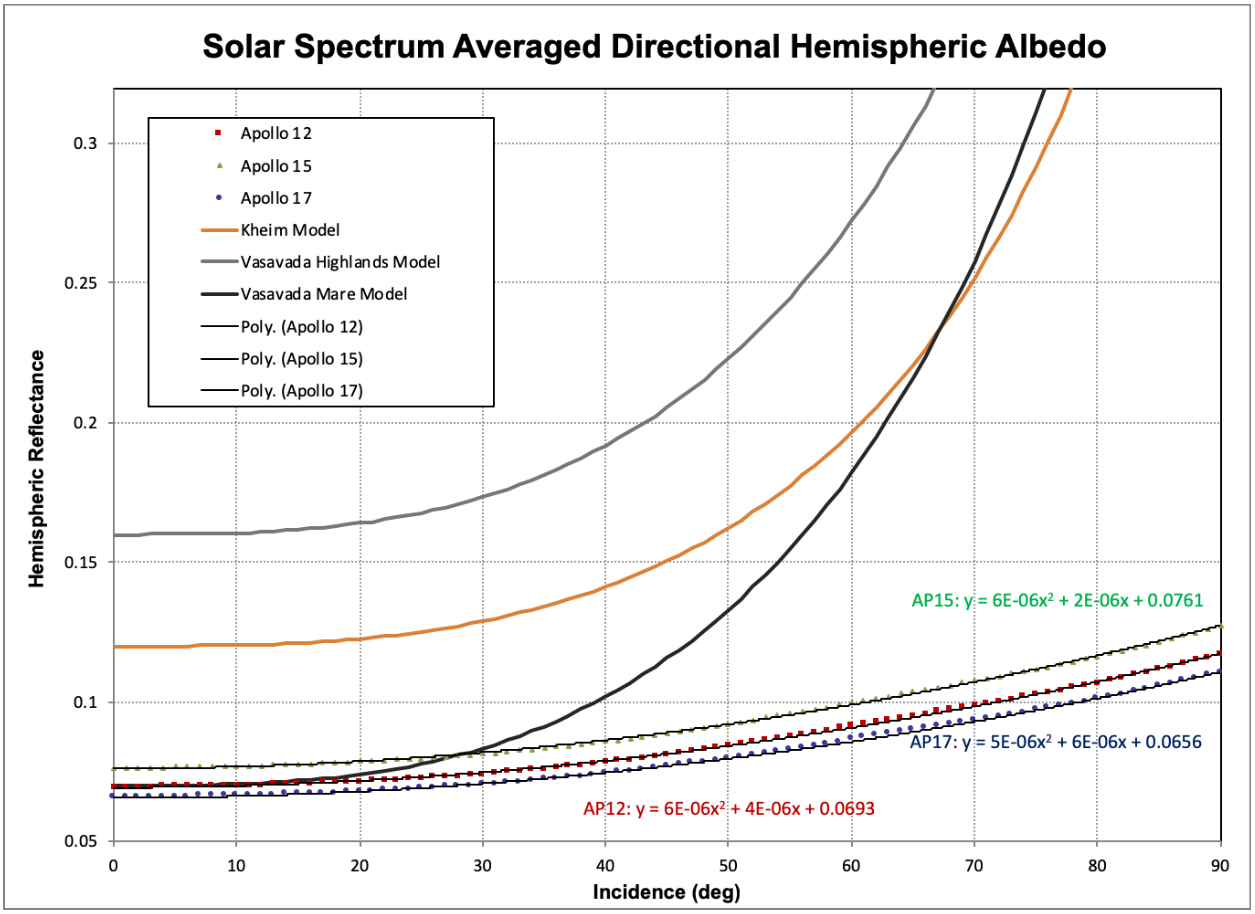

Figure 3.8: Solar spectrum averaged hemispheric albedos (A_h) as a function of solar incidence angle. Shown are our best-fits based on our BUG measurements of our Apollo samples, as well as the parameterizations used by Keihm (1994) and Vasavada (1999, 2012). Also shown are our best fit quadratic functions for A_h (i) for our Apollo 12, 15 and 17 samples.

As shown in the plot above, the hemispheric reflectance functions derived from our laboratory measurements of the Mare Apollo soil samples display relatively flat curves with increasing incidence angles, while the functions employed by Keihm and Vasavada dramatically increase beyond 50 degree incidence angle. As explained in chapter 2, Keihm's ($A_0=0.12$) and

Vasavada's ($A_0=0.07$ for the mare regions and $A_0=0.16$ for highlands) models have higher initial albedo values than what is measured at normal illumination conditions in the lab measurements of the Apollo samples ($A_0=0.069306$ for the mare Apollo 12 samples, $A_0=0.076127$ for Apollo 15 and $A_0=0.0656$ for the Apollo 17 sample). The also use a higher order polynomial, which contributes to the steep increase at higher incidence angles.

3.5 Diviner Bolometric Brightness Temperature Measurements and Thermal Model Results

We determined normal bolometric brightness temperatures from the Apollo 12, 15 and 17 sample sites using data acquired by Diviner. We employed the same method to calculate the bolometric brightness temperatures as discussed in the previous chapter.

The precise locations for the Apollo sampling stations have been determined by the LRO LROC team (http://www.lroc.asu.edu/). We found the coordinates of our sampling sites using the online Quickmap tool in conjunction with Apollo-era maps provided in the Handbook of Lunar Soils (1983). Our coordinates for the Apollo sites are shown in table 3.5. We obtained all Diviner data obtained between July 2009 and August, 2016 in Channels 3-9 with $0° < e < 5°$ within 3 km lat/lon boxes centered at these locations and binned them at a resolution of 0.25 hours in local time. We then computed bolometric brightness temperatures as described by Paige et al., (2010b). We also computed a small correction to the daytime bolometric brightness temperatures (obtained between 6 and 18 hours local time) to account for the ~7% annual variation in the solar flux due to the eccentricity of the Earth's orbit around the Sun by dividing the bolometric thermal emission by the square of of the Sun-Earth distance in AU. The seasonal effects due to the small (1.54°) obliquity of the Moon are negligible at these latitudes. The relationship between the corrected bolometric brightness temperatures, T_{BolC} and the measured T_{bol} values is:

$$\sigma T^4_{BolC} = \sigma T^4_{Bol} / R^2_{\oplus} \qquad (10)$$

Where $R_{\oplus}$ is the Sun-Earth distance in AU. The resulting measured T_{BolC} values for Apollo 12, 15 and 17 $R_{\oplus}<1$ (close) and $R_{\oplus}>1$ (far) are shown in Figures 3.9, 3.10 and 3.11.

Table 3.5. The Lunar coordinates of the Apollo landing sites. We used these latitudes and longitudes for the Diviner data for the bolometric temperature curves.

Apollo Site	**Longitude**	**Latitude**
Apollo 12	-23.421697617	-3.012505293
Apollo 15	3.597932339	26.03899956
Apollo 17	30.79599953	20.15399933

The thermal model we employed is equivalent to the model described by Hayne et al. (2017). We used it to calculate the bolometric brightness temperatures to compare with the Diviner data. The surface heat balance equation and description of the constants and variables we used to calculate the bolometric brightness temperatures can be found in chapter 2. Since we use prescribed values for $A_h(i)$ based on our Hapke fits to our laboratory reflectance measurements (Equations 6, 7 and 8), the only remaining free parameter in the model is the H-Parameter. The H-Parameter provides a means of gradually varying the thermal conductivity of the uppermost regolith layers, which is needed to determine/calculate the bolometric brightness temperatures of the lunar surface (Hayne et al., 2017). Our fitting procedure involved varying the H-Parameter to fit the Diviner nighttime bolometric brightness temperatures, but no effort was made to fit the Diviner daytime data.

Plots of our model-calculated normal bolometric brightness temperatures of the Apollo 12, 15 and 17 sites using our BUG Hapke derived albedo parameterizations are shown in Figures 3.9, 3.10 and 3.11. Also shown for comparison are normal bolometric brightness temperatures calculated using the Vasavada (1999, 2000) maria and highlands albedo parameterizations. We found that using an H-Parameter of 0.04m provided a best fit to the nighttime data in all cases. The available mid-morning and mid-afternoon Diviner observations for Apollo 12, 15 and 17 appear to be more consistent with our BUG empirical model results, which do not predict a significant rise in A_h at high incidence angles. Both the Vasavada and BUG empirical model results tend to underestimate the Diviner data during midday at distances greater than 1.0 AU for the Apollo 12 and 15 sites. Both models show good agreement with the late morning and early afternoon Diviner observations at the Apollo 17 site. However, The BUG empirical albedo model fits the Diviner bolomoteric temperatures better for data that are greater than 1.0 AU, whereas the Vasavada albedos fit the Diviner bolometric temperatures that are less than 1.0AU at the Apollo 17 site.

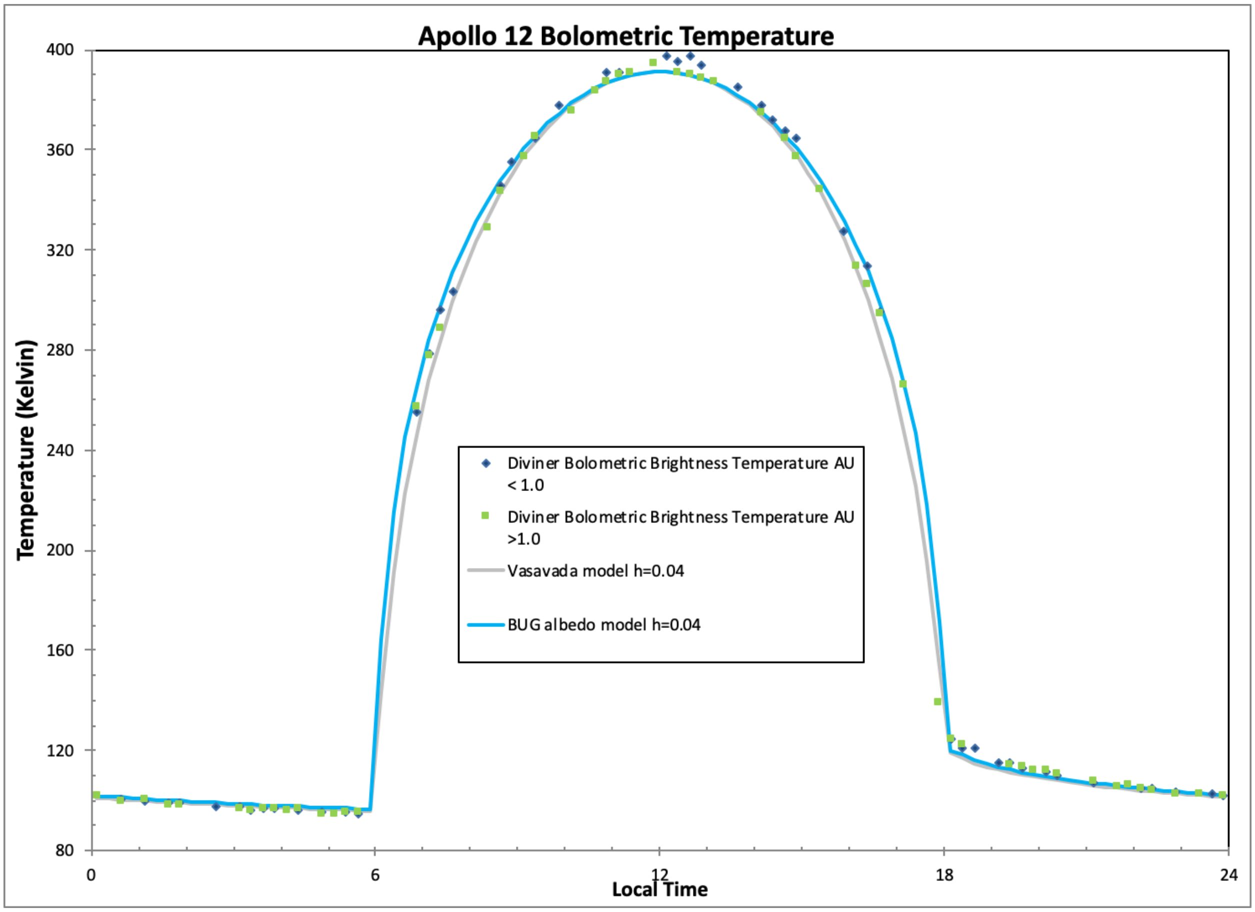

Figure 3.9: Diviner measurements of normal bolometric brightness temperatures for Apollo 12 along with the results of thermal model calculations assuming our solar spectrum averaged directional hemispheric albedo (BUG albedo model) functions for A_h (i) and those used by Vasavada et al. (2012) for Lunar Mare.

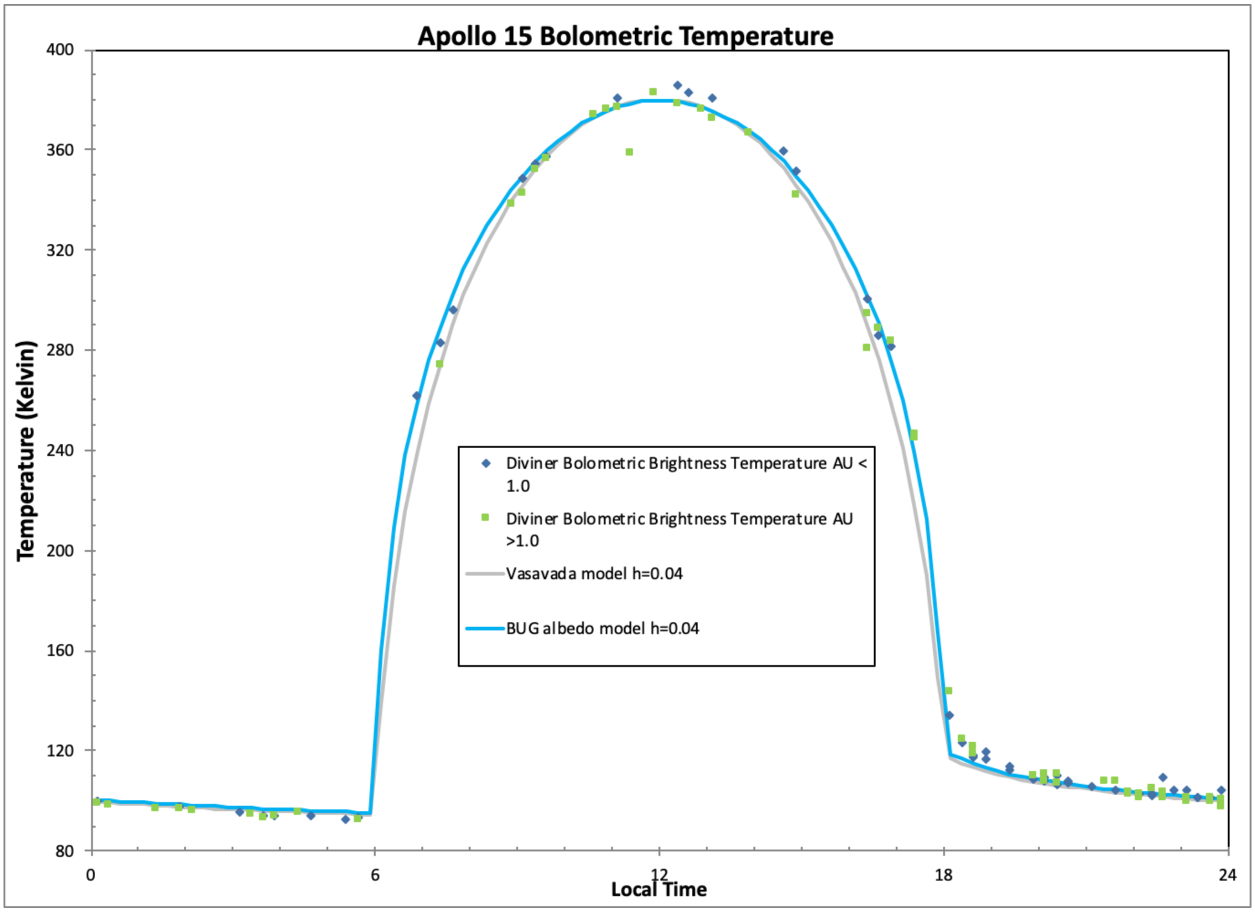

Figure 3.10: Diviner measurements of normal bolometric brightness temperatures for Apollo 15 along with the results of thermal model calculations assuming our solar spectrum averaged directional hemispheric albedo (BUG albedo model) functions for A_h (i) and those used by Vasavada et al. (2012) for Lunar Mare.

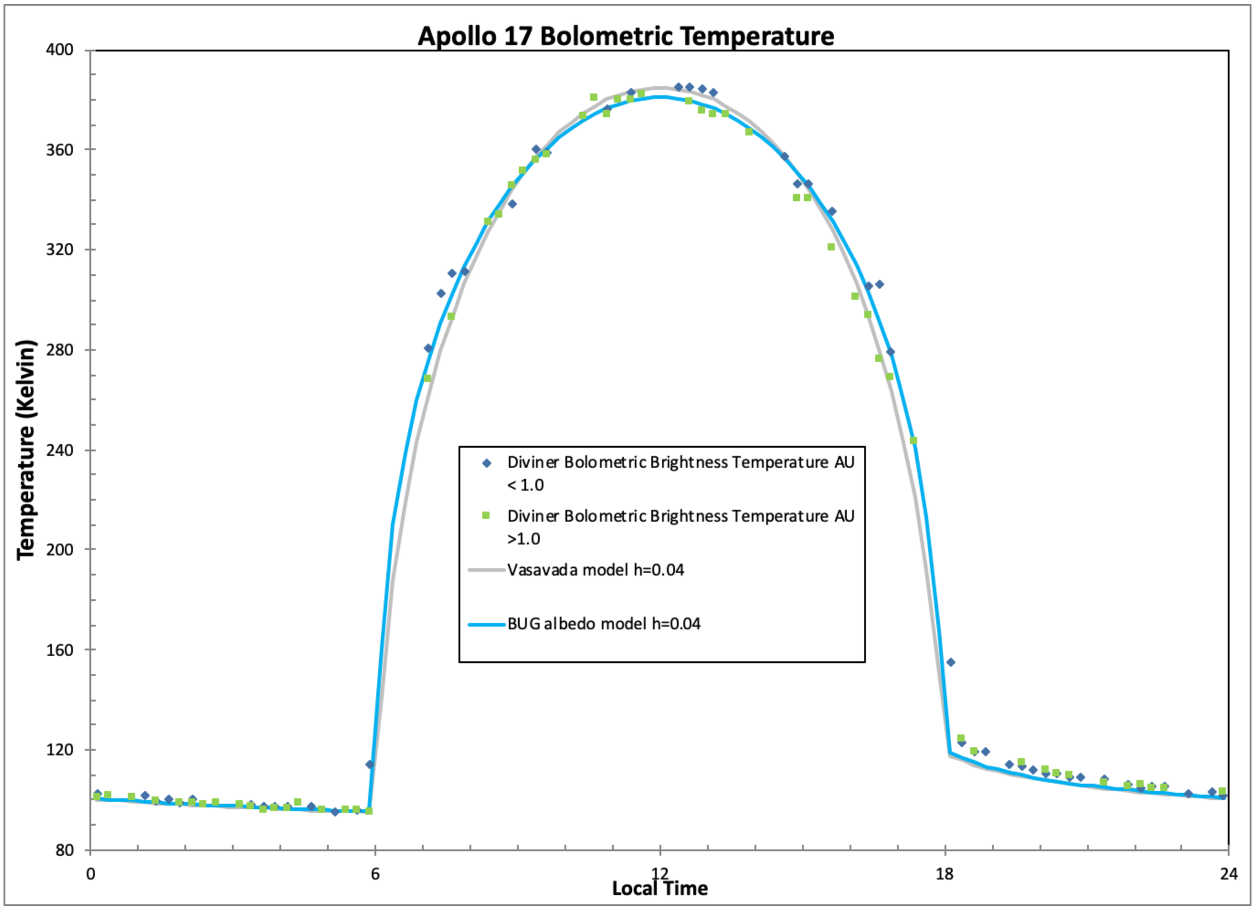

Figure 3.11: Diviner measurements of normal bolometric brightness temperatures for Apollo 17 along with the results of thermal model calculations assuming our solar spectrum averaged directional hemispheric albedo (BUG albedo model) functions for A_h (i) and those used by Vasavada et al. (2012) for Lunar Mare.

3.6 Conclusions

In total, we have obtained a complete set of calibrated BRDF measurements of three lunar samples acquired at 3 different Apollo landing sites at 450, 550, 750 and 950 at incidence angles ranging from 0 to 75°. We then successfully fit the BRDF measurements to the Hapke (1993) BRDF function as well as a simplified BRDF function that we developed for this study. We used the BRDF functions to calculate the solar-spectrum averaged hemispheric reflectance as a function of solar incidence angle, which is a key input to lunar thermal models. We tested the accuracy of our derived solar spectrum hemispheric reflectances by using them in a lunar thermal model to calculate normal bolometric infrared emission curves at the Apollo 12, 15 and 17 sites. We compared our model-calculated normal bolometric infrared emission curves with those measured by the LRO Diviner instrument and found excellent agreement at the Apollo sites.

The measurements and models we present here paint a self-consistent end-to-end picture of the solar-spectrum averaged reflectance properties for all the Apollo Mare soils. Our well-calibrated bidirectional reflectance measurements of the Apollo 12, 15 and 17 soil samples yielded solar-spectrum averaged hemispheric reflectances that produced thermal model-derived daytime bolometric brightness temperatures that are in good agreement with those measured by the well-calibrated Diviner instrument. This enhances our argument that differences in the compaction states or the surface textures of our laboratory samples versus those on the natural lunar surface were not a significant factor for the Mare Apollo sites. This is consistent with the results we found in chapter 2.

We still had a lingering question about the discrepancies in the highlands results studied in chapter 2. Ohtake's (2010) paper which ascribes the differences in their lab and orbital datasets to compaction and maturity differences inspired us to apply the same methodology to our samples. In Chapter 4 we study the effects of compaction on the albedo of our two characteristic soil samples (Apollo 11 Mare and Apollo 16 Highlands).

CHAPTER 4

The effects of densification/compaction on the albedo of Apollo 11 and 16 soils

4.0 Introduction

The work presented in Chapters 2 and 3 provides a foundation for future photometric studies of the lunar surface. In this chapter, we further investigate the discrepancy we discovered between the albedos derived from laboratory and orbital datasets for highlands soils relative to mare soils. We use the Apollo 11, sample 10084 and Apollo 16 sample 68810 to make the reflectance measurements as a function of soil porosity (packing density.) Although previous published work discusses the general effects of regolith porosity on albedo , this chapter addresses specifically how compaction affects the laboratory albedo measurements of actual lunar soil samples.

The effects of porosity of samples on the bidirectional reflectance measurements is not a new area of research. Petoniemi and Lumme (1992) first noticed that previous reflectance models did not account for the effect of packing density on scattered light in a particulate media like the lunar regolith. They showed through geometric optics and Monte Carlo simulations that dark or low albedo surfaces were noticeably brighter when the packing density was higher. Subsequently, Shkuratov et al. (1999) researched the effects of the complex particulate structures of lunar and planetary surface regoliths on measured albedos. As they demonstrated, color indices and absorption band depths for regolith-like surfaces were dependent upon particle size and upon understanding the porosity of the surfaces studied. Naranen et al (2004) also confirmed that volume density of the soils studied had a direct impact on the shadow-hiding opposition effect. However, they cautioned that variations in compaction methods will alter the material surface structure. Another study by Shepard and Helfenstein (2007) employed earlier versions of the Hapke photometric model to show that albedo, roughness, and porosity were intertwined and noted that this was due to limitations in the model because it did not account for the packing state of the particulate media. This led Hapke to update his bidirectional reflectance distribution function to include the effect of porosity (Hapke, 2008). He found that the reflectance of low and medium albedo powders increases when the porosity is decreased. Figure 1 shows this effect. He attributed this to the filling factor and the interaction between clumps of particles behaving as fundamental scatterers on the surface. In a later study by Shepard and Helfenstein (2011), it was determined that there was significant change in the surface phase function and single scattering albedo when the samples were compacted.

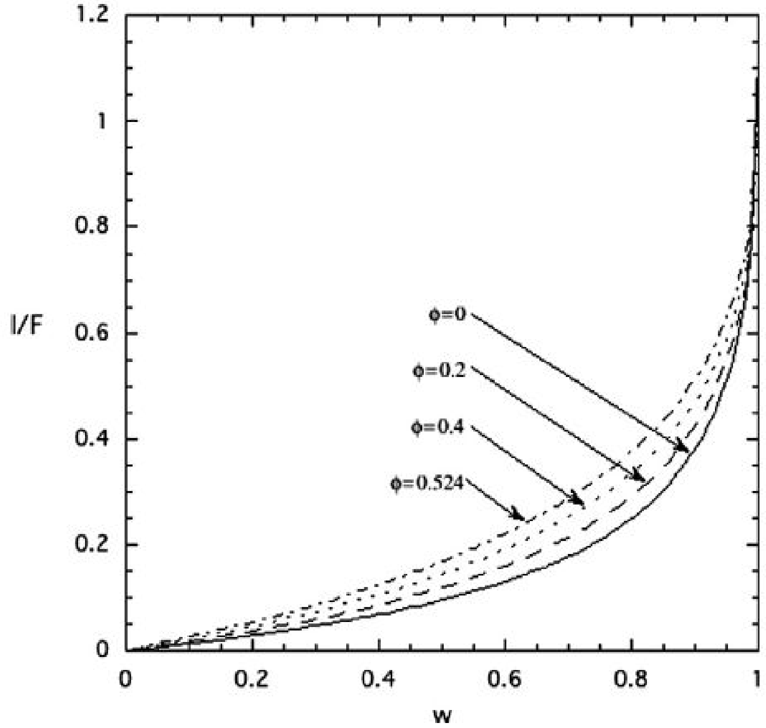

Figure 4.1: Radiance factor (I/F) versus single scattering albedo (w) at normal incidence and emission angles for several different values of the filling factor φ. The opposition effect is neglected. Note that the reflectance generally increases with φ. (Hapke, 2008)

4.1 Oxford Space Environment Goniometer and Verification

We used the newly developed Oxford Space Environment Goniometer (OSEG) to conduct albedo measurements for this study. OSEG is being developed to measure scattered light and thermal infrared emission, ranging from the visible to the far infrared (500nm to 400μm) at a range of photometric angles. The illumination source and detector are mounted on separate semicircular carriages. The sample sits on a base plate that has the capability of moving 360 degrees in azimuth space. The illumination source for the visible wavelengths is a green laser that is chopped and coupled down an optical fiber which is subsequently collimated. The source has the ability to move along a ring from 0 to 90 degrees in incidence angle and produces a one centimeter spot on the sample. The scattered light is then detected by the radiometer, which moves along a segment ring with emission angles from 0 to 180 degrees. (Warren et al., 2017, 2019). Figure two shows the OSEG experimental set up.

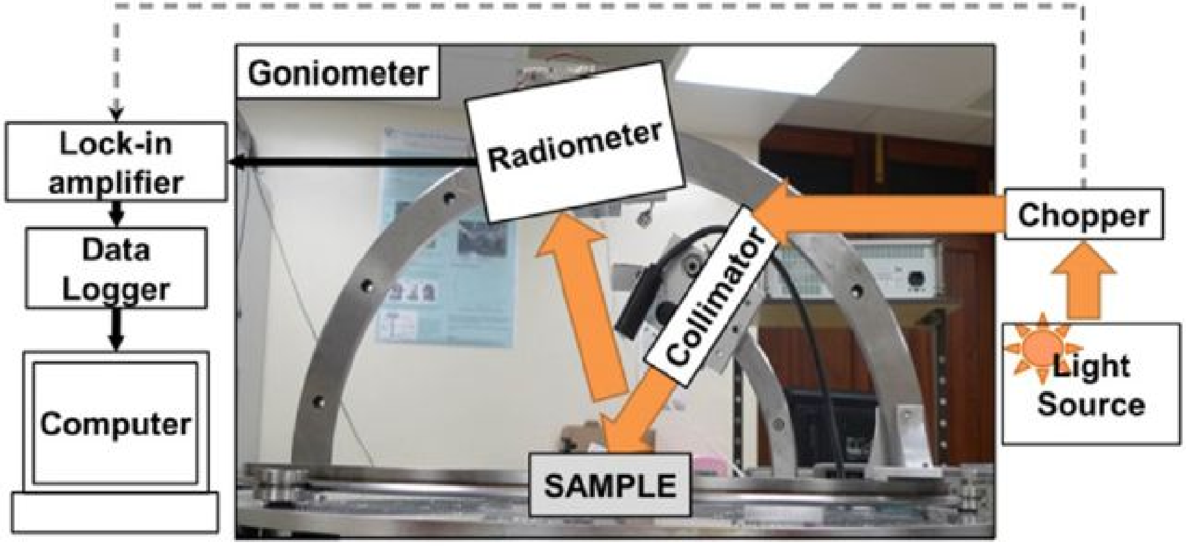

Figure 4.2: Schematic view of the Oxford Space Environment Goniometer. (Warren et al, 2017)

For the visible wavelengths, the OSEG instrument was calibrated by measuring the BRDF of a spectralon reference target, certified to NIST standards, and compared to the PHIRE goniometer. (Warren et al, 2017). The OSEG 500nm reflectance measurements were further validated by comparing the albedo of a piece of white Spectralon to those acquired with BUG's 550nm filter at the same photometric angles. Figures 3-5 show the cross calibration results of white spectralon between OSEG and BUG for fixed incidence angles of i=15, 30 and 45 degrees. All of the plots are perpendicular to the principal plane. Figure two shows excellent agreement for emission angles less than 20 degrees and then the datasets diverge slightly beyond 20 degrees. Figure 3 is a plot of fixed incidence angle of 30 degrees and shows excellent agreement between the BUG and OSEG datasets. Figure 5 shows excellent agreement between the two datasets for emission angles less than 40 degrees, however the datasets diverge dramatically beyond 40 degrees. The cause of this divergence is under investigation. The OSEG measurements are still preliminary and we have not yet resolved the discrepancies between BUG and OSEG. For this study, we are only comparing the albedos measured from OSEG to show the relative effects of packing density sample albedos at restricted photometric geometries.

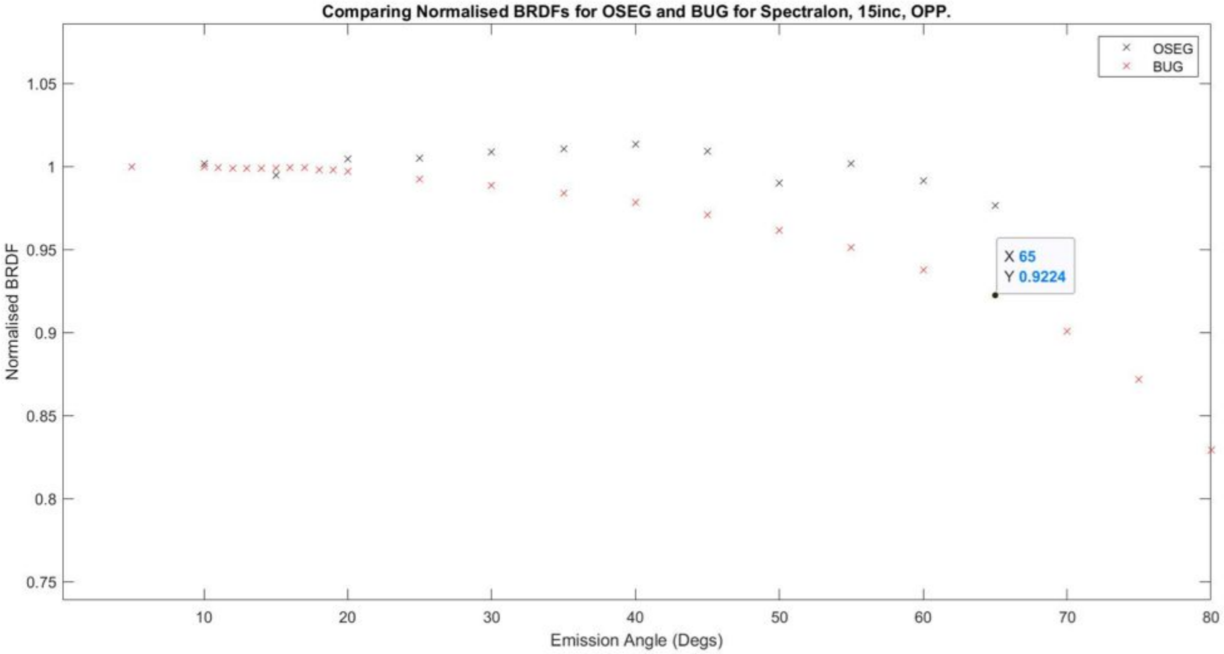

Figure 4.3: Comparisons between OSEG and BUG measurements for white Spectralon, perpendicular to the principal plane at incidence angle 15 degrees. BUG data are indicated in red stars and OSEG data are indicated in blue stars. There is excellent agreement for emission angles less than 20 degrees and slightly diverge beyond 20 degrees.

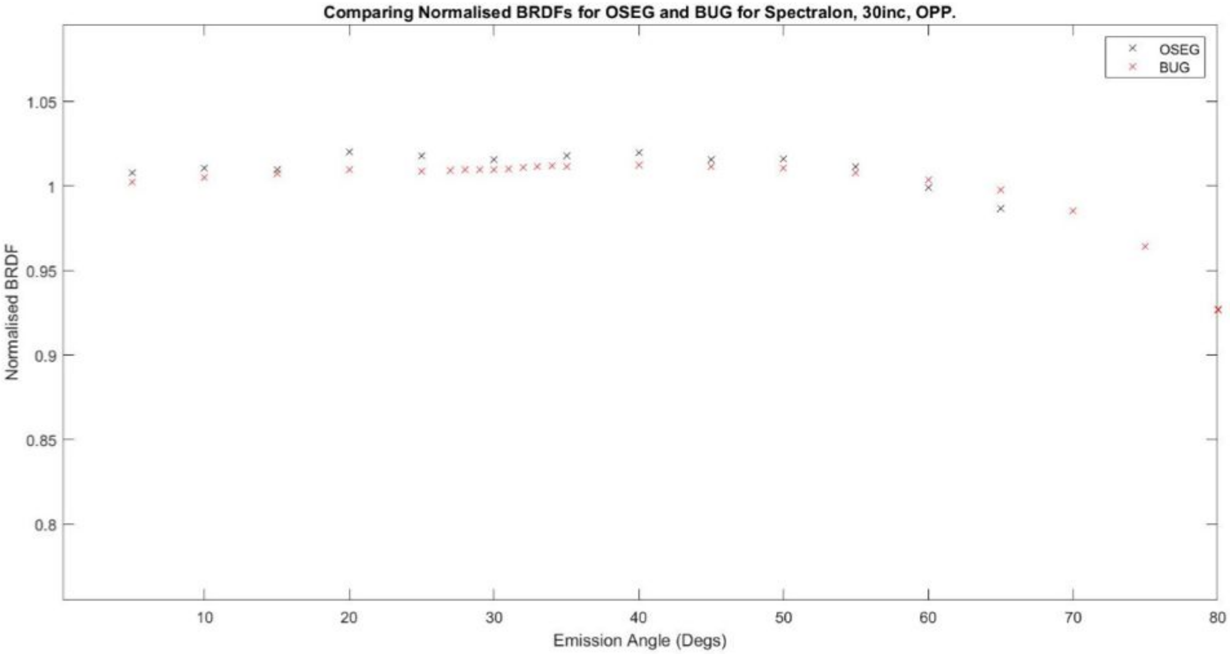

Figure 4.4: Comparison between OSEG and BUG measurements of white Spectralon, perpendicular to the principal plane at incidence angle 30 degrees. BUG data are indicated with red stars and OSEG data are indicated with blue stars. There is excellent agreement between the two datasets for this photometric range.

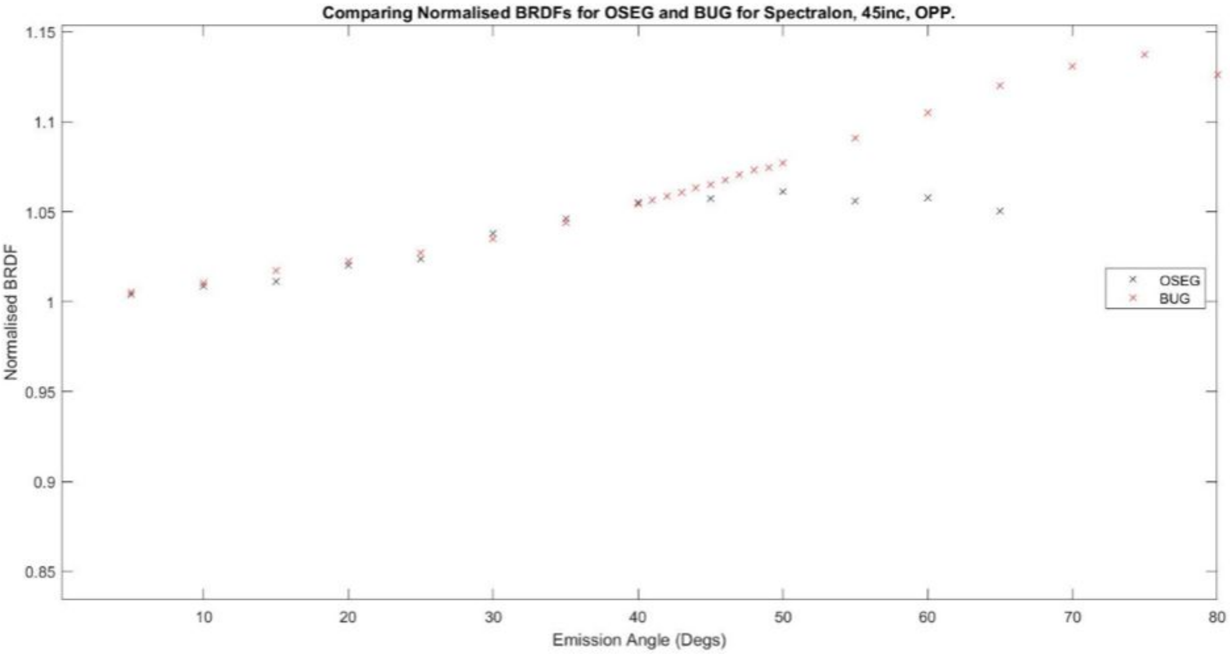

Figure 4.5: OSEG and BUG comparisons of white spectralon, perpendicular to the principal plane at incidence angle 45 degrees. BUG data are indicated with red stars and OSEG data are indicated with blue stars. There is excellent agreement between the two datasets for emission angles less than 40 degrees, however the datasets diverge dramatically beyond 40 degrees.

4.2 Sample Preparation and Density Measurements

The Apollo 11 (sample 10084) and Apollo 16 (sample 68810) soil samples were prepared in three stages to achieve three different densities (“uncompacted”, “partially compacted”, and “fully compacted”). The first round of preparation included gently pouring the uncompacted soil samples (separately) into the sample cup holder, which is 50mm in diameter. The density was calculated by weighing the sample and measuring the height of the sample with a laser profiler. The second round of measurements entailed tapping the previous sample a few times to achieve partial compaction and then measuring the height with the laser profiler. The final round measurements were made on samples that were tapped a few more times until the change in compaction remained visibly constant to achieve full compaction. Again the height was measured and the density calculated from the original weight of the sample. Figure 4.6 shows microscopic images of a similarly prepared Apollo 16 sample for each density/albedo measurement (uncompacted, partially compacted and fully compacted). The values for the densities and filling factor for each reflectance measurement made on both Apollo samples are shown in Table 4.1.

To calculate the filling factor, ϕ, we follow the method Hapke and Sato (2016) where they define the filling factor ϕ as the measured bulk density of the lunar soil divided by the solid density of an average lunar soil particle of 3100 kg/m3 (determined by Duke et al, 1970). The porosity (P) is defined as P = 1- ϕ. (Hapke and Sato, 2016)

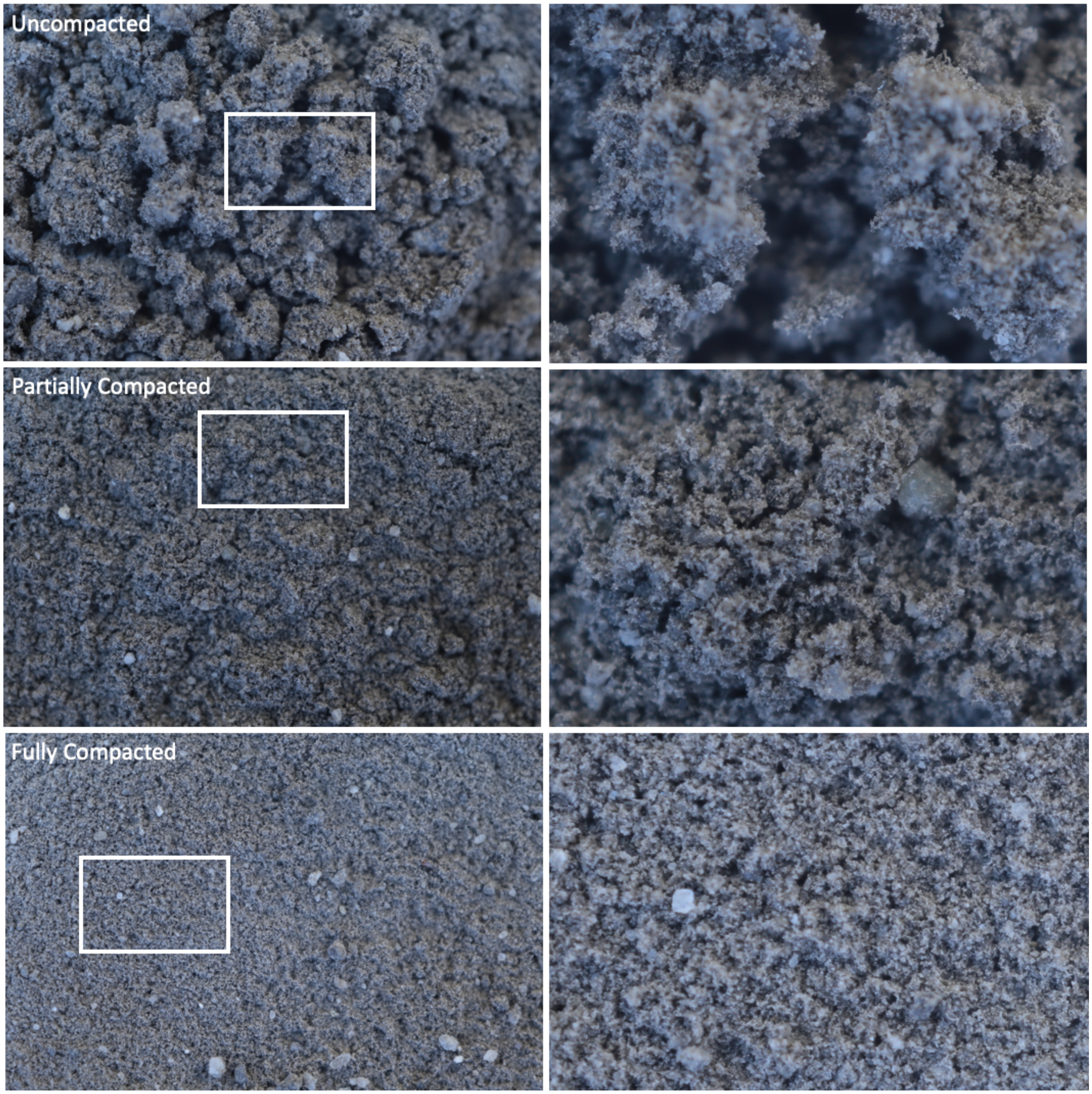

Figure 4.6: Microscopic images obtained under diffuse lighting of Apollo 16 sample 61141 in three stages of compaction. The scale of the images in the left column are 10 mm across the frame. The images in the right column are enlargements of the regions in the white boxes of the images in the left column and have a scale of 2.7mm across the image.

Table 4.1: Table of the calculated densities and filling factors of each compaction state for the albedo measurements made with OSEG.

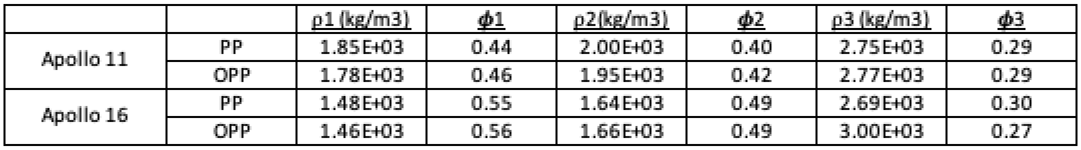

		ρ1 (kg/m3)	ϕ1	ρ2(kg/m3)	ϕ2	ρ3 (kg/m3)	ϕ3
Apollo 11	PP	1.85E+03	0.44	2.00E+03	0.40	2.75E+03	0.29
	OPP	1.78E+03	0.46	1.95E+03	0.42	2.77E+03	0.29
Apollo 16	PP	1.48E+03	0.55	1.64E+03	0.49	2.69E+03	0.30
	OPP	1.46E+03	0.56	1.66E+03	0.49	3.00E+03	0.27

4.3 OSEG Results

The OSEG data for a wavelength of 500nm are presented in terms of Lambert albedo. Two types of reflectance datasets for each sample; 1) along the principal plane and 2) perpendicular to the principal plane. For each dataset, the density was varied as mentioned in the previous section and then reflectance measurements were made at fixed incidence angles of i=0, 15, 30 and 45 degrees. The results for fixed incidence angle of zero are shown in Figures 4.6 - 4.9 Both the Apollo 11 and 16 soil samples show an increase in albedo for each state of compaction/decreased state of porosity. The Apollo 11 albedo along the principal plane for *e* =20 degrees increases from 0.055 to 0.07 and for *e* =60 degrees increases from 0.092 to 0.125. The Apollo 16 albedo for *e* =20 degrees increases 0.125 to 0.145 and for *e* =60 degrees increases from 0.225 to 0.255.

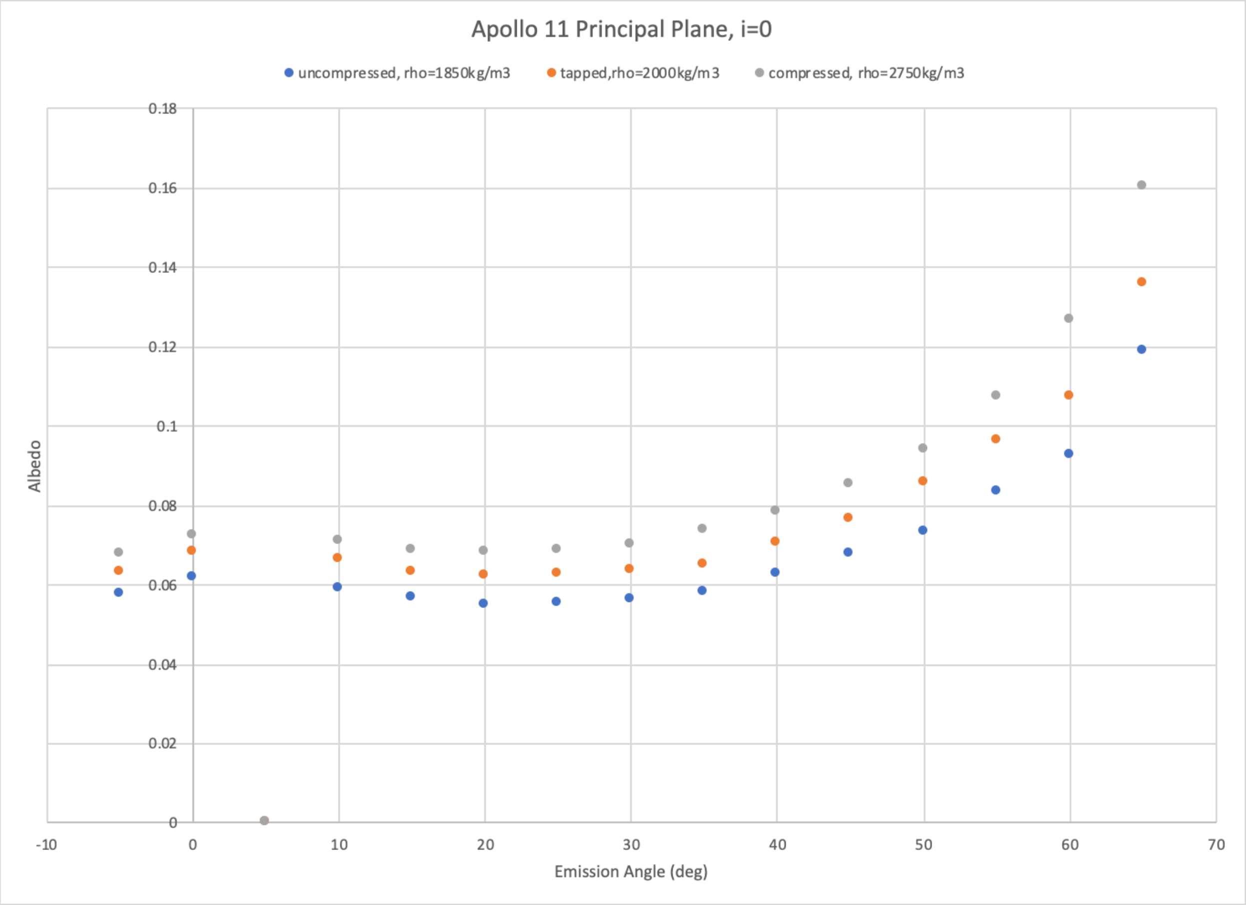

Figure 4.7: Principal plane plot of the reflectance versus emission angle for the three density states of Apollo 11. The incidence angle is fixed at zero.

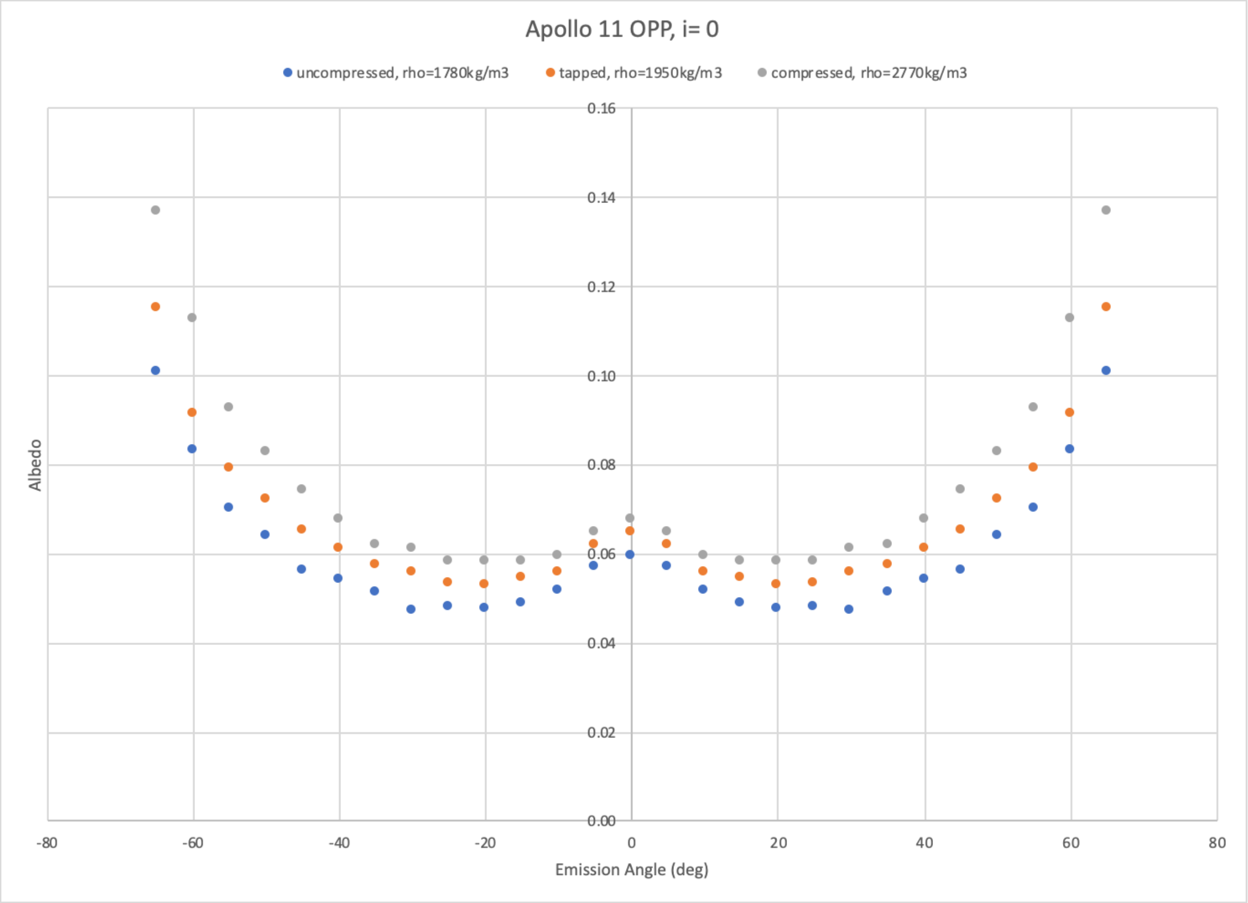

Figure 4.8: Perpendicular to the principal plane plot of the reflectance versus emission angle for the three density states of Apollo 11. The incidence is fixed at i=0 for each data point in this plot. You can clearly see the effect of compaction on the albedo.

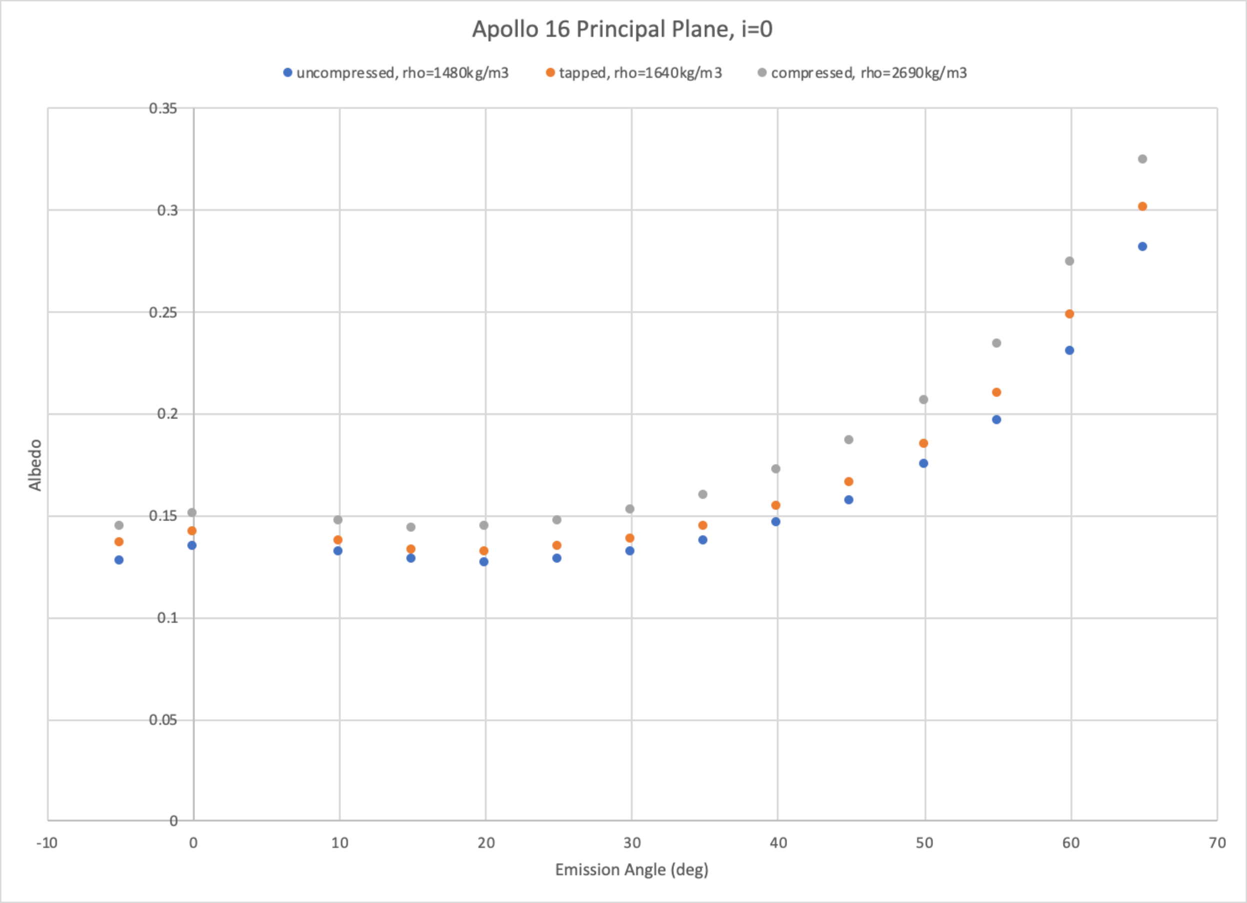

Figure 4.9: Principal plane plot of the reflectance versus emission angle for the three density states of Apollo 16. The incidence angle is fixed at i=0.

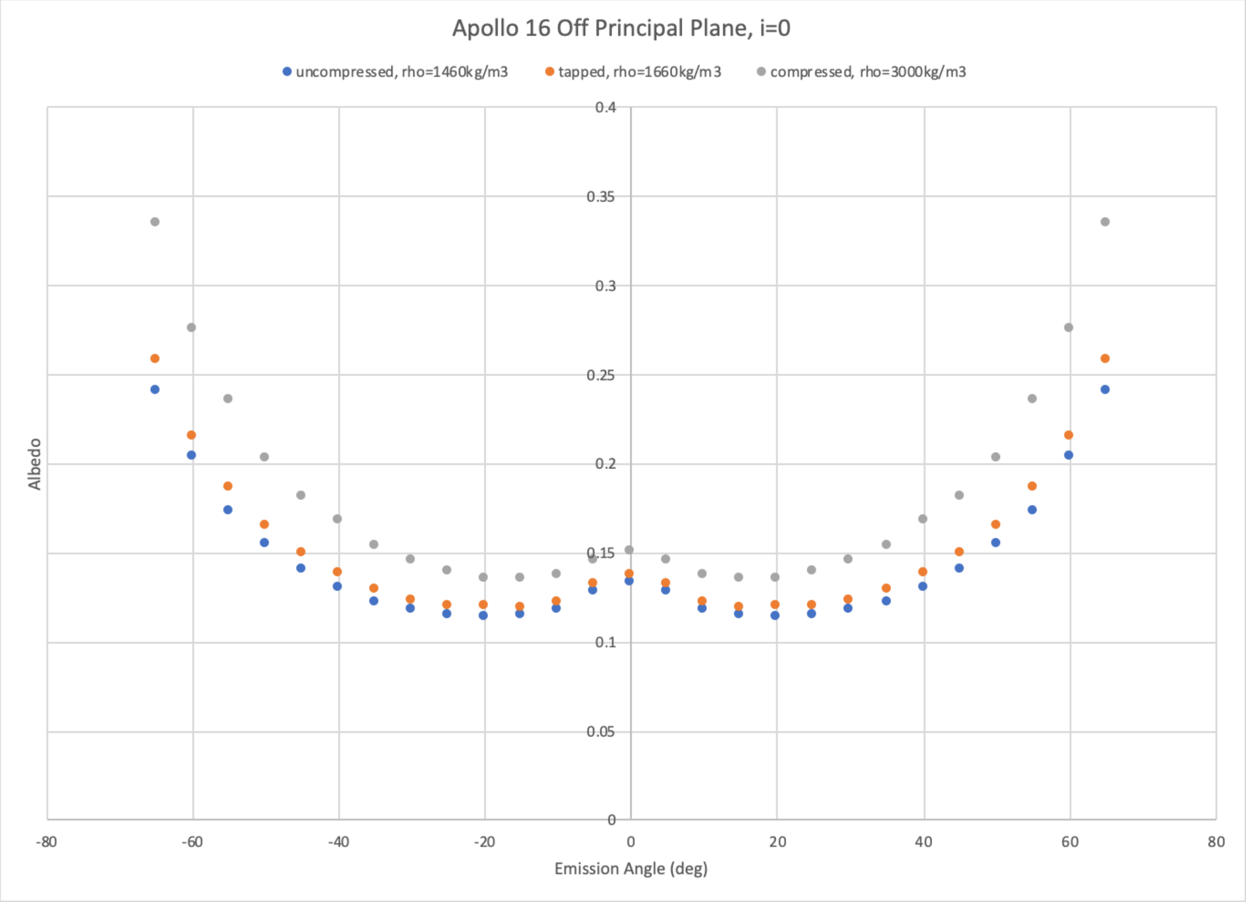

Figure 4.10: Perpendicular to the principal plane plot of the reflectance versus emission angle for the three density states of Apollo 16.

In order to quantify the sensitivity of albedo to the compaction of the lunar soil, we plot the BRDF of both Apollo datasets as a function of density for three different photometric combinations, i=15, 30 and 45 degrees. (See Figs. 4.11-4.13) We fit the data points to a line to determine the albedo/density slopes (See Table 4.2). The albedo/density slopes for Apollo 16 are almost twice as high as the slopes for the Apollo 11 data. This implies that the albedo of the Apollo 16 highlands soil sample is somewhat more easily compacted than the Apollo 11 Mare soil sample.

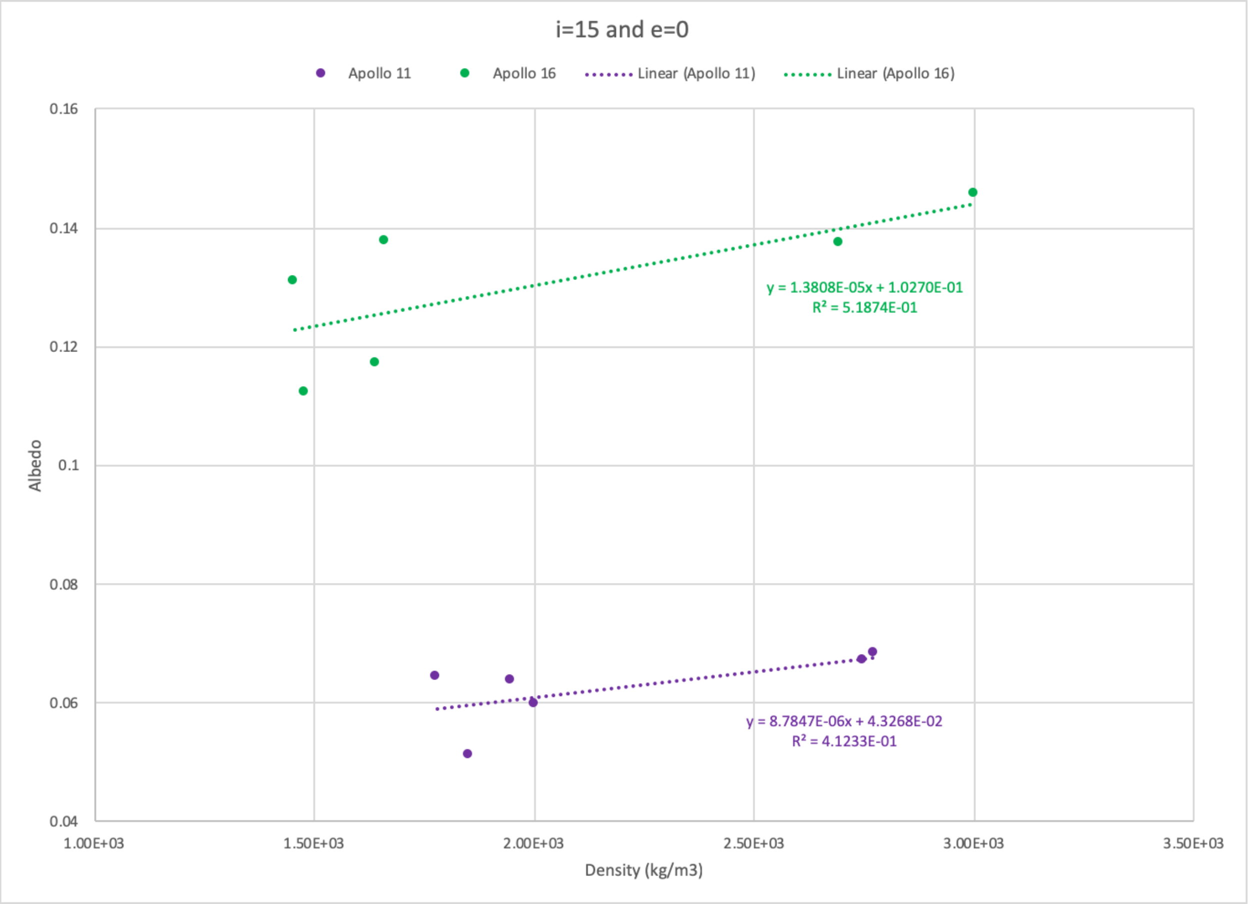

Figure 4.11: Albedo versus density for incidence angle of 15 degrees and emission angle of zero.

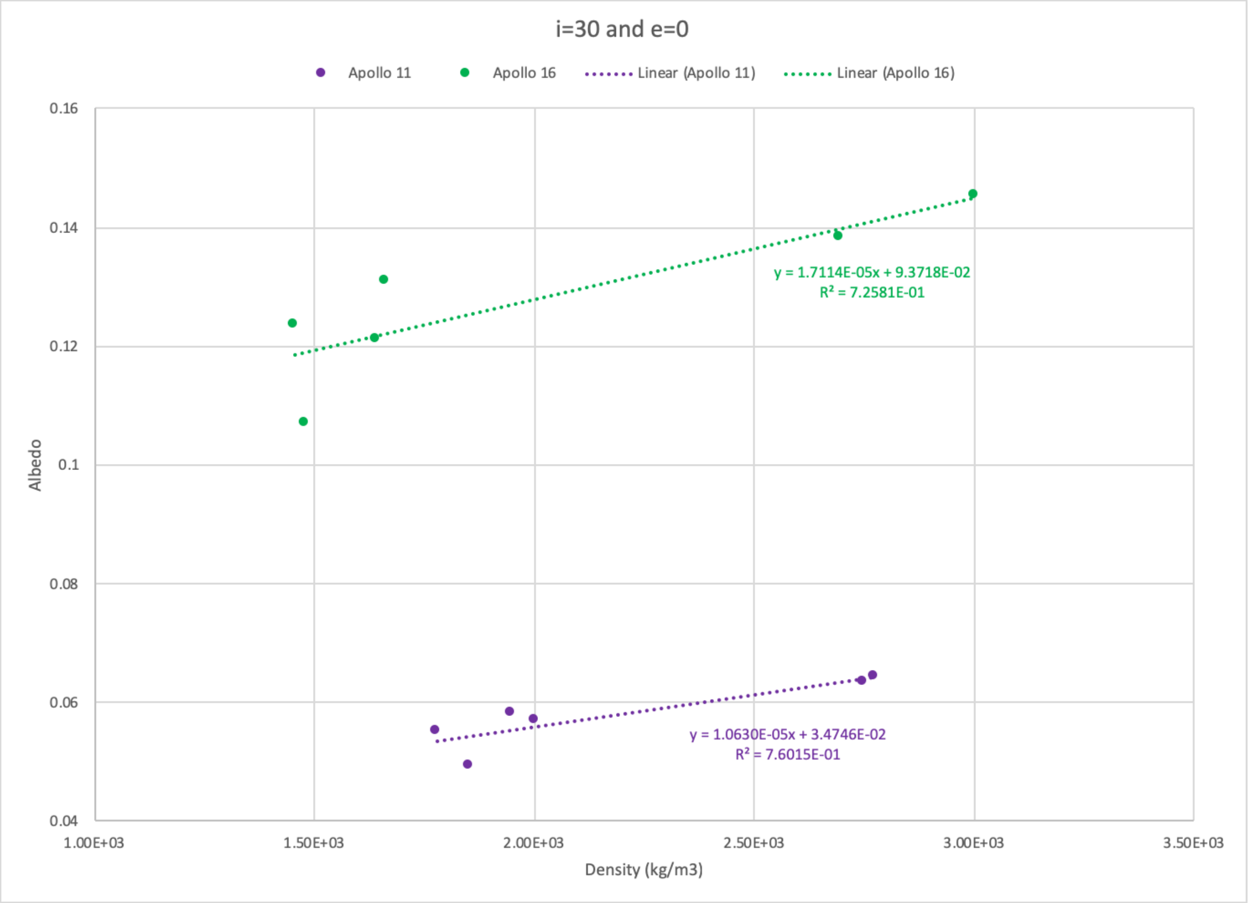

Figure 4.12: Albedo versus density for incidence angle of 30 degrees and emission angle of zero.

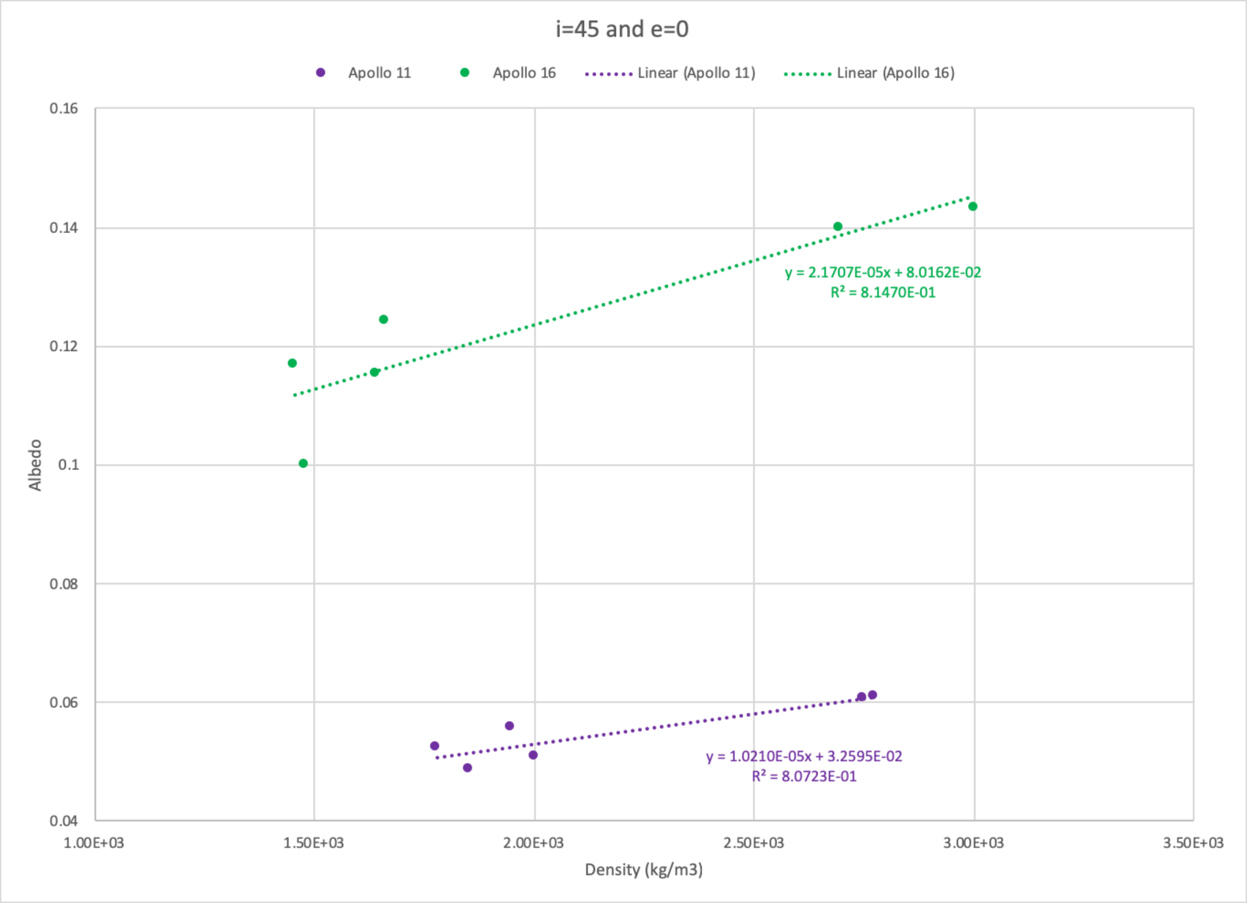

Figure 4.13: Albedo versus density for incidence angle of 45 degrees and emissison angle of zero.

Table 4.2 Table of best fit albedo/density slopes for the OSEG data in Figures 4.11-4.13. The albedo/density slopes for Apollo 16 are almost twice as high as the slopes for the Apollo 11 data. This implies that the albedo of the Apollo 16 highlands soil sample is more sensitive to compaction that the Apollo 11 Mare soil sample.

	Apollo 11	**Apollo 16**
***i*=15**	0.0000087847	0.000013808
***i*=30**	0.00001063	0.000017114
***i*=45**	0.00001021	0.000021707

4.3 Discussion

As of now, we understand that the albedos of all the Apollo samples are sensitive to compaction. This is not surprising, as our results are consistent with previous studies that model the reflectance behavior due to changes in porosity of lunar soils (Hapke and Sato, 2016 and Ohtake et al., 2010). From Chapter Two, our derived single scattering albedos, *w*, at 550nm are 0.288 and 0.488 for our Apollo 11 and Apollo 16 samples respectively. Our values for filling factor, $\boldsymbol{\phi}$, range between 0.27 and 0.56. These are within the range that Hapke (2008) theory would predict reflectance significant sensitivity porosity (See Fig. 4.1). Our results also show that the reflectance of Apollo 16 is more sensitive to compaction than Apollo 11. This is consistent with the results of previous observations and models which show that soils with intermediate reflectances are the most sensitive to variable compaction (Hapke, 2008, Hapke and Sato, 2016). However, the porosity value that Hapke and Sato calculated does not appear to be consistent with previous estimates. Their porosity value of $\boldsymbol{\phi}$=0.14 (P=0.84) was quoted as a lower limit for the porosity of the lunar soil, which would imply a bulk density of only 434 kg m^{-3}. This is not consistent with current lunar thermal models, which use a minimum bulk density at the lunar of 1100 kg m^{-3} (Hayne et al., 2017). The lunar sourcebook lists a range of bulk densities that are based on early remote sensing and *in-situ* measurements of the upper few centimeters of the lunar regolith. The inferred bulk density of the lunar surface before the Apollo landing was 1100kg m^{-3} at the surface and increased linearly to 1600 kg m^{-3} at 5cm below the surface. (Lunar Sourcebook, 1992) Our OSEG lab results for bulk density and calculated filling factors are consistent with these previous bulk density estimates. Based on in-situ and remote sensing measurements, the surface of the actual lunar regolith appears to be in a partially compacted state. This is not seemingly apparent in the photo in Figure 1.1, which shows that the bootprint of the Apollo astronaut is clearly compacted whereas the surrounding soil appears to be distinctly less densified. Whether or not differences in compaction is the sole explanation for the discrepancies in the reflectances of our Apollo 16 lab samples relative to those on the Moon, or whether other factors such as maturity or spatial variability also play a role can't be determined conclusively at this time.

REFERENCES

Allen, C. C., Greenhagen, B. T., Hanna, K. D., and Paige, D. A. (2011) "Remote analysis of Lunar pyroclastic glass deposits by LRO Diviner", LPSC XLII, Abstract 1512.

ASTM Solar Constant and Zero Air Mass Solar Spectral Irradiance Tables 1 (2014) Designation: E490 − 00a

Bandfield, J. L, Song, E., Hayne, P. O, Brand, B. D., Ghent, R. R., Vasavada, A. R. and Paige, D. A., "Lunar cold spots: Granular flow features and extensive insulating materials surrounding young craters", Icarus 231, 221-231 (2014)

Bandfield, J. L., Hayne, P. O., Williams, J. P., Greenhagen, B. T., & Paige, D. A. (2015), Lunar surface roughness derived from LRO Diviner Radiometer observations, Icarus, 248, 357-372.

Bandfield, J. L.; Cahill, J. T. S.; Carter, L. M.; Neish, C. D.; Patterson, G. W.; Williams, J.-P. and Paige, D. A. (2017) "Distal ejecta from lunar impacts: Extensive regions of rocky deposits", Icaurs 283, 282-299.

Biggar, S. F., Labed, J. , Santer, R.P., Slater, P.N.,.Jackson, R.D and Moran, M.S., (1988). Laboratory calibration of field reflectance panels, Proc. Soc. Photo-Opt. Instrum. Eng. 924:232-240.

Biggar, S. F., K. Thome and W. Wisniewski (2003), "Vicarious Radiometric calibration of EO-1 sensors by reference to high reflectance ground targets," IEEE TGRS 41:1174-1179.

Birkebak, R.C., Cremers, C. J. and Dawson, J. P. (1970). Directional spectral and total reflectance of lunar material, Proceedings of the Apollo 11 Lunar Science Conference, Vol. 3, pp. 1993 to 2000

Blewett, D. T., Lucey, P. G., Hawke, B. R., Ling, G. G. and Robinson, M. S. (1997), "A Comparison of Mercurian Reflectance and Spectral Quantities with Those of the Moon", ICARUS 129, 217–231.

Buratti, B. J., Hillier, J. K. and Wang, M. (1996), "The Lunar Opposition Surge: Observations by Clementine", ICARUS, 124, 490-499.

Chandrasekhar, S.. Radiative Transfer, Dover Publications, 1960

Cisneros, E., Awumah, A. Brown, H.M., Martin, A.C., Paris, K.N., Povilaitis, R.Z., Boyd, A.K., Robinson, M.S. and the LROC Team. (2017) "Lunar Reconnaissance Orbiter Camera

Permanently Shadowed Region Imaging – Atlas and Controlled Mosaics" Lunar and Planetary Science XLVIII.

Duke, M. et al., (1970) "Genesis of the soil and Tranquility Base. In: Proc. Apollo 11 Lunar Science Conference Geochem. Cosmochem. Acta, Cambridge, MA, pp.347-361.

Foote E. J., Paige D. A. Johnson J. R. Grundy W. M. Shepard M. K. (2009) "The Bidirectional Reflectance of Apollo 11 Soil Sample 10084", 40th LPSC Abstract #2500.

Foote, E. J., Paige, D. A., Shepard, M. K, Johnson, J. R., Biggar, S. F., Greenhangen, B. T. and Allen, C. C. (2010), "Apollo 11 and 16 Soil Bi-Directional Solar Reflectance Measurements: Models and LRO Diviner Observations", American Geophysical Union Fall Meeting, 2010.

Glotch, T. D., Lucey, P. G., Bandfield, J. L., Greenhagen, B. T., Thomas, I. R., Elphic, R. C., Bowles, N., Wyatt, M. B., Allen, C. C., Hanna, K. D. and Paige, D. A., (2010) "Highly Silicic Compositions on the Moon", SCIENCE, 329, 1510-1513.

Goguen, J. D., Stone, T. C., Kieffer, H. H., Buratti, B. J. (2010) "A new look at photometry of the Moon", ICARUS, 208, 548-557.

Gold, T., (1955) "The Lunar Surface"Royal Astronomical Society, Vol. 115, pages 585-684.

Morris, R., Score R., Dardano, C. and Heiken , G. (1983) Handbook of Lunar Soils. NASA Planetary Materials Branch. Publication 67, JSC 19069.

Hapke, B. and Von Horn, H. (1963), "Photometric Studies of Complex Surfaces with. Applications to the Moon", JGR, Volume 68, Number 15.

Hapke, B. (1981), "Bidirectional reflectance spectroscopy: 1" Theory, J. Geophys. Res., 86, 3039–3054.

Hapke, B. Theory of Reflectance and Emittance Spectroscopy, Cambridge University Press, 1993;

Hapke, B., Nelson, R. and Smythe, W. (1998) "The Opposition Effect of the Moon: Coherent Backscatter and Shadow Hiding", ICARUS, 133, 89-97.

Hapke, B., (2008) "Bidirectional reflectance spectroscopy 6. Effects of porosity" Icarus 195, 918–926

Hapke, B. Theory of Reflectance and Emittance Spectroscopy, Cambridge University Press, 2012;

Hapke, B. and Sato, H. (2016) “The porosity of the upper lunar regolith” ICARUS vol. 273, 75-83.

Hayne, P. O., Bandfield, J. L., Siegler, M. A., Vasavada, A. R., Ghent, R. R., Williams, J.-P., … Paige, D. A. (2017). “Global regolith thermophysical properties of the Moon from the Diviner Lunar Radiometer Experiment” Journal of Geophysical Research: Planets, 122, 2371–2400.

Heffels, A., Knapmeyer, M., Obersta, J. and Haase, I. (2017) “Re-evaluation of Apollo 17 Lunar Seismic Profiling Experiment data” Planetary and Space Science. Volume 135, 43-54.

Helfenstein P. and Veverka, J., (1987) “Photometric properties of lunar terrains derived from Hapke’s equation. ICARUS, 72, 342-357.

Helfenstein P. and Shepard, M. K. (1999) “Submillimeter-Scale Topography of the Lunar Regolith”, ICARUS, 141, 107-131.

Hillier, J. K., Buratti, B. J. and Hill, K. (1999) “Multispectral Photometry of the Moon and Absolute Calibration of the Clementine UV/Vis Camera”, ICARUS, 141, 205-225.

Izawa, M. R. M., Applin, D. M., Cloutis, E. A., Cuddy, M. and Mann, P., (2014) “Spectroscopic studies of pristine lunar regolith under H2O, O2, and CO2 controlled conditions”, LPSC

Johnson, J.R., et al. JGR, 111, E02S14, 2005JE002494, 2006;

Johnson J. R. Shepard M. K. Paige D. A. Foote E. J. Grundy W. (2009) “Spectrogoniometric Measurements and Modeling of Apollo 11 Soil 10084”, 40th LPSC Abstract #1427.

Johnson, J. R, Shepard, M. K., Paige, D. A, Foote, E., Grundy, W. M. (2010), "Spectro-goniometric measurements and modeling of Apollo 16 soil 68810”, American Geophysical Union Fall Meeting, 2010

Johnson, J. R, Shepard, M. K., Grundy, W. M., Paige, D. A, Foote, E. (2013), "Spectrogoniometry and modeling of martian and lunar analog samples”, ICARUS, 223, 383-406.

Keihm, S. J. (1984), Interpretation of the lunar microwave brightness temperature spectrum: 634 Feasibility of orbital heat flow mapping, Icarus, 60(3), 568-589.

Korotev, R.L., and J.J. Gillis, JGR, 106, E6, 2001;

Lunar Sourcebook: A User’s Guide to the Moon, Cambridge University Press, LPI, 1992;

LROC Coordinates/quickmap for Apollo landing sites; http://www.lroc.asu.edu/

LROC images (https://www.lroc.asu.edu/images)

Mazarico, E., Neumann, G.A., Smith, D. E., Zuber, M. T., Torrence, M.H. (2011) Illumination conditions of the lunar polar regions using LOLA topography

McCord,T. B., Clark, R. N., Hawke, B. R., McFadden, L. A., Owensby, P. D., Pieters, C. M., Adams, J. B. (1981) "Moon' Near-Infrared Spectral Reflectance, A First Good Look", JGR, VOL. 86, NO. Bll, PAGES 10883-10892.

Milliken, R. E. and Mustard, J. F. "Quantifying absolute water content of minerals using near-infrared reflectance spectroscopy" (2005) Journal of Geophysical Research, Vol. 110, E12001

Minnaert, M. (1941) Photometry of the Moon. in Planets and Satellites, University of Chicago Press.

Näränen, J., Kaasalainen, S., Peltoniemi J., Heikkilä, S., Granvik, M., and Saarinen, V. (2004) "Laboratory photometry of planetary regolith analogs II. Surface roughness and extremes of packing density" Astronomy and Astrophysics 426, 1103–1109

NASA archive (https://images.nasa.gov/)

Ohtake, M., T. Matsunaga, Y. Yokota, S. Yamamoto, Y. Ogawa, T. Morota, C. Honda, J. Haruyama, K. Kitazato, H. Takeda, A. Iwasaki, R. Nakamura, T. Hiroi, S. Kodama, H. Otake (2010) "Deriving the Absolute Reflectance of Lunar Surface Using SELENE (Kaguya) Multiband Imager Data" Space Sci Rev 154: 57–77.

Ohtake, M., Pieters, C.M., Isaacson, P., Besse S., Yokota, Y., Matsunaga, T., J., Boardman S. Yamomoto, J. Haruyama, M. Staid, U. Mall , R.O. Green (2013) "One Moon, Many Measurements 3: Spectral reflectance" ICARUS Volume 226, 364-374.

Paige et al., DPS meeting #38, #49.01, 2006.

Paige, D. A., M. T. Foote, B. T. Greenhagen, J. T. Schofield, S. Calcutt, A. R. Vasavada, D. J. Preston, F. W. Taylor, C. C. Allen, K. J. Snook, B. M. Jakosky, B. C. Murray, L. T. Soderblom8, B. Jau, S. Loring, J. Bulharowski, N. Bowles, M. T. Sullivan, C. Avis, E. M. De Jong, W. Hartford and D. J. McCleese (2010a). "The Lunar Reconnaissance Orbiter Diviner Lunar Radiometer Experiment", Space Science Reviews . DOI: 10.1007/s11214-009-9529-2.

Paige, D.A., M. A. Siegler, J. A. Zhang, P. O. Hayne, E. J. Foote, K. A. Bennett, A. R. Vasavada, B. T. Greenhagen, Schofield, J. T., D. J. McCleese, M. C. Foote, E. M. De Jong, B. G. Bills, W. Hartford, B. C. Murray, C. C. Allen, K. J. Snook, L. A. Soderblom, S. Calcutt, F. W. Taylor, N. E. Bowles, J. L. Bandfield, R. C. Elphic, R. R. Ghent, T. D. Glotch, M. B. Wyatt, P. G. Lucey (2010b) "Diviner Lunar Radiometer Observations of Cold Traps in the Moon's South Polar Region", Science, 330, 479-482

Peltoniemi, J. I. and Lumme, K. (1992) “Light scattering by closely packed particulate media”, Journal of the Optical Society of America, Vol. 9, Issue 8, pp. 1320-1326

Plecia, J. B., Bussey, D. B. J., Robinson, M. S. and Paige, D. A. (2010) “King Crater – Surface properties derived from Diviner, Mini-RF, and LROC data”, LPSC XLI, Abstract 2160

Raut, U., Karnes, P. L., Retherford, K. D., Davis, M. W., Liu, Y., Gladstone, G. R., et al. (2018). Far-ultraviolet photometric response of Apollo soil 10084. Journal of Geophysical Research: Planets, 123, 1221–1229. https://doi.org/10.1029/ 2018JE005567

Rhodes, J. M., Blanchard, D. P., Dungan, M. A., Brannon, J. C., and Rogers, K. V. (1977) “Chemistry of Apollo 12 Mare Basalts: Magma types and fractionation processes” LPSC, p1305-1338.

Sato, H., M. S. Robinson, B. Hapke, B. W. Denevi, and A. K. Boyd (2014), Resolved Hapke parameter maps of the Moon, J. Geophys. Res. Planets, 119, 1775–1805, doi:10.1002/2013JE004580.

Shepard, M. K. (2001) “The Bloomsburg University Goniometer (BUG), An Integrated Laboratory for measuring Bidirectional Reflectance Functions”, LPSC XXXII, Abstract 1015.

Shepard, M. K. (2002) "Initial Results from the Bloomsburg University Goniometer Laboratory" Solar System Remote Sensing, p. 75

Shepard, M. K. and Helfenstein, P. (2007) "A test of the Hapke photometric model" Journal of Geophysical Research 112, E03001 doi:10.1029/2005JE002625

Shepard, M. K. and Helfenstein, P. (2011) "A laboratory study of the bidirectional reflectance from particulate samples”, ICARUS, 215, 526-533.

Shepard, M. K., Introduction to Planetary Photometry, Cambridge University Press, 2017.

Shkuratov, Y., Starukhina, L., Hoffmann, H. and Arnold, G. (1999) “A Model of Spectral Albedo of Particulate Surfaces: Implications for Optical Properties of the Moon” ICARUS. Vol. 137, Issue 2, pp 235-246

Vasavada, A. R., Paige, D. A., & Wood, S. E. (1999), Near-surface temperatures on Mercury and the Moon and the stability of polar ice deposits, Icarus, 141(2), 179-193.

Vasavada, A. R., Bandfield, J. L., Greenhagen, B. T., Hayne, P. O., Siegler, M. A., Williams, J.P., & Paige, D. A. (2012), Lunar equatorial surface temperatures and regolith properties from the Diviner Lunar Radiometer Experiment, J. Geophys. Res., 117(E12).

Warren, T. J., Bowles, N. E., Donaldson Hanna, K. and Thomas, I. R. (2017) "The Oxford space environment goniometer: A new experimental setup for making directional emissivity measurements under a simulated space environment" REVIEW OF SCIENTIFIC INSTRUMENTS 88, 124502

Warren, T. J., Bowles, N. E., Donaldson Hanna, K., & Bandfield, J. L. (2019). "Modeling the angular dependence of emissivity of randomly rough surfaces." Journal of Geophysical Research: Planets, 124, 585–601

Williams, J.-P., Paige, D. A., Greenhagen, B. T. and Sefton-Nash, E. (2017) "The global surface temperatures of the Moon as measured by the Diviner Lunar Radiometer Experiment", Icarus 283, 300-325.